DESIGN AND DEVELOPMENT OF IRON ALUMINIUM INTERMETALLIC COMPOUNDS FOR STRUCTURAL APPLICATIONS AT HIGH TEMPERATURES

A THESIS SUBMITTED TO
THE GRADUATE SCHOOL OF NATURAL AND APPLIED SCIENCES
OF
MIDDLE EAST TECHNICAL UNIVERSITY

BY

MEHMET YILDIRIM

IN PARTIAL FULFILLMENT OF THE REQUIREMENTS
FOR
THE DEGREE OF DOCTOR OF PHILOSOPHY
IN
METALLURGICAL AND MATERIALS ENGINEERING

DECEMBER 2014

Approval of the thesis:

DESIGN AND DEVELOPMENT OF IRON ALUMINIUM INTERMETALLIC COMPOUNDS FOR STRUCTURAL APPLICATIONS AT HIGH TEMPERATURES

submitted by **MEHMET YILDIRIM** in partial fulfillment of the requirements for the degree of **Doctor of Philosophy in Metallurgical and Materials Engineering Department, Middle East Technical University** by,

Prof. Dr. Gülbin Dural Ünver _____
Dean, Graduate School of **Natural and Applied Sciences**

Prof. Dr. Cemil Hakan Gür _____
Head of Department, **Metallurgical and Materials Eng.**

Prof. Dr. M.Vedat Akdeniz _____
Supervisor, **Metallurgical and Materials Eng. Dept**., **METU**

Prof. Dr. Amdulla O. Mekhrabov _____
Co-Supervisor, **Metallurgical and Materials Eng. Dept**., **METU**

Examining Committee Members:

Prof. Dr. Tayfur Öztürk _____
Metallurgical and Materials Eng. Dept., METU

Prof. Dr. M. Vedat Akdeniz _____
Metallurgical and Materials Eng. Dept., METU

Prof. Dr. Caner Durucan _____
Metallurgical and Materials Eng. Dept., METU

Prof. Dr. Şükrü Talaş _____
Metallurgical and Materials Eng. Dept., AKU

Assoc. Dr. Y. Eren Kalay _____
Metallurgical and Materials Eng. Dept., METU

Date: 18.12.2014

I hereby declare that all information in this document has been obtained and presented in accordance with academic rules and ethical conduct. I also declare that, as required by these rules and conduct, I have fully cited and referenced all material and results that are not original to this work.

Name, Last name : Mehmet Yıldırım

Signature :

ABSTRACT

DESIGN AND DEVELOPMENT OF IRON ALUMINIUM INTERMETALLIC COMPOUNDS FOR STRUCTURAL APPLICATIONS AT HIGH TEMPERATURES

Yıldırım, Mehmet
PhD, Department of Metallurgical and Materials Engineering
Supervisor: Prof. Dr. M.Vedat Akdeniz
Co-Supervisor: Prof. Dr. Amdulla O. Mekhrabov

December 2014, 175 pages

Fe-Al based intermetallic compounds are considered as suitable candidates for structural applications at high temperatures due to their outstanding oxidation and corrosion resistance, good intermediate temperature strength, low density, low cost and relatively high melting point. These outstanding physical and mechanical properties are mainly attributed to their long-range ordered superlattices, deviation from stochiometry and ternary alloying additions. However, poor ductility at ambient temperatures significantly restricts the fabricability and potential applications. Thus, further alloy design and development is needed in order to improve insufficient properties.

This study focuses on two main topics: (i) investigation of the effect of ternary alloying additions on ordering characteristics especially B2↔A2 order-disorder transformation temperature and site occupancy characteristics of $Fe_{50}Al_{50-n}X_n$ intermetallics and confirmation of the validity of theoretical predictions proposed for single phase $Fe_{50}Al_{50-n}X_n$ intermetallics, (ii) improvement of room temperature

mechanical properties and high temperature oxidation behavior of $Fe_{50}Al_{50-n}X_n$ intermetallics via alloying additions and/or proper heat-treatment.

The effect of ternary alloying element additions on the ordering characteristics, room temperature mechanical properties and oxidation behavior of B2-type ordered FeAl intermetallic compounds were studied for as-cast and heat-treated states. It is shown that type and content of ternary alloying element together with heat-treatment have strong influences on these properties. It is also shown that type of ternary alloying element has also important effect on ordering characteristics such as order-disorder transition temperature and site occupancy behavior.

In order to have better analyzing of order-disorder transition, experimentally measured transition temperatures were compared with theoretical predictions where excellent agreement was obtained. In this manner, the relative partial ordering energy parameter (RPOE), β, has been defined for the first time. The RPOE parameter takes into account both site occupancy behavior of alloying elements and variation of order-disorder transition temperature. The sign of this parameter implies the distribution of alloying elements over Fe or Al sublattices, while its magnitude provides useful information about order-disorder transition temperatures featuring the bond strengths of Al-X or Fe-X pairs relative to Fe-Al pair. Current predictions based on the RPOE parameter are consistent with the theoretical predictions.

Mechanical characterization of the alloys reveals that room temperature mechanical properties strongly depend on ordering and microstructural features such as volume fraction, size, morphology and distribution of existent phases and solidification route, i.e, eutectic or liquidus + solidus. These microstructural parameters can be controlled by controlling the Al content and content of ternary alloying element. Al content dominates the order, whereas content of ternary alloying element dominates the volume fraction of present phases with regard to solid solubility of alloying element in FeAl intermetallic.

The cyclic oxidation tests and structural characterization of oxide scale after oxidation demonstrated that protective, continuous and stable α-Al_2O_3 scale can

easily be formed by proper selection of the type and content of alloying elements. Analyzing the results, formation of α-Al_2O_3 scale takes place in the first few cycles of oxidation indicating the fast growing of even, continuous and uniform scale without formation of any voids or cracks.

Keywords: Iron Aluminides, Microstructure, Order-Disorder Phase Transition, Room Temperature Mechanical Properties, Oxidation Behavior

ÖZ

YÜKSEK SICAKLIK YAPISAL UYGULAMALARI İÇİN DEMİR-ALÜMİNYUM METALLERARASI BİLEŞİKLERİNİN TASARIMI VE GELİŞTİRİLMESİ

Yıldırım, Mehmet
Doktora, Metalurji ve Malzeme Mühendisliği Bölümü
Tez Yöneticisi: Prof. Dr. M.Vedat Akdeniz
Ortak Tez Yöneticisi: Prof. Dr. Amdulla O. Mekhrabov

Aralık 2014, 175 sayfa

Fe-Al esaslı metallerarası bileşikler sahip oldukları mükemmel oksitlenme ve korozyon dirençleri, orta sıcaklık mukavemetleri, düşük yoğunlukları, düşük maliyetleri ve nispeten yüksek erime noktalarından dolayı yüksek sıcaklıktaki yapısal uygulamalar için aday malzemeler olarak düşünülmektedir. Bu tip malzemelerin üstün fiziksel ve mekanik özellikleri çoğunlukla sahip oldukları uzun mesafe düzenine sahip süper-kafeslerine, stokiyometriden sapmalarına ve üçüncül alaşım elementi ilavesine bağlıdır. Ancak oda sıcaklığında sahip oldukları düşük süneklik üretilebilirliklerini ve olası uygulama alanlarını önemli ölçüde kısıtlamaktadır. Bu sebeple ileri alaşışm tasarımına ve geliştirilmesine ihtiyaç duyulmaktadır.

Bu çalışmada iki temel amaç hedeflenmiştir: (i) üçüncül alaşım elementi ilavesinin $Fe_{50}Al_{50-n}X_n$ metallerarası bileşiklerinin B2↔A2 düzen-düzensizlik faz dönüşüm sıcaklığı ve birim kafes pozisyonları gibi düzenlenme karakteristiklerine etkisinin incelenmesi ve tek fazlı yapıya sahip $Fe_{50}Al_{50-n}X_n$ metallerarası bileşikleri için önerilen teorik tahminlerin doğruluğunun ispatlanması, (ii) $Fe_{50}Al_{50-n}X_n$ metallerarası

bileşiklerinin oda sıcaklığındaki mekanik özellikleri ve yüksek sıcaklık oksitlenme davranışlarının alaşım elementi ilavesi ve/veya uygun ısıl işlem yöntemleri ile geliştirilmesi.

Üçüncül alaşım elementi ilavesinin B2 tip düzenli yapıya sahip FeAl metallerarası bileşiklerinin yapısal özelliklerine, mikroyapısına, oda sıcaklığındaki mekanik özelliklerine ve oksitlenme davranışına etkisi hem dökülmüş haldeki hem de ısıl işlem görmüş numunelerde incelenmiş, üçüncül alaşım elementinin cinsi ve mikatrının uygun tavlama koşulları ile birlikte incelenen özelliklere önemli etkisinin olduğu saptanmıştır. Ayrıca üçüncül alaşım elementinin cinsinin düzen-düzensizlik faz dönüşüm sıcaklığı ve birim kafes pozisyonları gibi düzenlenme karakteristiklerine önemli etkisinin olduğu gözlenmiş, elde edilen sonucların var olan teorik verilerle mükemmel uymluluk gösterdiği saptanmıştır.

Düzen-düzensizlik faz dönüşümlerini daha iyi analiz etmek için deneysel olarak ölçülen dönüşüm sıcaklıkları teorik tahminler ile kıyaslanmış ve mükemmel uyumluluk gösterdiği saptanmıştır. Bu bağlamda, relatif kısmi düzenlenme enerjisi parametresi, β, literatürde ilk defa tanımlanmıştır. Bu parametre hem alaşım elementlerinin birim kafeste hangi pozisyona yerleşeceklerini hem de düzen-düzensizlik faz dönüşüm sıcaklığındaki değişiklikleri hesaba katmaktadır. Bu parametrenin işareti alaşım elemetinin Fe ya da Al alt-kafeslerinden hangisine yerleşeceğini, büyüklüğü ise Al-X ve Fe-X çiftlerinin relatif bağ kuvvetlerini Fe-Al çiftinin bağ kuvvetti ile kıyaslayarak düzen-düzensizlik faz dönüşüm sıcaklığı hakkında önemli bilgi vermektedir. Bu parametre temelinde yapılan hesaplamalar teorik tahminler ile iyi bir uyum göstermektedir.

Alaşımların mekenik karakterizasyonu oda sıcaklığındaki mekanik özelliklerin düzenlenme ve yapı içerisinde bulunan fazların sayısı, miktarı, büyüklüğü, morfolojisi ve dağılımı gibi mikroyapısal parametreler ve alaşımların katılaşma davranışına çok fazla bağlı olduğunu göstermiştir. Bu mikroyapısal parametreler üçüncül alaşım elementi ve yapıdaki Al miktarı ile kontrol edilmektedir. Yapıdaki Al miktarı düzenlenmeyi kontrol ederken, üçüncül alaşım elementinin çeşidi ve miktarı

ise var olan fazların miktarlarını alaşım elementinin FeAl metallerarası bileşiğindeki çözünürlüğüne bağlı olarak kontrol etmektedir.

Çevrimsel oksitlenme testleri ve test sonrası oluşan oksit tabakasının yapısal karakterizasyonu koruyucu, sürekli ve kararlı α-Al_2O_3 tabakasının uygun türde ve miktarda üçüncül alaşım elementi seçilerek kolaylıkla oluşabileceğini göstermiştir. α-Al_2O_3 oksit tabakasının ilk birkaç çevrimde oluşması düzenli, kararlı ve sürekli tabakanın herhangi bir boşluk ya da çatlak oluşmadan hızlıca büyüdüğünü göstermektedir.

Anahtar Sözcükler: Demir Alümintler, Mikroyapı, Düzen-Düzensizlik Faz Dönüşümleri, Oda Sıcaklığı Mekanik Özellikler, Oksitlenme Davranışı.

To Özlem and my lovely son Demir.

ACKNOWLEDGMENTS

I would like to express my gratitude to my supervisors Prof. Dr. M. Vedat Akdeniz and Prof. Dr. Amdulla O. Mekhrabov for their supervision, support, guidance and encouragement during this study. They trusted in me, gave the chance of doing independent research and helped me get over every obstacle on the way.

I sincerely acknowledge the former and present members of NOVALAB group; Sıla Süer, Cem Topbaşı, Nagehan Duman, Sultan Aybar, Mine Kalkancı, Erdem Mermer, Mahsuni Yalçın, Amir Fadaie, Bengi Yağmurlu, Merve Karataş and Tufan Güngören for making this long journey fun. I would also like to thank Nusret Serhat Ün, Nihat Ali Işıtman and Halil İbrahim Yavuz for their endless friendship.

I would like to express my special thanks to Muratahan Aykol, for his encouraging discussions, endless motivation, clever hints and his deep and never ending knowledge. I am grateful to Cengiz Tan, Necmi Avcı, Yusuf Yıldırım, Serkan Yılmaz, Önder Şahin, Hülya Kılıç Yalçın, İsa Hasar, Arif Atalay Özdemir and Cemal Yanardağ for their significant technical support. I am thankful to METU Metallurgical and Materials Engineering Department for providing facilities for my research.

I am also thankful to my parents for their endless support throughout my lengthy education. Especially, I would also like to thank my love Özlem Altıntaş Yıldırım for her understanding and support, and my lovely son, Demir,

This work was financially supported by DPT-ÖYP research funds and TUBİTAK, National Scholarship Programme for Ph.D. Students (2211). This work was also supported through TUBITAK, Project No MAG-COST-535 (104M323), which I also gratefully acknowledge.

TABLE OF CONTENTS

LIST OF TABLES

TABLES

LIST OF FIGURES

FIGURES

CHAPTER 1

INTRODUCTION

Intermetallic compounds are considered as metallic materials formed by two or more metallic elements. These compounds have long-range ordered crystal structures, different from those of their metallic components, below a crucial temperature called as order-disorder phase transition temperature (T_c).

Aluminides of iron, nickel and titanium have attracted considerable research interest among the big family of intermetallic compounds during the past 20 years due to their outstanding structural and mechanical properties especially at elevated temperatures [1-4]. In this particular aspect, iron aluminides are suitable candidates for structural applications at high temperature due to their excellent oxidation and corrosion resistance, low density, relatively high melting point, good intermediate temperature strength compared to many other commercial Fe based materials such as stainless steels and cast irons [5-15]. These excellent physical and mechanical properties are mainly attributed to their long-range ordered superlattices, deviation from stochiometry and type and content of ternary alloying additions. However, poor ductility and brittleness at ambient temperatures greatly restrain the fabricability and potential applications of iron aluminides like other intermetallic compounds. Therefore, much attempt is still being performed to improve the insufficient mechanical properties at room temperature via macroalloying, microalloying and appropriate thermal treatments [8, 13, 14].

This study have two main aims: (i) to investigate the effect of ternary alloying additions on ordering characteristics especially B2↔A2 order-disorder transformation temperature and site occupancy characteristics of $Fe_{50}Al_{50-n}X_n$ intermetallics and to confirm the validity of theoretical predictions proposed for

single phase $Fe_{50}Al_{50-n}X_n$ intermetallics, (ii) to improve room temperature mechanical properties and high temperature oxidation behavior of $Fe_{50}Al_{50-n}X_n$ intermetallics via alloying additions and/or proper heat-treatment.

Variation of B2↔A2 order-disorder phase transition temperature in FeAl intermetallic compound was studied theoretically by Akdeniz and Mekhrabov [16] by tuning systematically the type and content of ternary alloying elements. However, best to our knowledge, there is very little experimental information based on order-disorder transition temperatures of B2-type ordered FeAl intermetallic compounds. Therefore, this study aims investigation of order-disorder transition temperatures experimentally by means of thermal analysis measurements and confirmation of theoretical predictions proposed for single phase $Fe_{50}Al_{50-n}X_n$ intermetallics,. In this manner, relative partial ordering parameter (RPOE), β, has been defined for the first time. RPOE parameter gives useful information about site occupancy behaviour of ternary alloying element atoms over Fe or Al sublattices and variation of critical order-disorder transition temperature relative bond strengths of Al-X or Fe-X pairs relative to Fe-Al pair.

In addition, it was attempted to provide a direct correlation between microstructures and room temperature mechanical properties in order to hinder room temperature brittleness. In this particular aspect, main emphasis was directed toward which alloying possibility, i.e., single phase FeAl solid solution, FeAl solid solution with binary intermetallic precipitates or ultrafine eutectic phase mixtures whose components are Fe-Al based phase and a ternary intermetallic phase, provides best combination of room temperature mechanical property, high strength with enhanced plasticity.

This thesis begins with providing some basic metallurgical concepts related to intermetallic compounds and a review of previous studies in Chapter 2. In Chapter 3, the experimental methods used for production and characterization of investigated materials are given. In Chapter 4, effect of ternary alloying additions on ordering characteristics, especially order-disorder phase transition temperatures of $Fe_{50}Al_{50-}$

$_nX_n$ (n=1 at.%), X= Cr, Mn, Ni, Ti, Ta, Mo and W, alloys are investigated. This thesis continues with investigation of the structural properties and room temperature mechanical properties of $Fe_{50}Al_{50-n}X_n$, X= Cr, Mn, Mo, Nb, Hf and Zr, alloys in Chapter 5 followed by discussing oxidation behavior of $Fe_{50}Al_{50-n}X_n$, X= Ti and B alloys, by studying the cyclic oxidation kinetics in Chapter 6. Finally, this thesis is concluded in Chapter 7 by highlighting the major contributions to the research field of iron aluminides.

CHAPTER 2

THEORETICAL BACKGROUND

2.1 Solid Solutions and Ordered Intermetallic Compounds

A *solid solution* is formed whenever atoms of different elements occupy a common crystal lattice without formation of new structures. There are two types of solid solutions: interstitial and substitutional. For interstitial solid solutions, the solute or impurity atoms are placed in the holes (interstices) between the host atoms due to the large size difference between the solute and host atoms.

For substitutional solid solutions, the host atoms are replaced by the solute or impurity atoms in the crystal lattice. Crystal structure, atomic size mismatch, electronegativity and valences are the governing factors of solid solubility.

- **Crystal Structure:** For extended solid solubility, crystal structures of both elements should be same.
- **Atomic Size Mismatch:** If the atomic size (atomic radii) difference between the two elements is less than 15 %, solid solution is formed. Otherwise, new phase will form.
- **Electronegativity:** For complete solid solubility, atoms of different elements should have similar electronegativity.
- **Valence:** For complete solid solubility, atoms of different elements should have same valence. A metal will dissolve a metal of higher valence to a greater extent than one of lower valence.

Substitutional solid solutions can be either disordered or ordered. Disordered solid solutions are obtained when the solute atoms randomly replace the host atoms; whereas ordered solid solutions are formed when unlike atoms occupy the adjacent sites in crystal lattice. A fully ordered solid solution is generally called as *superlattice*. A schematic presentation of types of solid solutions is given in Figure 2.1.

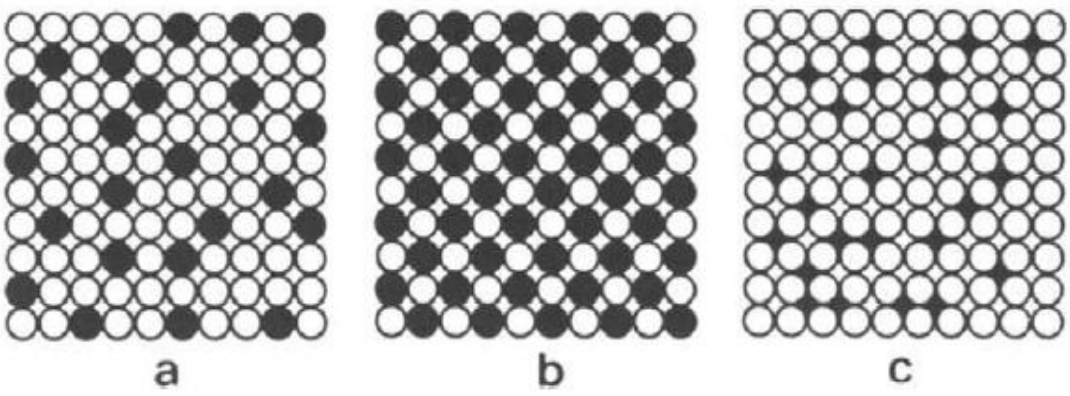

Figure 2.1 Schematic models of solid solutions. (a) disordered (random) substitutional; (b) ordered substitutional; (c) interstitial Adapted from Ref. [17].

A *continuous series of solid solution* is formed if the two different elements are replaced at all compositions, whereas a *terminal (primary) solid solution* is formed when the solid solubility is only present at the pure element portions of the binary phase diagrams. However, as the solid solubility of one element in the other is limited around a stoichiometric composition, the arising phase is called as *intermetallic compound*. Restriction of the solid solubility is illustrated in Figure 2.2. The solid solubility of B atoms in A decreases with increasing the stability of intermediate phase.

Intermetallic compounds have ordered crystal structures completely different from those of their metallic constituent and these compounds have simple stoichiometric ratios (AB, AB_3, A_3B, etc.) and narrow compositional ranges [1].

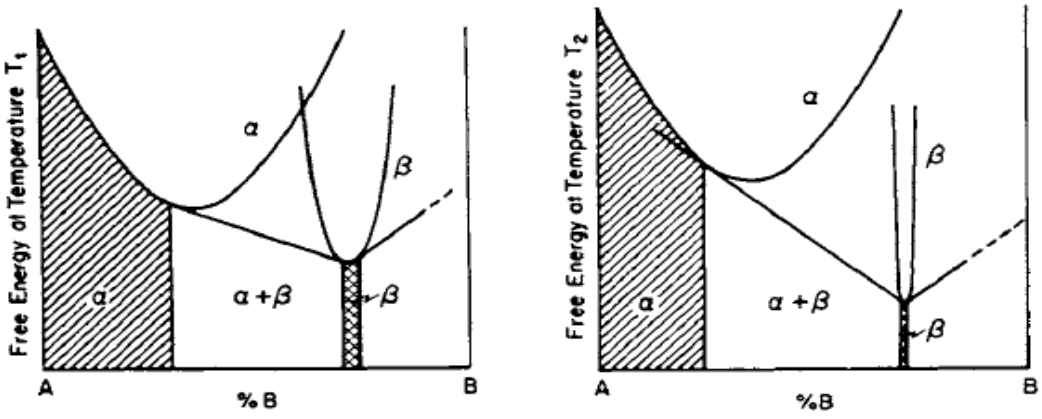

Figure 2.2 Hypothetical free energy curves demonstrating the restriction of solid solubility due to the presence of intermetallic compound. Adapted from Ref. [17].

2.2 Long Range Order and Order-Disorder Transition Temperature in Intermetallic Compounds

Considering a binary A-B alloy system composed of equal numbers of A and B atoms, if A and B atoms have a regular periodic arrangement with respect to one another, the A-B alloy is known as an *ordered* alloy. If this order remains at large distances compared to interatomic distances in a lattice, the order is called as long-range order (LRO). LRO is defined by a single parameter denoted as LRO parameter (η). This parameter lies within the range of zero (complete disorder) to unity (complete order). The structure of the alloy is fully ordered at absolute zero temperature. The degree of the order decreases with increasing temperature until a critical temperature above which the order disappears and the structure is completely disordered. This critical temperature is called as *order-disorder phase transition temperature*.

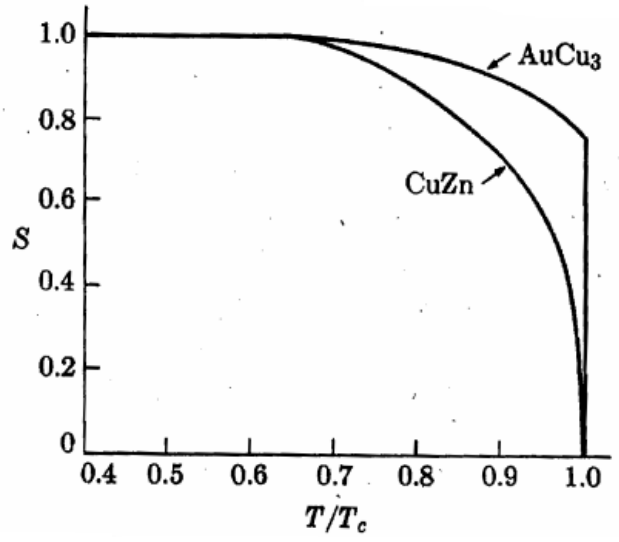

Figure 2.3 Curves of long range order variation with temperature. ($AuCu_3$ and CuZn are the examples of first-order and higher-order order-disorder transitions, respectively) Adapted from Ref. [18].

In view of thermodynamics, alloys possess the highest entropy at high temperature due to the randomness. On the contrary, phases present at low temperatures have lowest entropy and lowest energy because of the ordered state. Ordered phases at low temperature undergo a transition into disordered phases upon heating. This transition is known as *order-disorder phase transformation (transition)*. Order-disorder transitions like other transitions are classified as first-order and higher-order transitions according to the order of the derivative of the Gibbs free energy with respect to a variable, which first shows discontinuity at the transition temperature. For first order transitions, ordered and disordered phases are in equilibrium with each other and they can be differentiated. Whenever ordered and disordered phases cannot be differentiated impossibly the transition is denoted as higher-order transition [19].

2.3 Aluminides

An aluminide is a binary intermetallic compound formed between aluminium and a metallic element more electropositive than Al. High melting point, relatively low density, excellent oxidation and corrosion resistance, good high temperature

mechanical properties are the main advantages of aluminides compared to other metallic materials [1, 4, 9, 20]. These attractive properties make aluminides promising materials for high temperature structural applications [9, 10]. Important properties of the some aluminides are listed in Table 2.1. However, aluminides like other intermetallic compounds display limited fabricability, brittle fracture and poor ductility at ambient temperatures [21, 22]. Thus, their potential usage as an engineering material is restricted.

Table 2.1 Physical properties of aluminides.

Alloy	Crystal Structure	Order-Disorder Transition Temp. (°C)	Melting Point (°C)	Density (g/cm^3)	Composition with Al (at.%)
FeAl	B2	1318	1330	5.56	23.3-54.9
Fe_3Al	$D0_3$	552	1540	6.72	23.6-34.1
NiAl	B2	1638	1638	5.86	30.9-58.2
Ni_3Al	$L1_2$	1390	1390	7.50	24.7-27.7
TiAl	$L1_0$	1440	1440	3.91	47.7-69.5
Ti_3Al	$D0_{19}$	1180	1180	4.20	22.4-38.4

2.3.1 Iron Aluminides

Iron aluminides was first recognized in 1930s [23, 24] due to their unique oxidation resistance, but detailed investigations concerning the mechanical properties of iron aluminides were carried out by Cahn and co-workers in the early 1960s [25-27] . There are several iron aluminium intermetallic compounds with different composition and crystal structure in binary Fe-Al phase diagram [28] (Figure 2.4). Table 2.2 summarizes the compositions and crystal structures of iron aluminium intermetallic compounds.

Fe_2Al_9 and $FeAl_6$ are the metastable phases exist in Fe-Al system. These phases are only formed under high cooling rates. Intermetallic compounds present in the Al-rich side of the Fe-Al phase diagram, which are ε-Fe_5Al_8, $FeAl_2$, Fe_2Al_5 and $FeAl_3$, do not have any usage in engineering applications up to date due to their narrow

compositional ranges and very brittle nature. Nevertheless, intermetallic compound of the Fe-rich side of Fe-Al phase diagram, both Fe_3Al and FeAl, have considerable research attention due to their excellent oxidation and corrosion resistance, low density, relatively high melting point, good intermediate temperature strength, low material cost and conservation of strategic elements such as Cr compared to many other commercial Fe based materials such as stainless steels and cast irons [5-15]. Therefore, these materials are considered to be the potential candidates for applications as structural materials, heaters and fasteners at elevated temperatures in petrochemical industries, conventional power plants, coal conversion plants, catalytic converters and components for industrial valves and molten salt applications [29-31]. However, poor ductility and toughness at ambient temperatures, limited fabricability, poor strength and creep resistance at temperatures above 600 °C hinders the applications of iron aluminides like other ordered intermetallic compounds [8, 13, 14].

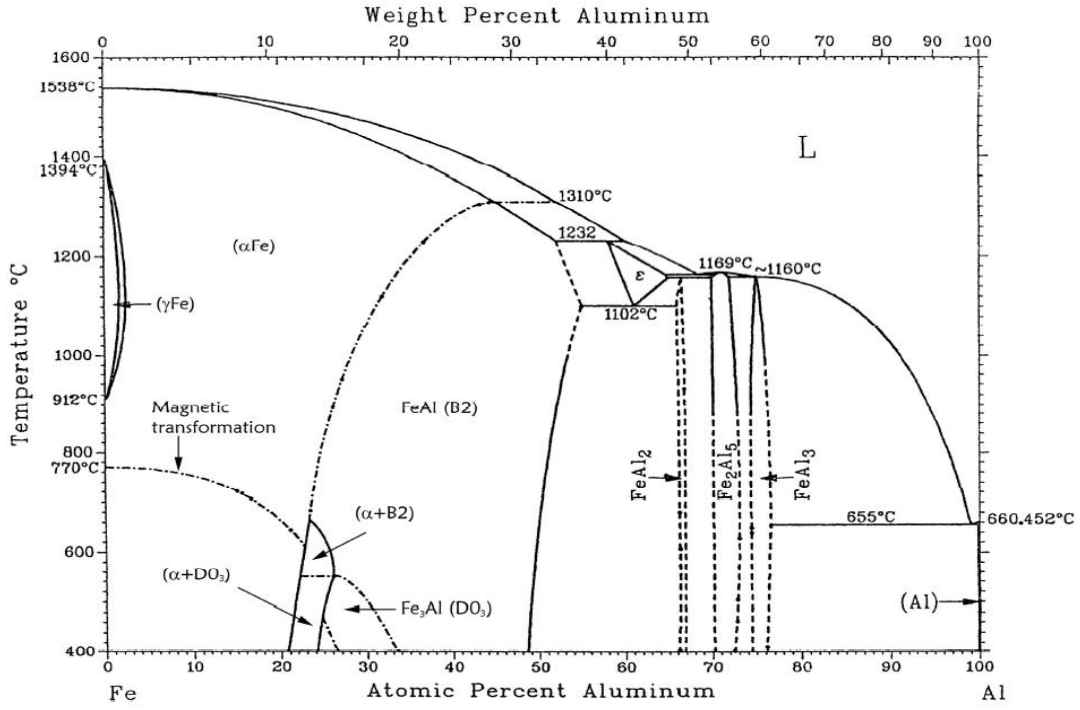

Figure 2.4 Fe-Al binary phase diagram. Adapted from Ref. [28].

Table 2.2 Crystal structures and compositions of Fe-Al intermetallic compounds present in Fe-Al binary phase diagram.

Alloy	Pearson Symbol	Space Group	Strukturbericht Designation	Composition with Al (wt.%)	Composition with Al (at.%)
Fe_3Al	cF16	Fm m	$D0_3$	13.0-20.0	23.6-34.1
FeAl	cP8	Pm m	B2	12.8-37.0	23.3-54.9
ε-Fe_5Al_8	cI52	I 3m	-	40.0-47.3	58.0-65.0
$FeAl_2$	aP18	P1	-	48.0-49.4	65.6-66.9
Fe_2Al_5	oc24	Cmcm	-	53.0-57.0	70.0-73.3
$FeAl_3$	mc102	C2/m	-	58.5-61.3	74.5-76.6
Fe_2Al_9 (m)	mP22	$P2_1/c$	$D8_d$	68.5	81.8
$FeAl_6$ (m)	oc28	$Cmc2_1$	$D2_b$	74.3	85.7

2.3.2 Fe_3Al

Fe_3Al based alloys with the $D0_3$-type of ordered crystal structure (Figure 2.5) have three different sublattices: disordered BCC (A2) structure at temperatures above 1000 °C, an ordered B2-type BCC structure at temperatures between 552 °C and 1000 °C and a perfectly ordered $D0_3$-type BCC structure at temperatures below 552 °C. The distribution of the Fe and Al among the sublattices determines the type of ordered structure. In the $D0_3$-type structure, β sites are occupied by Al atoms and other sites are occupied by Fe atoms. In the B2-type structure, Fe atoms occupy α sites, while Al atoms occupy β and γ sites. In the disordered A2 structure all sites are occupied by Al or Fe atoms randomly.

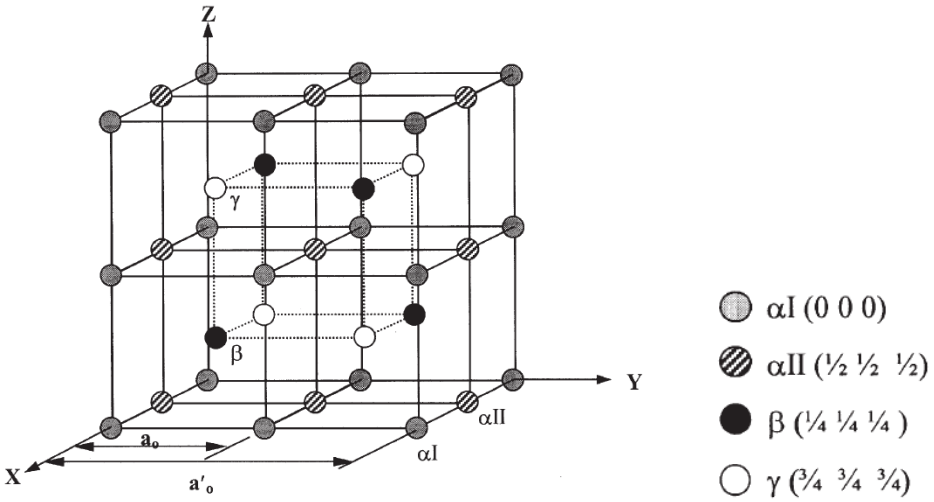

Figure 2.5 The $D0_3$-type ordered crystal structure of Fe_3Al.

2.3.3 FeAl

FeAl based alloys with the B2-type ordered crystal structure have wide range of Al concentration from 23 to 54 at.%. B2-type structure is an imperfectly ordered crystal structure in contrast to Fe_3Al. In this structure, Fe atoms are located at the corner lattice sites, whereas Al atom is located in the centre lattice site (Figure 2.6). B2-type crystal structure is stable between room temperature to 1300 °C at which it undergoes a second order order-disorder phase transition to disordered A2 structure.

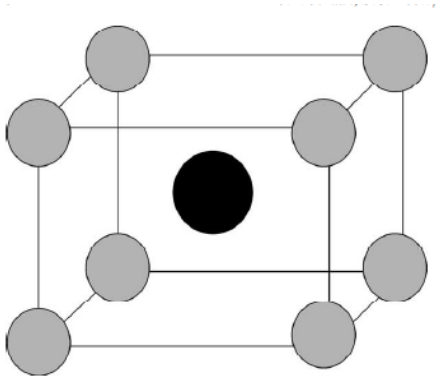

Figure 2.6 The B2-type ordered crystal structure of FeAl (grey spheres represent Fe atoms, black sphere represents Al atom).

Among iron aluminides, B2-type ordered FeAl is the most oxidation resistant alloy due to its large reservoir of Al [31]. Its wide range of Al content (23 to 54 at.%) leads to formation of stable, protective Al_2O_3 layers [32]. Moreover, FeAl has lower density, hence it has better strength to weight ratio rather than steels, Fe-based alloys and Fe_3Al. In addition, its high electrical resistivity (130-170 μΩ/cm) makes them suitable heating elements at high temperatures [31]. However, FeAl based alloys cannot find widespread engineering applications due to their brittle fracture and poor ductility at ambient temperatures [1].

2.3.4 Mechanical Properties of Iron Aluminides

Room temperature mechanical properties of Fe-Al based alloys strongly depend on their Al content, type of superlattices, deviation from alloy stoichiometry, defect concentration and test environment [16, 31].

Yield strength of the Fe-Al based alloys increases linearly with increasing Al content in the single phase α-(Fe, Al) (0-11 at.% Al) and two phase α-(Fe, Al) + Fe_3Al (11-25 at.% Al) regions up to stoichiometric Fe_3Al (25 at.%) composition [9, 11, 33, 34]. Then, the yield strength sharply drops in the single phase $D0_3$-type ordered Fe_3Al region.

Studies concerning the room temperature yield strength of B2-type ordered FeAl [35-37] showed that yield strength is independent of Al content within the composition range of 40-48 at.% Al; however, at the stoichiometric Fe-50Al composition yield stress increases markedly (> 1000 MPa). It is important to note that the steep increase in room temperature yield strength at the stoichiometric composition is directly related to the vacancy concentration. Theoretical and experimental studies illustrated that vacancy concentration show an increase with Al content and reach the maximum value near the stoichiometric composition [38, 39]. On the other hand, deviation from stoichiometry increases the anti-site defect concentration which has an important role on blocking the dislocation motion in B2-type ordered Fe-Al alloys [35, 37]. Consequently, it can be concluded that vacancy concentration is the

dominant factor influencing the mechanical properties of Fe-Al alloys compared to anti-site defect concentration [38].

$D0_3$-type ordered Fe_3Al and B2-type ordered FeAl like other intermetallic compounds are known to be very brittle at ambient temperatures. The major reasons for their brittle fracture and poor ductility have not been identified yet [40] since there is no single cause for brittleness at ambient temperatures [2]. The reasons for the poor ductility and brittleness can be the combination of several extrinsic and intrinsic factors. These factors are listed as: environment, impurity, surface finish, pest, cooling rate, slip vector, number of slip systems, difficulty in glide of dislocation and nucleation, weak grain boundary, restricted cross slip and low cleavage strength. Among these factors, environmental embrittlement is the main factor which affects the room temperature ductility. The reaction between moisture in air and Al atoms results in the formation of hydrogens that can be easily diffused into crack tips and finally embrittle the Fe aluminide.

$$2Al + 3H_2O \rightarrow Al_2O_3 + 6H \qquad (2.1)$$

Liu reported that the maximum room temperature ductility was observed in dry oxygen environment rather than other environments even in vacuum due to the formation of alumina according to the following reaction.

$$4Al + 3O_2 \rightarrow 2Al_2O_3 \qquad (2.2)$$

The formation of hydrogens is annihilated due to the reaction between aluminium and oxygen, thus ductility increases. Al concentration and temperature are the other factors affecting the hydrogen-induced embrittlement. . Iron aluminides containing higher than 38 at.% Al are less sensitive to hydrogen-induced embrittlement because of the intrinsically brittle grain boundaries of iron aluminides containing aluminium higher than 38 at.%. Concentration of the hydrogen at crack tips decreases with increasing temperature.

Conversely, although the major cause of room temperature brittleness seems to be the environmental embrittlement, Al concentration and deviation from alloy stochiometry are the significant factors that have considerable effect on ductility. Among Fe-Al alloys, $D0_3$-type ordered Fe-25Al alloy showed the highest room temperature tensile elongation of 8 % [41]. Ductility reduced with increasing Al content especially in B2-type region and finally at stoichiometric Fe-50Al composition no tensile elongation was observed [41, 42]. Studies related to the fracture surfaces of Fe-Al based alloys [21, 41-44] demonstrated that there is a relationship between fracture mode and Al content or deviation from stochiometry. The fracture mode of stoichiometric and near stoichiometric B2-type Fe-Al alloys is completely intergranular fracture, while fracture mode alters to transgranular cleavage in the Fe-rich Fe-25Al, Fe-30Al or Fe-34Al alloys. However, Fe-Al alloys containing nearly 40 at.% Al show both intergranular fracture and transgranular cleavage.

Further alloy design and development strategies including alloying, grain refinement, stabilization of ordered B2 structure, improvement of grain boundary cohesion, formation of protective surface layers, control of microstructure and suitable heat-treatment are needed in order to improve the room temperature ductility and associated hydrogen-induced embrittlement [8].

2.4 Alloying Additions to FeAl

Great research has been performed in order to investigate the effect of alloying additions on the structural and mechanical properties of FeAl based intermetallic compounds. Ternary alloying additions into B2-type ordered FeAl alloys can be classified into three groups according to their solid solubility behaviour in FeAl phase [45].

- **Class I elements**, X_I = Ni, Co, Mn, Si, Cu, Zn, Mn or Cr. These elements have large solid solubility in FeAl and they form single phase solid solutions

after homogenization. Addition of class I elements strongly increase the room temperature ductility but they do not improve the compressive strength.

- **Class II elements**, X_{II} = Zr, Hf, Nb, Ta, Ti or Re. These elements have incomplete solid solubility in FeAl even after a long homogenization treatment (175 hours) at high temperature. Formation of ternary intermetallic compounds is present. Addition of these elements doubles the compressive strength of binary iron aluminides.
- **Class III elements**, X_{III} = Mo or W, appear not to show any significant solid solubility in B2-type ordered FeAl alloys. New binary intermetallic compounds (Fe-Mo, Al-Mo, Fe-W, etc.) form and no ternary intermetallic compound forms. Addition of Mo or W result in substantial increase in compressive strength.

2.4.1 Alloying Additions forming (Fe, Al, X) solid solutions

Cr as a ternary alloying addition seems to be the most effective way for improvement of room temperature ductility of Fe-Al based alloys [9]. Extended solid solubility of Cr in both α-(Fe, Al) and B2 type FeAl phase leads to formation of solid solutions up to 50 at.% Al compositions [11].

McKamey et al. [46, 47] reported that 2 to 6 at.% Cr additions to Fe_3Al containing 28 at.% Al increases the room temperature tensile elongation by a factor of 2.5. On the other hand, they also presented that room temperature yield stress values slightly reduce with Cr addition. Alloying Fe_3Al with Cr results in the formation of fine and wavy slip lines contrary to the straight and coarse ones present in the binary Fe_3Al. These fine and wavy slip lines make the cross-slip easier from one (110) plane to another in the (110) <111> slip system. It is also observed that Cr addition changes the fracture mode from transgranular cleavage to mixed intergranular and transgranular fracture. This result indicates the increase in grain boundary and cleavage strength. Cr addition also reduces the antiphase boundary energy (APB) by increasing the spacing between dislocations in the fourfold superdislocation [46-48].

Room temperature ductility of B2-type ordered FeAl can also be enhanced by Cr additions. Li et al. [49] presented that 5 at.% Cr addition has a favourable effect on room temperature ductility of B2-type ordered Fe-36.5Al alloy without any significant change in fracture mode and slip system.

It was previously reported that 1 at.% Li or Ce additions have softening effect on Fe-40Al alloy, whereas 1 at.% Ni addition increases yield stress and reduces the room temperature ductility [50]. Munroe [51-53] studied Ni additions and it was shown that Ni has a pronounced influence on vacancy hardening nature of B2-type ordered FeAl intermetallics.

Room temperature ductility of iron aluminides can also be improved by addition of another solid solution forming ternary alloying element, Mn [54, 55]. In several studies significant enhancements were obtained in ductility of $D0_3$-type ordered Fe_3Al [56, 57] and B2-type ordered FeAl alloys [58]. Improvement of room temperature ductility by Mn can be attributed to several factors like by Cr addition including: grain refinement, reduction of APB size, easier cross-slip, alteration of fracture mode from transgranular to mixed transgranular and intergranular, improvement of cleavage strength [56].

2.4.2 Alloying Additions forming precipitates of intermetallic phases

Additions of Zr, Hf, Nb, Ta and Ti results in the formation of new intermetallic phase besides Fe-Al based phase due to the limited solid solubility of these alloying elements in Fe-Al based phases. This new phase is a ternary intermetallic compound generally called as Laves phase [11, 12, 59, 60]. Laves phases having the common composition AB_2 are the largest group of intermetallic compounds [61]. The principal advantage of Laves phase is its outstanding high temperature strength. However, hard and brittle nature at ambient temperatures is the major drawbacks of the Laves phases [62, 63].

Laves phase containing two phase Fe-Al-X intermetallics have considerable importance for structural applications at high temperatures because optimization of mechanical properties can be performed easily. Iron aluminides containing higher than 38 at.% Al are less sensitive to hydrogen-induced embrittlement because of the intrinsically brittle grain boundaries of iron aluminides containing aluminium higher than 38 at.%.. In such a process, the volume fraction of the Laves phase can be controlled by the ternary alloying element content, while the atomic order in Fe-Al matrix can be controlled by the Al content [59, 62].

Zr is a typical example of Laves phase forming ternary alloying addition. It has a very low solid solubility in the Fe-Al phases and even very small additions of Zr to Fe_3Al or FeAl cause the formation of $Zr(Fe, Al)_2$ or $Zr(Fe, Al)_{12}$ phases in the eutectic form, respectively [11, 60, 64-66]. Stein et al. [12] studied the Zr additions to disordered (A2) Fe-10Al, $D0_3$-type ordered Fe-20Al and B2-type ordered Fe-40Al alloys and it was indicated that volume fraction of hard and brittle ternary intermetallic phases increase with increasing Zr content. The yield strength of all alloys within the temperature range of room temperature to 1000 °C raises with increasing the amount of ternary phases; however, no plastic deformation was observed at the room temperature when the amount of ternary intermetallic phase exceeded a certain amount.

Nb is another ternary intermetallic Laves phase former element in Fe-Al system. Hexagonal C14-type $Nb(Fe, Al)_2$ Laves phase forms as a result of low solubility of Nb in Fe-Al alloys [67, 68]. Solubility of Nb in Fe-Al system depends on the Al content as opposed to that of Zr: higher in the B2-type FeAl region and lower in the Fe-rich side [69]. According to ternary Fe-Al-Nb phase diagram studies there is a eutectic valley lying parallel to the Fe-Al axis between (α-Fe)/FeAl and $Nb(Fe, Al)_2$ Laves phase [69-71]. The ternary eutectic compositions for the Fe-rich and Al rich sides were presented as Fe-22.8Al-9.7Nb and Fe-41.2Al-9.1 Nb or Fe-45.0Al-8.0Nb, respectively [71]. Compression tests showed that Nb additions increases the yield strength of Fe-26Al alloy within the temperature range of room temperature to 1000 °C which is similar with observations made for Fe-Al-Zr alloys [72]. However, more

recent studies [73, 74] demonstrated that enhanced room temperature plasticity with high strength was observed for Fe-40Al-6Nb alloy. The improved room temperature mechanical properties can be attributed to the ultrafine eutectic composite structure of Fe-40Al-6Nb alloy containing micron scale Fe-Al based dendrites and nanoscale Nb(Fe, Al)$_2$ Laves lamella or fibres exist in eutectic mixture.

Ta has also low solubility and C14-type Ta(Fe, Al)$_2$ Laves phase forms at different amounts depending on the Al content when Ta is added to Fe_3Al or FeAl based alloys [11, 59, 75, 76]. Although Ta as well as other Laves phase former transition elements acts as a strengthener both at ambient and high temperature, its strengthening influence is different from that of others' due to the different ordering and microstructural features. Risanti and Sauthoff reported [59] that different type of Ta(Fe, Al)$_2$ Laves phase morphologies can be observed depending on the Al and Ta content. 2 at.% Ta addition to Fe-rich disordered (A2) Fe-16Al and $D0_3$-type ordered Fe-25Al results in the formation of Ta(Fe, Al)$_2$ Laves phase only at grain boundaries, while 3 at.% Ta addition leads to formation of Laves phase preferentially at grain boundaries and within the grains. Laves phase becomes the main component of eutectic phase mixture with Fe-rich Fe-Al based phase when the Ta content was further increased to 6 at.%. However, no eutectic phase mixture was detected with same amounts of Ta were added to Al-rich B2-type ordered Fe-45Al alloys.

Although C14-type Hf(Fe, Al)$_2$ Laves and $ThMn_{12}$-type ternary intermetallic $HfFe_6Al_6$ τ_1 phases, present in Fe-Al-Hf ternary phase diagram [77], can be considered as possible strengtheners , there are few reports about the alloying and strengthening Fe-Al based alloys with Hf. Gaydosh et al. [22] studied mechanical properties of Fe-Al alloys with Hf addition. They indicated that 1 at.% Hf addition to binary B2-type ordered Fe-40Al alloy resulted in pronounced improvements in yield strength like other ternary intermetallic phase forming alloying elements; however, room temperature ductility decreases because of the formation of $HfFe_6Al_6$ τ_1 phase.

The last ternary intermetallic forming element is Ti. Fe-Al-Ti alloys are attractive since various strengthening mechanisms exist in the ternary Fe-Al-Ti system [11, 78,

79]. $L2_1$-type ordered Fe_2TiAl Heusler phase, C14-type $Ti(Fe, Al)_2$ Laves phase and $Mn_{23}Th_6$-type cubic τ_2 phase are the possible ternary intermetallic phases in Fe-Al-Ti system. Important increase in yield strength up to 1100 °C temperatures was achieved by the precipitation of ternary intermetallic phases in both Fe-rich and Al-rich Fe-Al-Ti alloys [78-81].

Finally, all ternary intermetallic phase forming alloying elements have significant effects on yield strength and tensile or compressive strength of Fe-Al based alloys as they offer precipitation of two or more hard and brittle ternary intermetallic phases. However, room temperature brittleness except for Nb addition is still a big problem that should be overcome. Formation of borides or carbides by co-doping of ternary intermetallic phase forming alloying elements with C or B and additional thermal treatments may be beneficial for improving the room temperature ductility.

Fe-Al based alloys can also be strengthened by binary intermetallic compounds besides Laves phase as in the Fe-Al-Mo or Fe-Al-W systems [11]. In recent studies main concern is devoted on the investigation of phase relationships, microstructures and mechanical properties of Fe-Al-Mo alloys instead of Fe-Al-W alloys because of the extremely high melting temperature of W (~3422 °C). Eumann et al. [82, 83] investigated the phase equilibrium in ternary Fe-Al-Mo system and they demonstrated that hexagonal Fe_7Mo_6 (μ) and cubic Mo_3Al are the possible precipitates that can be formed when Mo is added to disordered (A2) or ordered Fe-Al ($D0_3$-type Fe_3Al and B2-type FeAl) based alloys. The same group of authors also studied [84] the strengthening effect of Mo_3Al on $D0_3$-type Fe_3Al and B2-type FeAl based alloys and it was shown that volume fraction of Mo_3Al precipitates have significant effect on increasing the yield strength and compressive strength of $D0_3$-type ordered Fe-30Al and B2-type ordered Fe-40Al alloys. They also reported that detrimental effect of Mo_3Al formation on room temperature ductility can be improved by subsequent heat-treatment.

2.5 Oxidation Resistance of Iron Aluminides

High temperature oxidation and corrosion resistance of metallic materials originally depend on their capability of forming a slow-growing, protective, adherent and mechanically stable external chromia (Cr_2O_3), silica (SiO_2) and alumina (Al_2O_3) layers on their surface [30, 85, 86]. These three oxides are the only ones that display sufficient protection of their metallic substrate against oxidation and corrosion. Among these oxides alumina has several advantages over chromia and silica including slower growth rate and formation at even highly low oxygen partial pressures in single oxidant environments [30, 85]. Moreover, alumina scales prevent oxidation and corrosion of metallic substrates by hindering the diffusion of elements which expedite corrosion on the surface such as S, Cl and alkalis in the multi oxidant environment [30].

Oxidation resistance of iron aluminides are essentially related to their Al content. It is known that 15 at.% Al is the lowest concentration in order to repress internal oxidation and form stable alumina scales on surface of iron aluminides [87, 88]. Thus, most well-known iron aluminides, Fe_3Al and FeAl, have Al amount higher than the critical composition and they are considered as the suitable materials at oxidizing environments. Among iron aluminides and commercial iron based alloys, B2-type FeAl intermetallic compound has the best oxidation resistance due to its higher Al content.

α- Al_2O_3, also named as corundum, is the only thermodynamically stable oxide in Al-O system and it has a trigonal crystal structure and a melting temperature of 2047 °C. Alternatively, alumina exists in metastable forms, namely γ, δ and θ aluminas, depending on temperature [30]. The temperature stability of stable and metastable aluminas as follows:

(2.3)

Each metastable form of alumina has a unique crystal structure and physical properties. However, all these forms are fast-growing, less protective and more porous [89-93].

Table 2.3 Densities and crystal structures of different forms of aluminas. Adapted from Ref. [94].

Polymorph	Density (g/cm^3)	Crystal structure
Amorphous	3.0-3.1	-
γ- Al_2O_3	3.60-3.67	Cubic spinel
δ- Al_2O_3	3.60-3.67	Tetragonal or orthorhombic
θ- Al_2O_3	3.60-3.67	Monoclinic
α- Al_2O_3	3.99	Trigonal

Alumina is one of the most stable oxides in nature according to well-known Ellingham diagram (Figure 2.7) and it is too difficult to reduce it when it is formed once. On the other hand, there must be a strong adhesion between alumina scale and substrate in order to exhibit a strong protection of iron aluminides against oxidation at high temperatures.

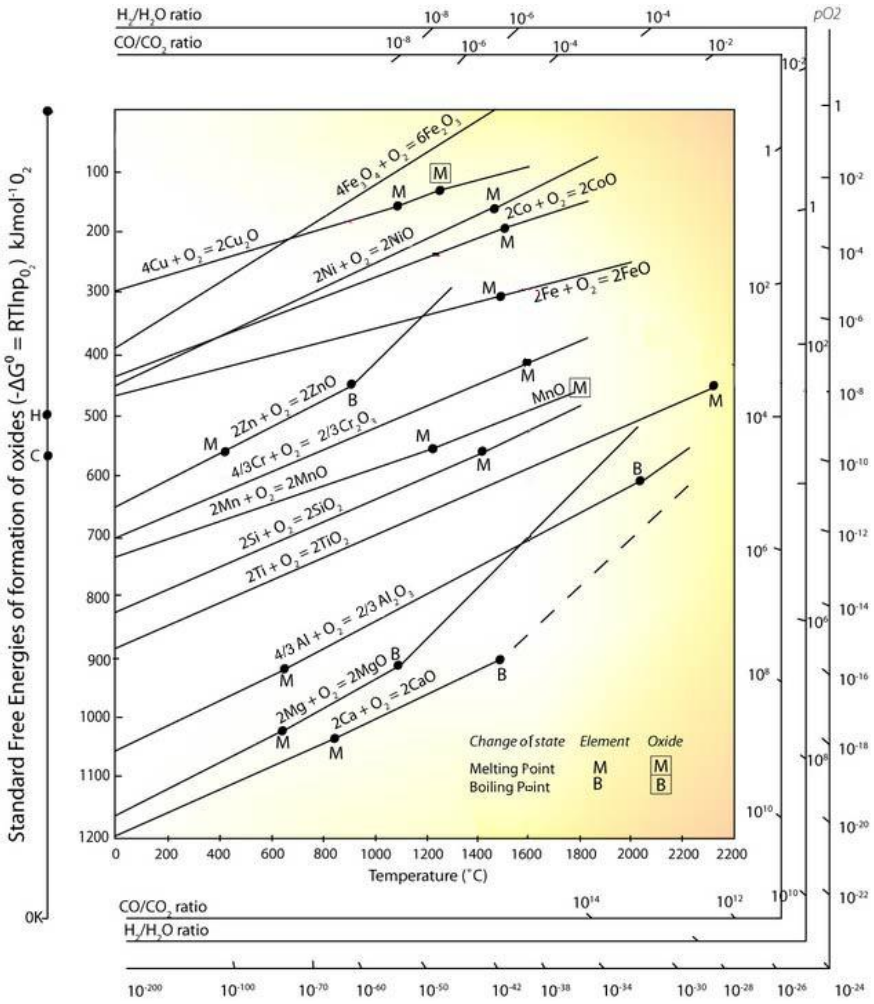

Figure 2.7 The Ellingham diagram for selected oxides.

Failure of alumina scales due to the thermal expansion mismatch between alumina and substrate and generation of thermal stresses during cooling is the most important problems of alumina forming materials such as iron aluminides. Linear thermal expansion coefficients for some materials are listed in Table 2.4. It is important to note that large thermal expansion mismatches are present between the alumina and iron aluminides based on Fe_3Al and FeAl.

Table 2.4 Coefficient of thermal expansion (CTE) for selected materials. Adapted from Ref. [95].

Material	CTE, $\alpha_L * 10^{-5}$, (1/°C)
FeAl	2.1
Fe_3Al	1.2
Zinc & its Alloys	3.5
Lead & its Alloys	2.9
Magnesium & its Alloys	2.8
Aluminum & its Alloys	2.5
Steel Stainless Austenitic (304)	1.73
Steel Stainless Austenitic (310)	1.44
Steel Stainless Austenitic (316)	1.6
Steel Stainless Ferritic	1.1
Steel Stainless Martensitic	1.2
High Temperature Steels	1.4
Ultra High Strength Steels	1.4
Age Hardenable Stainless Steels	1.5
Nodular or Ductile Cast Irons	1.9
Malleable Irons	1.3
Gray Cast Irons	1.1
Alumina	0.9

Spallation of protective alumina scales, which is schematically shown in Figure 2.8, during cooling, is the major problem of iron aluminides. Studies showed that [30, 96, 97] mechanical instability of alumina layers such as cracking, delamination and spallation results from several reasons including vacancy and void formation at the surface, impurity segregation to aluminide-alumina interface, poor adhesion between alumina and aluminide, large thermal expansion mismatch and thermal stress formation.

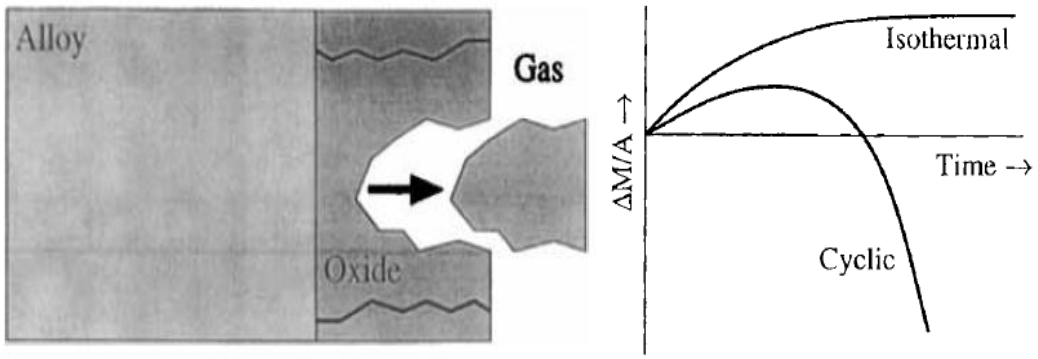

Figure 2.8 Schematic diagram showing the cracking and spallation of oxide layer and comparison of isothermal and cycling oxidation kinetics. Adapted from Ref. [95].

Another drawback of iron aluminides is the diffusion of Fe atoms to the scale and generation of Fe oxide nodules on the scale surface. These nodules finally merge and envelope the whole surface. This circumstance thickens the alumina scale and results in the spallation of alumina layers independent of whether alumina is stable or not.

Doping iron aluminides with ternary alloying elements is the most effective in order to increase their oxidation and scale spallation resistance. Although the additions of Cr to Fe_3Al intermetallic compound have beneficial effects on mechanical properties [46, 47], studies showed that Cr has a detrimental effect on high temperature oxidation behaviour of Fe_3Al [98-101]. Babu et al. [99] reported that additions of Cr to Fe_3Al deteriorate the oxidation resistance by increasing the mass gain in the early stages of oxidation as a result of the generation of chromia. Velon et al. [100] also

observed that 2 or 4 at.% Cr additions to Fe_3Al increases the oxide growth rate in the initial stages of oxidation at 500 °C due to the chromia formation. Co-existence of alumina and chromia is not beneficial to oxidation behaviour since chromia favours the diffusion of Fe atoms to oxide surface and leads to formation of iron oxide nodules. Moreover, it was presented that [98] 10 at.% Cr addition to Fe_3Al increased the mass gain in the first stages of oxidation at 800 and 900 °C.

Detrimental effect of C to oxidation resistance of Fe-Al alloys in the temperature range 700-1000 °C was also presented in several studies [102, 103]. Although the mechanism behind the negative effects of carbides is not entirely understood, carbide containing iron aluminides are more sensitive to oxidation than the carbide free ones.

The scale adherence and high temperature oxidation behaviour of iron aluminides can be strongly strengthened by Ti additions [99, 104]. Studies showed that Ti containing Fe_3Al intermetallic compounds have higher parabolic rate constants and more adherent scale with equiaxed alumina grains [99]. Additionally, Li et al. [104] investigated the Ti addition on the high temperature oxidation resistance of B2 type FeAl and reported many advantageous effects which can be listed as follows:

- Formation of another stable and protective scale of TiO besides Al_2O_3
- Increased scale adherence and scale spallation resistance due to presence of TiO
- Less thermal expansion mismatch between FeAl and TiO
- Enhancement of oxide scale toughness

All these positive influences of Ti additions decrease the possibility of generation of thermal stresses during cooling and retard the failure of the protective oxide scale. Oxidation and scale spallation behaviour of iron aluminides can also be modified by additions of reactive elements such as Y and Zr. Although the oxidation rates of Y-doped iron aluminides did not altered intrinsically, scale adhesion to substrate improved significantly [105, 106]. Y addition reduced the stresses formed during

cooling by changing the diffusion mechanism of oxide from counter current diffusion of Al and O to oxygen diffusion. This alteration then resulted in the generation of pegs at the scale-substrate interface and improvement of scale adhesion [105-107]. Xu and Gao [107] presented that Zr additions enhanced the scale spallation resistance of iron aluminides similar to Y additions. Neither any spallation nor failure of the scale was observed for Zr-doped alloys.

CHAPTER 3

EXPERIMENTAL PROCEDURE

3.1 Raw Materials

The samples of Fe-Al-X alloys were prepared by mixing the appropriate amounts of high purity constituents obtained from Alfa Aesar. The purities of the constituents is given in Table 3.1.

Table 3.1 Purities of constituent elements (wt.%).

Element	Purity (%)
Fe	99.97
Al	99.9
B	99.5
Cr	99.2
Hf	99.7
Mn	99.9
Mo	99.95
Ni	99.9
Nb	99.6
Ta	99.95
Ti	99.9
W	99.95
Zr	99.8

In this thesis, $Fe_{50}Al_{50-n}X_n$ alloys were investigated with X= Cr, Hf, Mn, Mo, Nb, Ta, Ti and Zr up to 9 at.% concentrations and with X= B, Ni and W up to 5 at.% concentrations, respectively.

3.2 Fabrication of the Samples

3.2.1 Arc-Melting

The samples of $Fe_{50}Al_{50-n}X_n$ alloys with 15 g mass were produced by first arc-melting (Edmund Buehler Arc Melter (Figure 3.1)) using a non-consumable tungsten electrode and a water-cooled copper tray in high-purity argon atmosphere. Zirconium was used as an O getter during the melting process. The alloys were re-melted three to four times in order to achieve complete homogeneity. The weight loss during the arc-melting process was smaller than 0.5 wt. %.

Figure 3.1 The arc-melter used for fabrication of samples.

3.2.2 Suction Casting

The samples of $Fe_{50}Al_{50-n}X_n$ alloys, where X= Cr, Mn, Mo, Nb and Ta were fabricated in the form of cylindrical rods (Figure 3.2) with diameter of 3 mm and length of 150 mm via suction casting technique from arc-melted ingots in order to obtain standard mechanical test specimens. The suction casting unit is equipped into Edmund Buehler Arc Melter.

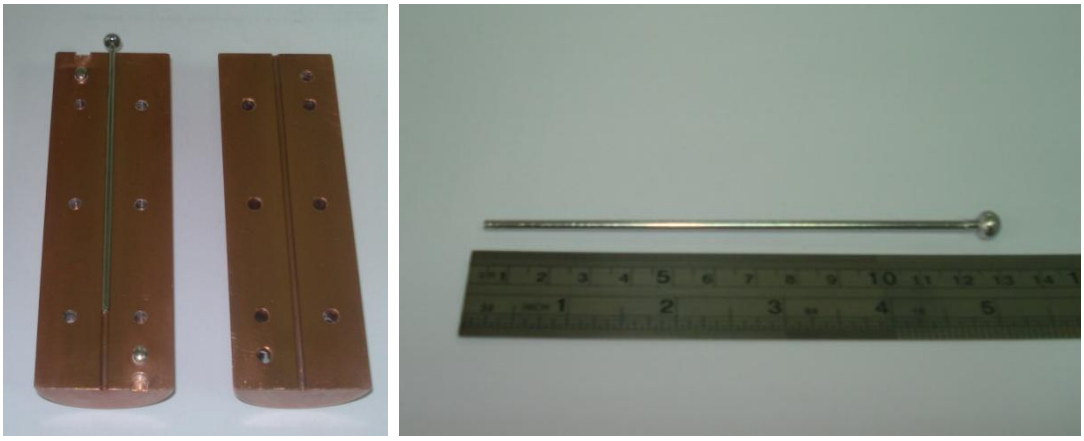

Figure 3.2 Copper mold and cylindrical rods produced by suction casting.

3.2.3 Heat-Treatment

The arc-melted samples were subjected to homogenization and annealing in order to attain highly ordered state in $Fe_{50}Al_{50-n}X_n$ alloys. The homogenization was performed at 1000 °C for 24 h and then samples were annealed at 400 °C for 168 h, followed by furnace cooling in order to avoid cracking. The samples were encapsulated in evacuated quartz tubes which were filled with argon gas.

3.3 Characterization of the Samples

3.3.1 X-ray Diffraction

The phase analyses of the samples were performed by X-ray diffraction (XRD) analyses using a Rigaku D/Max-2200 PC diffractometer with Cu-Kα radiation of a wavelength of 1.540562 Å for the angle range 2θ = 25°-100° with continuous recording with a scanning rate of 2°/min and a step size of 0.02°.

3.3.2 Scanning Electron Microscopy

The microstructural examination of the samples was performed using a Jeol Jsm 6400 model and Fei Nova Nano 430 Field Emission Gun (FEG) scanning electron microscope (SEM). For the microstructural examinations, samples were ground (up to 1200 grit), polished and etched in Ti_2 solution (68 ml glycerin, 16 ml 70% HNO_3 and 16 ml 40% HF).

The compositions of the samples were verified through energy dispersive X-ray analysis (EDS) using a SEM equipped with a Noran System 6 X-Ray Microanalysis System.

3.3.3 Differential Scanning Calorimetry

Thermal analysis measurements of the samples were performed with a Setaram Setsys–16/18 (Figure 3.3) differential scanning calorimeter (DSC). The samples of 15-30 mg weight were heated up in alumina crucibles under an argon atmosphere from room temperature to 1500 °C at a constant heating rate of 10 °C/min. Different heating rates (10, 20 and 30 °C/min) were employed in order to perform thermo-kinetic studies. Temperature calibration was performed using certified samples of Al, Zn, Ag, Au and Ni. The accuracy of the temperature calibration was ±1 K.

Figure 3.3 Setaram Setsys–16/18 DSC used in the thermal analysis measurements.

3.3.4 Mechanical Testing

The room temperature mechanical properties of as-cast and heat-treated alloys were investigated by means of compression tests using an Instron 5582 universal testing machine at a strain rate of 10^{-4} s^{-1} according to ASTM E9-09 standards (Standard Test Methods of Compression Testing of Metallic Materials at Room Temperature). Cylindrical specimens of 3 mm diameter and 4.5 mm length were cut by spark erosion and any surface layers were removed by grinding prior to testing. The yield stress was determined as 0.2% proof stress in uniaxial compression. Eight specimens were considered in tests. Samples having deviations due to the artifacts such as voids and cracks were excluded.

3.3.5 Microhardness Measurements

Vickers microhardness measurements were performed using a Shimadzu-2 Micro Hardness Tester under a load of 500 g. The mean hardness values were determined by averaging 10 measurements on each sample.

3.3.6 Vibrating Sample Magnetometer

Magnetic measurements of the samples were carried out with an ADE Magnetics EV/9 Vibrating Sample Magnetometer (VSM) under a maximum applied magnetic field of 30000 Oe (3.0 Tesla) and the Curie temperature (T_c) was determined as minimum point of (dM/dT) versus temperature curve under a constant magnetic field of 500 Oe.

3.4 Oxidation Measurements

3.4.1 Sample Preparation

The samples for cyclic oxidation experiments were cut from the ingot to the size of 3 x 6 x 1 mm^3 by Buehler IsoMet® 4000 Precision Saw. Before testing, the samples were ground by SiC emery papers up to 1200 grit, polished with Al_2O_3 powders or diamond paste of 3 and 1 μm in size to obtain mirror like finish, ultrasonically cleaned in an acetone or methanol-benzene solution and finally dried in air.

3.4.2 Cyclic Oxidation Test

Cyclic oxidation tests were carried in a Muffle (chamber) furnace (Protherm PLF 130/9 model 1300 °C maximum temperature) at 800 and 900 °C in laboratory air. One cycle consists of heating the sample to 800 or 900 °C at a heating rate of 10 K/min, holding at 800 or 900 °C for 24 hours and fast cooling to room temperature, which is approximately 20 minutes. After being cooled to room temperature, measuring the mass change using an electronic balance with an accuracy of 0.01 mg.

CHAPTER 4

EFFECT OF TERNARY ALLOYING ADDITIONS ON ORDERING CHARACTERISTICS OF FeAl INTERMETALLIC COMPOUNDS

The mechanical properties of Fe-Al intermetallics strongly depend on deviation from alloy stoichiometry and type and content of ternary alloying additions [45]. However, the specific physical and mechanical properties of iron aluminides are also attributed to the $D0_3$ and/or B2 type of long-range ordered (LRO) superlattices [5, 6] and the arrangement of ternary alloying element atoms in the submicro volumes of these ordered superstructures. Furthermore, the arrangement and distribution of ternary alloying additions on the sublattices of these ordered superstructures have significant effect on the magnitude of order-order and order-disorder phase transformation temperatures of Fe-Al intermetallics [16].

The effects of ternary alloying additions on order-disorder phase transformation temperature and the characteristics of atomic short range order in various types of ordered aluminides have been analysed by combining the statistico-thermodynamical theory of ordering with the electronic theory of alloys in pseudopotential approximation [16, 108-118]. A good qualitative agreement with available experimental data in the literature have been obtained for $L1_2$-type, DO_3-type, B2-type and $L1_0$-type ordered intermetallics of Ni_3Al [109], Fe_3Al [110-112, 115], FeAl [16, 113] and γ-TiAl [114] respectively. Although a great deal of experimental work has been performed on the effects of ternary alloying additions for Ni_3Al and Fe_3Al intermetallics [119-123], little information is provided in the literature on the ordering characteristics, especially B2↔A2 order-disorder transformation temperatures, of Fe-Al-X alloys transformation nearly 50 at.% Al [11, 16, 45].

Therefore, it is of research interest to investigate the effect of ternary alloying elements additions on the B2↔A2 order-disorder transformation temperatures of $Fe_{50}Al_{50-n}X_n$ intermetallics with B2-type ordered structure. Moreover, effort has also been directed towards to provide experimental data to confirm the validity of theoretical model proposed for single phase $Fe_{50}Al_{50-n}X_n$ ternary intermetallics [16].

4.1 Microstructure and Phase Analysis

Table 4.1 lists the nominal and actual compositions of as-cast and heat-treated $Fe_{50}Al_{49}X_1$ alloys. The microstructures of binary stoichiometric FeAl and ternary $Fe_{50}Al_{49}X_1$ alloys display single phase solid solutions having equiaxed coarse grain structures in as-cast and heat treated conditions. The examples of these almost similar microstructures are given in Figure 4.1 for binary and $Fe_{50}Al_{49}X_1$ alloys. However, small amounts of second phase particles, which preferentially form along the grain boundaries, tend to exist in alloys containing X = Mo, W, Ti and Ta elements.

Table 4.1 Nominal and actual compositions of $Fe_{50}Al_{49}X_1$ samples.

Nominal composition (at.%)	EDS analysis (at.%)					
	as-cast			heat-treated		
	Fe	Al	X	Fe	Al	X
Fe-50Al	50.2 ± 0.2	49.8 ± 0.2	-	50.4 ± 0.2	49.6 ± 0.2	-
Fe-49Al-1Cr	50.2 ± 0.2	48.6 ± 0.3	1.2 ± 0.1	50.2 ± 0.2	48.7 ± 0.2	1.1 ± 0.1
Fe-49Al-1Mn	50.0 ± 0.3	49.2 ± 0.3	0.8 ± 0.2	51.3 ± 0.3	47.7 ± 0.2	1.0 ± 0.1
Fe-49Al-1Ni	50.1 ± 0.3	49.0 ± 0.3	0.9 ± 0.2	50.1 ± 0.1	48.9 ± 0.2	1.0 ± 0.1
Fe-49Al-1Ti	52.1 ± 0.6	46.9 ± 0.6	1.0 ± 0.2	52.0 ± 0.5	47.0 ± 0.2	1.0 ± 0.1
Fe-49Al-1Ta	49.7 ± 0.2	49.4 ± 0.3	0.9 ± 0.1	49.8 ± 0.2	49.0 ± 0.2	1.2 ± 0.2
Fe-49Al-1Mo	50.2 ± 0.2	48.7 ± 0.2	1.1 ± 0.1	50.7 ± 0.2	48.3 ± 0.3	1.0 ± 0.1
Fe-49Al-1W	51.4 ± 0.3	47.7 ± 0.3	0.9 ± 0.2	51.5 ± 0.4	47.6 ± 0.4	0.9 ± 0.1

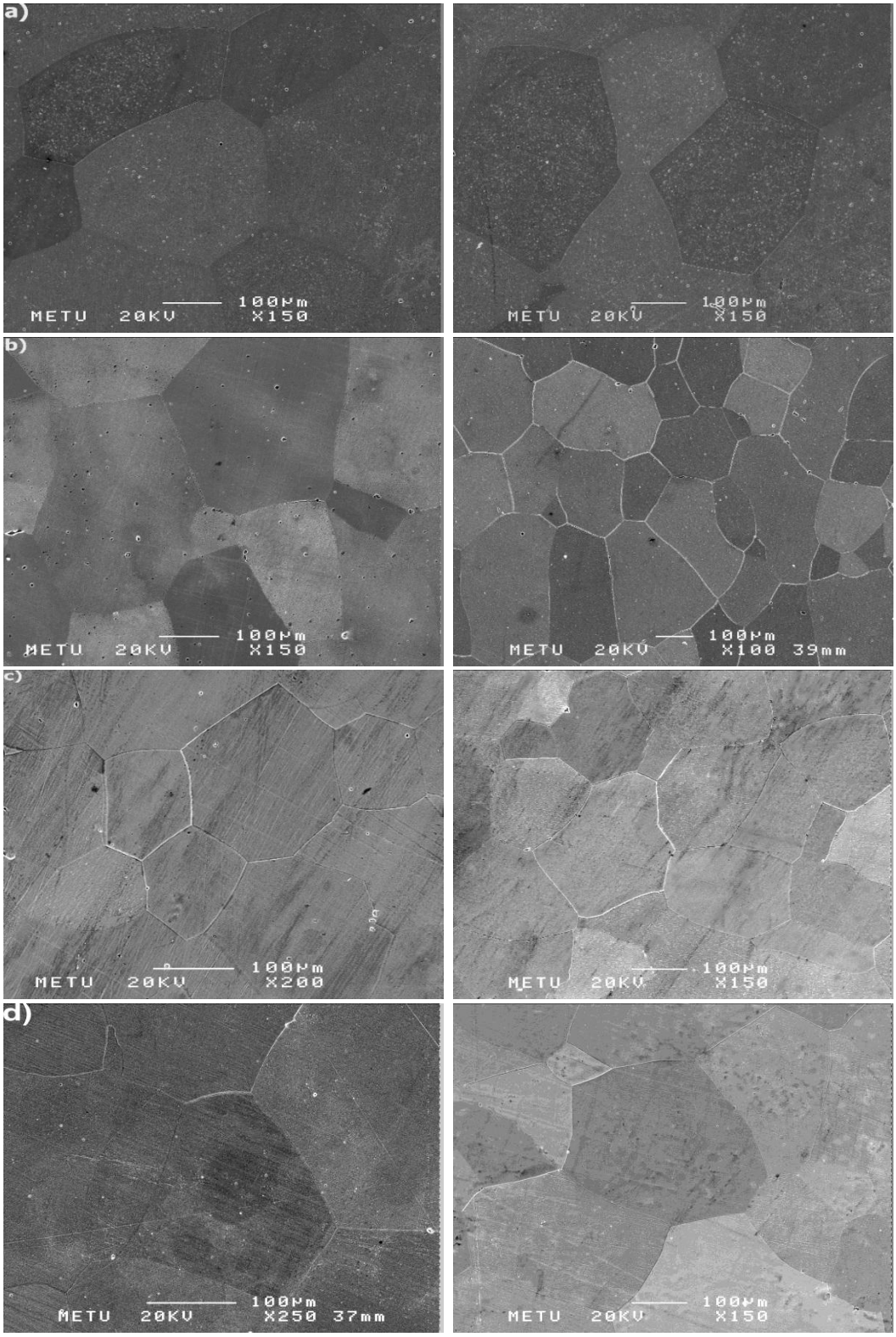

Figure 4.1 SEM micrographs of as-cast and heat-treated (right-side) $Fe_{50}Al_{50-n}X_n$ alloys; (a) binary, X = (b) Cr, (c) Mn, (d) Ni, (e) Ti, (f) Ta, (g) Mo and (h) W.

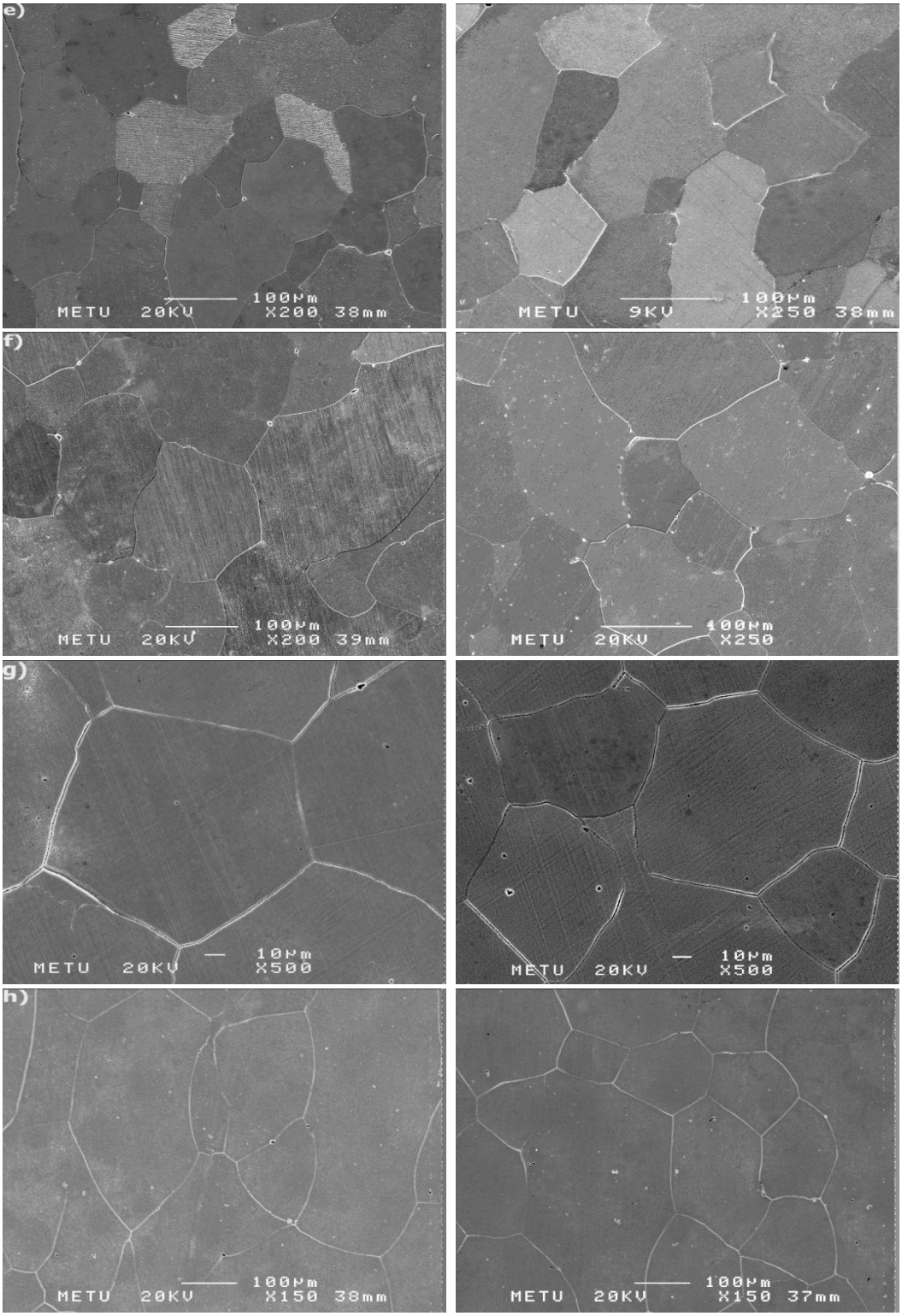

Figure 4.1 (cont'd) SEM micrographs of as-cast and heat-treated (right-side) $Fe_{50}Al_{50-n}X_n$ alloys; (a) binary, X = (b) Cr, (c) Mn, (d) Ni, (e) Ti, (f) Ta, (g) Mo and (h) W.

The formation of these second phase particles would be attributed to their low and/or limited solid solubility in FeAl phase [11, 45] and could not be detected by XRD analyses due to their small volume fractions. However, high magnification SEM studies coupled with EDS analysis (Figure 4.2) confirm the existence of the X-rich second phase particles in as-cast and heat-treated $Fe_{50}Al_{49}X_1$ (X = Mo, W, Ta, Ti) alloys. Moreover, the arrangement of these intrinsically hard and brittle second phase particles eventually develop continuous networks along the grain boundaries where intercrystalline decohesion is observed. This seems to be one of the major reasons for poor ductility behavior of these alloys. The volume fractions of these second phase particles increase with further addition of X content (n > 1 at.%). This increase leads to formation of second phase particles not only along the grain boundaries but also within the grain interior.

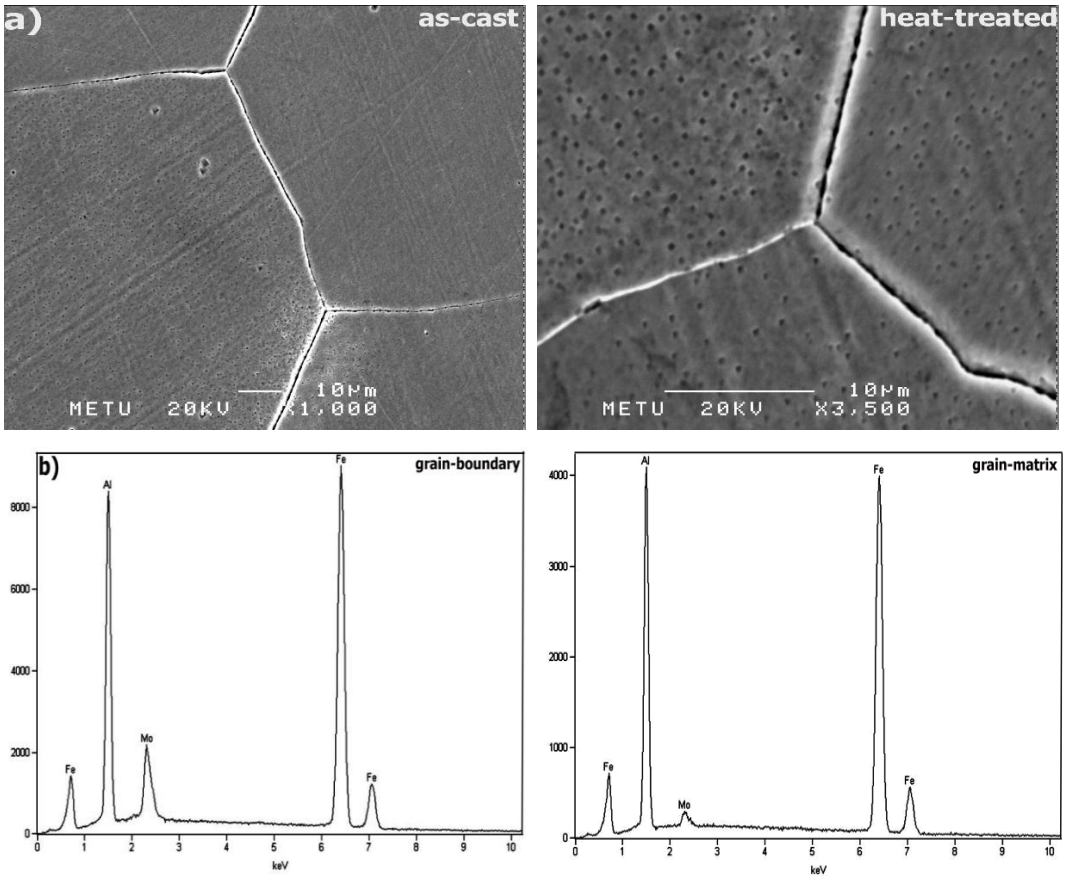

Figure 4.2 (a) SEM micrographs of $Fe_{50}Al_{49}Mo_1$ alloys at high magnification, and (b) EDS spectrum of as-cast $Fe_{50}Al_{49}Mo_1$ alloy.

The solid solubility behavior of ternary alloying additions in B2-type FeAl alloys may be ascribed to the site occupancy characteristics of the X alloying elements. It is interesting to note that these alloying elements that can readily form second phase particles in the microstructure have been predicted to preferentially substitute Fe sublattice sites in B2 type ordered Fe-Al intermetallics [16].

XRD analyses of as-cast and heat-treated $Fe_{0.5}Al_{0.49}X_{0.01}$ alloys reveal almost the same diffraction pattern as that of the stoichiometric binary FeAl alloy and prove the existence of single phase B2 type ordered FeAl phase (Figure 4.3) in all alloys under investigation. The relative intensities of diffraction lines are comparatively larger for the heat-treated than as-cast alloys due to the homogenization and ordering heat-treatment described above.

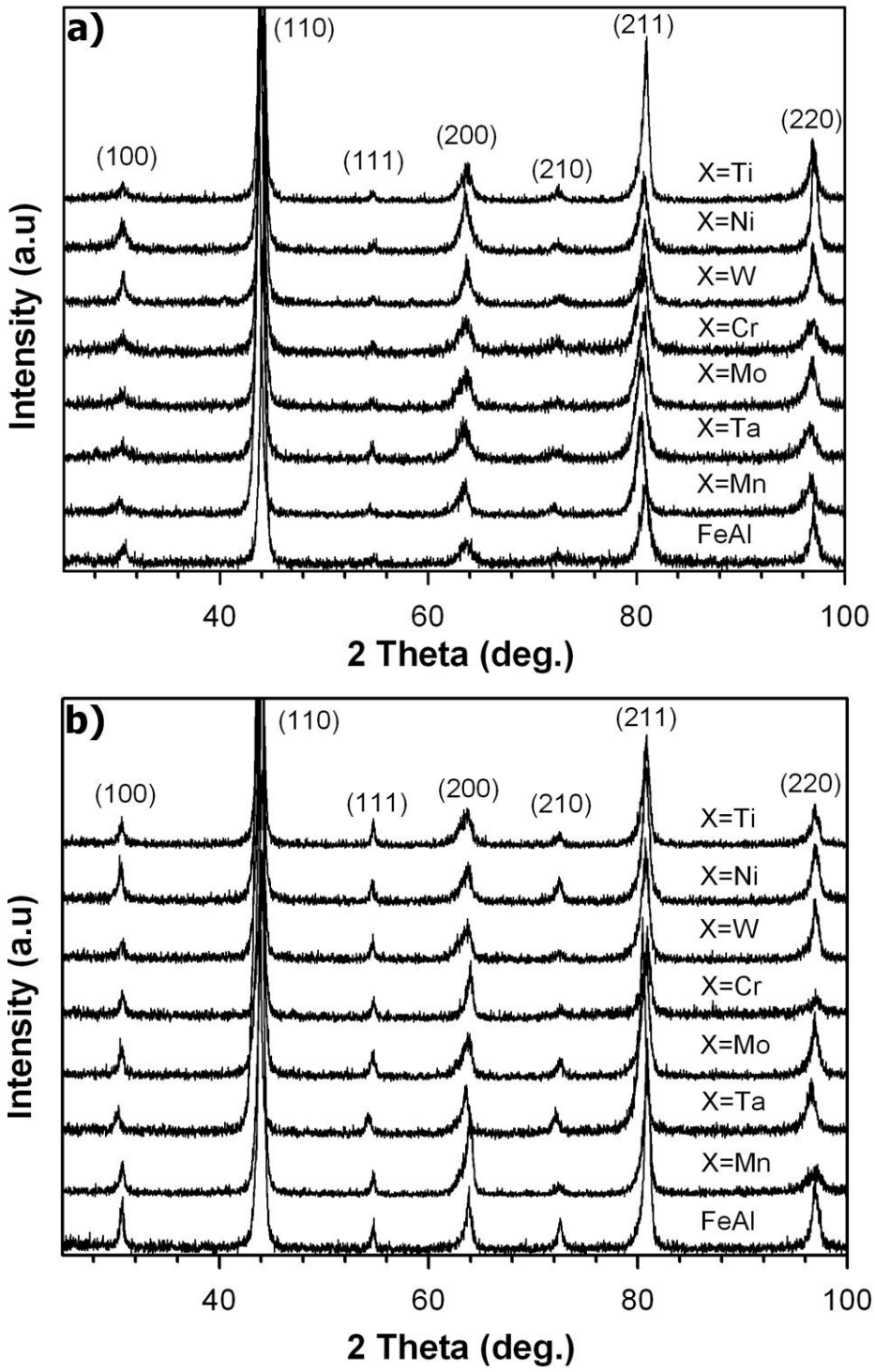

Figure 4.3 XRD patterns of (a) as-cast and (b) heat-treated $Fe_{50}Al_{50-n}X_n$ alloys.

Success of the ordering heat treatment procedure and consequently the extent of the atomic ordering may be evaluated by calculating the long range ordering (LRO) parameter, η, for the as-cast and heat-treated binary stoichiometric FeAl alloys. LRO parameters, η, have been calculated on the base of XRD results given in Figure 4.4 by employing following set of equations [124];

$$\ln \eta^2 = -(\ln y_F - \ln y_{SS}) \tag{4.1}$$

where,

$$\ln y_F = \ln \frac{I_F}{4mLP\left[(c_{Al} f_{Al} + c_{Fe} f_{Fe})^2 + (c_{Al}\Delta f_{Al} + c_{Fe}\Delta f_{Fe})^2\right]} \tag{4.2}$$

and

$$\ln y_{SS} = \ln \frac{I_{SS}}{mLP\left[(f_{Al} - f_{Fe})^2 + (\Delta f_{Al} - \Delta f_{Fe})^2\right]} \tag{4.3}$$

where I_F and I_{SS} are the integrated intensities of the fundamental and superstructure diffraction lines, respectively, m is the multiplicity factor, LP is the Lorentz Polarization factor, c_{Al} , f_{Al} , Δf_{Al} and c_{Fe} , f_{Fe} , Δf_{Fe} are the atomic fraction, atomic scattering factors and scattering-factor corrections of the Al and Fe atoms, respectively.

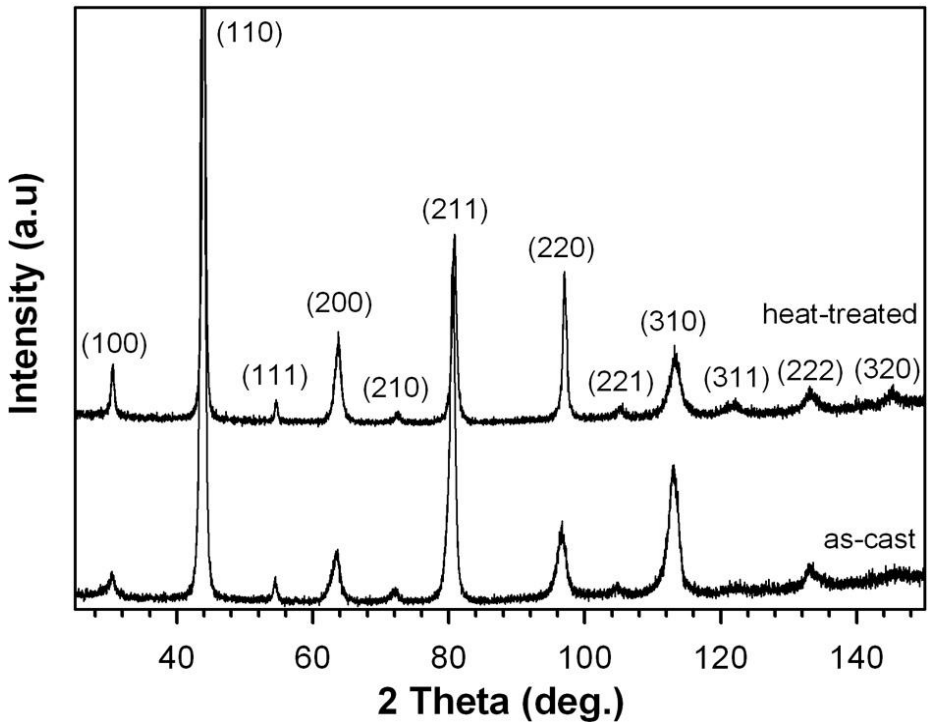

Figure 4.4 XRD patterns of binary as-cast and heat-treated FeAl alloys used for LRO parameter determination.

LRO parameters calculated based on Equations (4.1)-(4.3) have been found to be 0.48 and 0.83 for as-cast and heat-treated FeAl alloys, respectively. The presence of the superstructure diffraction lines and the experimentally determined magnitude of the LRO parameter for heat-treated binary FeAl alloy suggest the existence of not fully but highly ordered B2-type crystal structure. Fully ordered structure having $\eta = 1.0$ could not be achieved because of the presence of rather coarse (> 200 μm) equiaxed grains, which tends to reduce the intensities of the superstructure diffraction lines [125].

4.2 Determination of B2↔A2 Order-Disorder Phase Transition Temperatures

It is well known that transformation of B2-type ordered FeAl phase to the disordered A2-type phase occurs through a second order transition in the composition range between 23 and 45 at.% Al [28, 126]. However, alloys under investigation having Al

content around 50 at.% undergoes L + α-Fe (A2) ↔ FeAl (B2) type reaction at 1310 °C. Although this transformation was considered as a peritectic reaction [127], it has been recently proposed and accepted to be a second order FeAl (B2) ↔ α-Fe (A2) transition [126].

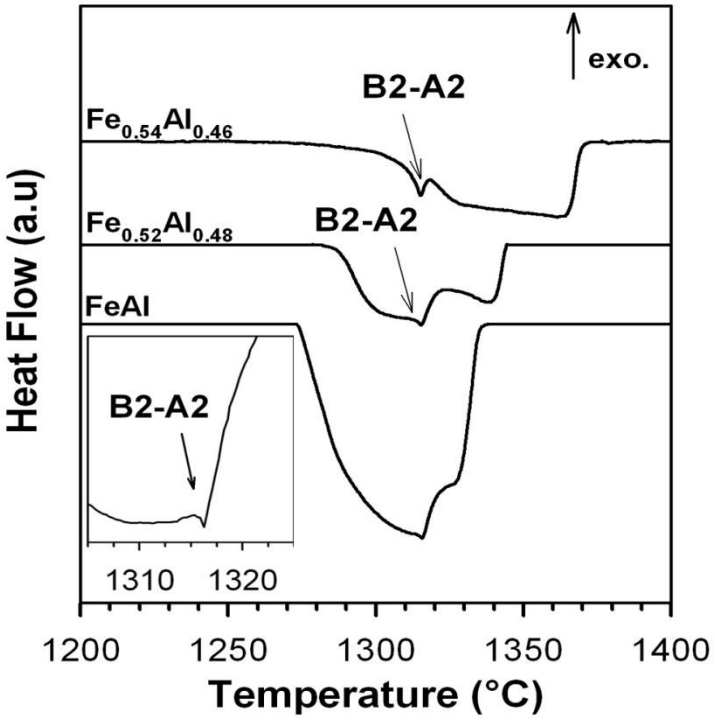

Figure 4.5 DSC heating (at a heating rate of 10K/min) curves of binary heat-treated Fe-Al alloys. Inset shows the 1305-1325 °C interval of binary FeAl alloy in detail.

Before going through a detailed analysis of the effect of ternary alloying additions on the order disorder transformation temperature of Fe-Al alloys, it is of interest to confirm the reliability and reproducibility of thermal behavior of $Fe_{50}Al_{49}X_1$ alloys studied in this present investigation by thermal analysis. Therefore, experimentally determined thermal characteristics of binary heat-treated Fe-Al alloys in the composition range of 46-50 at.% Al having B2-structure have been verified by phase diagram [28] and other experimental data on B2↔A2 order-disorder phase transition temperatures given in the literature [126]. Figure 4.5 shows the DSC thermograms of the binary B2-type ordered Fe-Al alloys on heating around their melting

temperatures. Peak temperatures appearing in L + α-Fe (A2) two phase region after melting have been identified as B2↔A2 order-disorder phase transition temperatures. The characteristics of the DSC thermograms and values of order-disorder transition temperatures, measured as 1316 °C for stoichiometric FeAl alloy, are consistent with the phase diagram [28] and other literature data [126].

The effect of ternary alloying additions on the B2↔A2 order-disorder phase transformation temperatures of the heat-treated $Fe_{50}Al_{49}X_1$ alloys has been analyzed by considering their DSC heating curves (Figure 4.6) and measured transformation temperatures are given in Table 4.2. It is evident that all ternary alloying elements except Cr and Ti, tend to increase the order-disorder transformation temperature with respect to binary Fe-Al alloy. Ti is the only ternary alloying element that slightly decreases this temperature.

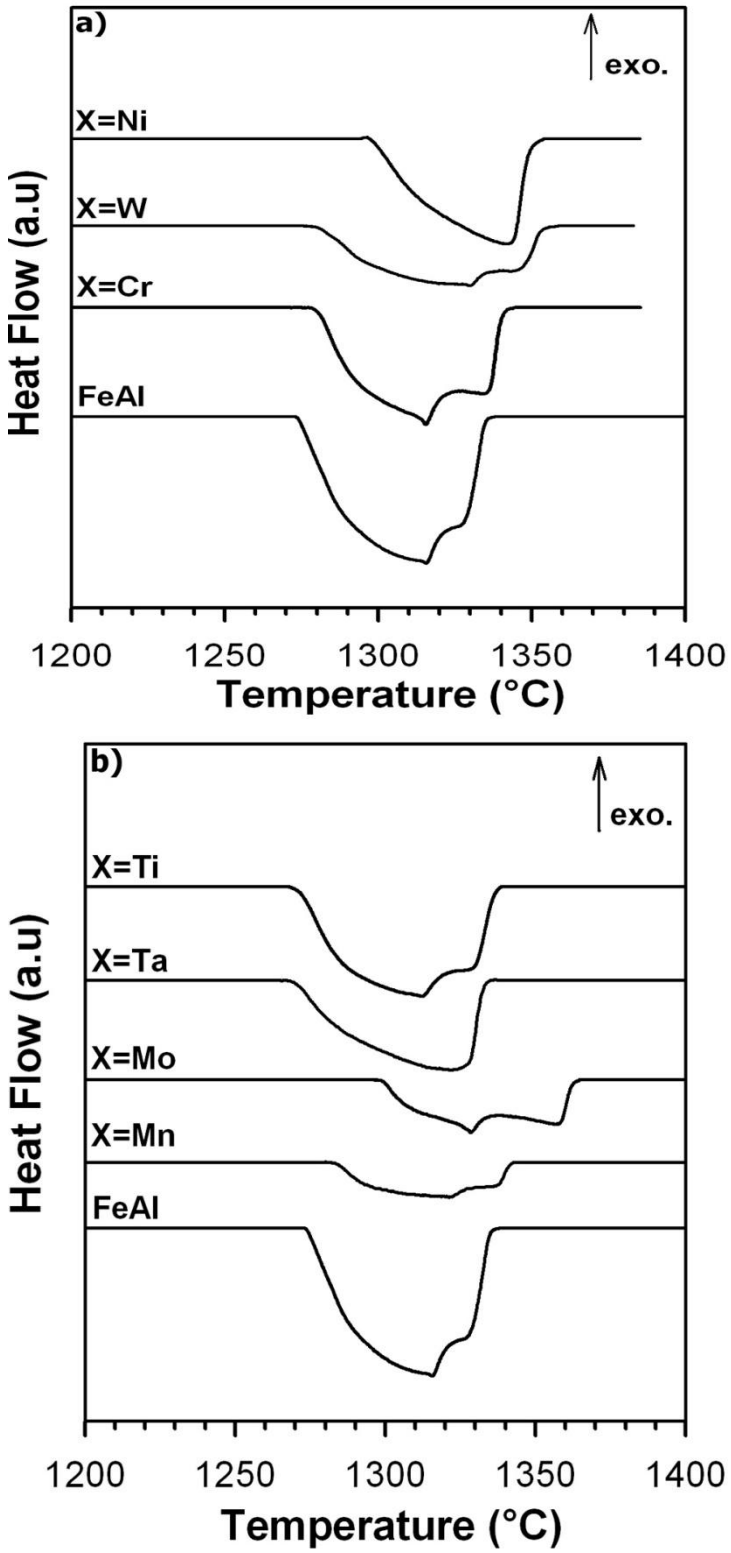

Figure 4.6 DSC heating (at a heating rate of 10K/min) curves of heat-treated $Fe_{50}Al_{50-n}X_n$ alloys; (a) X = Cr, W and Ni (b) X = Mn, Mo, Ta and Ti.

It appears that the extent of variation in B2↔A2 order-disorder phase transformation temperatures depends on the type of ternary alloying elements additions. The effect of type and content of the ternary alloying element additions on the order-disorder transformation temperatures of $Fe_{50}Al_{50-n}X_n$ intermetallics with B2-type ordered structure have also been investigated theoretically [16] by considering the energetic and structural characteristics of atomic ordering processes in these intermetallics. Hence, the effect of ternary alloying additions on the B2↔A2 order-disorder transformation temperature will now be discussed within the framework of the theoretical model and calculations proposed by Mekhrabov and Akdeniz [16] and comparison will be made with experimental results.

Table 4.2 Experimentally measured order-disorder transformation temperatures of heat-treated $Fe_{50}Al_{50-n}X_n$ alloys.

Alloying Element	None	Ti	Cr	Mn	Ni	Mo	Ta	W
B2↔A2 Order-Disorder Transition Temp. (°C)	1316	1313	1316	1322	1326	1330	1336	1336

It was shown that the distribution of ternary alloying element atoms over sublattices of B2-type Fe-Al intermetallics, determined by their partial SRO parameters, have a significant effect on the B2↔A2 order-disorder transformation temperature which has been calculated by using the following equation (4.4) [128];

$$\frac{\Delta T}{T_o} \approx 49\left[1-\frac{49}{48}\frac{1}{Cosh^{2}\left(\frac{W^{FeX}-W^{AlX}}{4k_BT_o}\right)}\right]c_X \qquad (4.4)$$

where $\Delta T = T_{ox} - T_o$ and it is the change in order-disorder phase transition temperature. T_o and T_{ox} denote the B2↔A2 order-disorder phase transition temperature of binary stoichiometric FeAl and Fe-Al-X intermetallics, respectively,

W_{FeX} and W_{AlX} are the partial ordering energies of Fe-X and Al-X pairs in the ternary alloy, respectively, k_B is the Boltzmann constant and c_X is the concentration of ternary alloying element X.

The normalized transition temperature, $\Delta T/T_o$, may be considered as an indication of degree of variation in order-disorder transition temperature that strongly depends on the type of ternary alloying X elements. Consequently, absolute values of relative partial ordering energies of different atomic pairs of Fe, Al, X elements, $W_{\alpha\alpha'}(R)$ in Fe-Al-X intermetallics become an important parameter in determining the T_{ox} temperatures. Employing the partial ordering energies of Fe-X and Al-X pairs in Table 4.3 (as given in Ref. [16]) and T_o of 1316 °C, as determined experimentally by DSC measurement for the binary FeAl alloy, the normalized transition temperatures are recalculated.

Table 4.3 Partial ordering energies of $Fe_{50}Al_{50-n}X_n$ alloys for n = 1 at.% at first coordination sphere.

Alloying Element	Ordering Energy (at. u.)		β
	$W^{AlX}(R_1)$	$W^{FeX}(R_1)$	$\frac{W^{AlX} - W^{FeX}}{W^{FeAl}}$
Ni	-3.67×10^{-3}	7.18×10^{-4}	-1.50
Mn	-4.84×10^{-3}	-7.37×10^{-4}	-1.41
Cr	-2.41×10^{-3}	4.00×10^{-4}	-0.96
Ti	3.09×10^{-3}	5.89×10^{-4}	0.86
Ta	2.54×10^{-2}	1.06×10^{-2}	5.07
Mo	4.44×10^{-2}	2.81×10^{-2}	5.58
W	4.18×10^{-2}	2.41×10^{-2}	6.06

The calculated values are compared to the experimentally determined normalized temperature changes for $Fe_{50}Al_{50-n}X_n$ alloys in Table 4.4. The qualitative and/or semi-quantitative agreement between theoretical predictions [16] and present experimental observation is excellent in terms of the effect of ternary alloying

elements addition on the tendency of variation of order-disorder phase transformation temperature of Fe-Al intermetallics.

Table 4.4 Normalized order-disorder transition temperatures of $Fe_{50}Al_{50-n}X_n$ alloys determined by DSC measurements in comparison with theoretical predictions [16] (T_o = 1316 °C for the binary FeAl alloy).

Alloying Element	$(\Delta T/T_o) \times 10^{-3}$			
	Theoretical			Experimental
	n = 0. 25 at.%	n = 0.5 at.%	n = 1 at.%	n = 1 at.%
Ti	-0.61	-1.26	-2.57	-1.88
Cr	-0.15	-0.31	-0.59	0
Mn	2.43	4.86	10.00	3.78
Ni	3.03	6.06	12.81	6.29
Mo	52.55	106.02	213.88	8.81
Ta	46.47	92.94	185.89	12.58
W	58.88	121.29	239.07	12.58

4.3 Relative Partial Ordering Energy Parameter (RPOE), β

It has been shown that the variation of critical order-disorder phase transformation temperature ΔT depends not only on the magnitude of partial ordering energies of Al-X and Fe-X atomic pairs, but also on the distribution of X ternary alloying element atoms over Fe and Al sublattices in Fe-Al intermetallics determined by their partial SRO parameters [16]. Hence, the tendency of variation of order-disorder phase transformation temperature may be determined exclusively by taking into account both the effects lattice site occupation preferences of X element atoms and magnitude of partial ordering energies. These energies would be considered as the measure of the bond strength of Al-X and Fe-X atomic pairs formed when X element atoms preferentially reside over either Fe or Al sublattices in Fe-Al intermetallics.

Thus, the relative partial ordering energy parameter (RPOE), β, has been defined by following equation (4.5);

$$\beta = \frac{W^{AlX} - W^{FeX}}{W^{FeAl}} \tag{4.5}$$

In the calculation of RPOE parameter we have used a value for the ordering energy of Fe-Al atomic pairs $W^{Fe\text{-}Al}(R_1) = 2.92x10^{-3}$ at.u. as determined by Krivoglaz and Smirnov [128]. Calculated values of RPOE parameters are tabulated in Table 4.3 together with the partial ordering energies of Al-X and Fe-X atomic pairs. It is worth to note that, while the sign of the RPOE parameter implies the distribution of ternary alloying element atoms over Fe and Al sublattices in Fe-Al intermetallics, its magnitude provides useful information on the bond strengths of atomic pairs of Al-X or Fe-X relative to Fe-Al in $Fe_{50}Al_{50-n}X_n$ intermetallics. The outcome of RPOE parameter and associated conditions for sublattice occupation, and the change in the order-disorder transformation temperatures are summarized in Table 4.5 along with experimentally and theoretically determined $\Delta T/T_o$ values.

Table 4.5 Order-disorder transition temperatures, relative partial ordering energy parameters, sublattice occupations and normalized order-disorder transition temperatures of $Fe_{50}Al_{50-n}X_n$ alloys.

Alloying Element	T_{ox} (°C)	β	$\Delta T = T_{ox}-T_o$ Condition		Occupation Site	Occupation Condition	$(\Delta T/T_o) \times 10^{-3}$ Exp.	$(\Delta T/T_o) \times 10^{-3}$ Theo
None	1316	-	-	-	-	-		
Cr	1316	-0.96	$T_{ox}\approx T_o$	β≈1	Al	β<0	0	-0.59
Mn	1322	-1.41	$T_{ox}>T_o$	β>1	Al	β<0	3.78	10.00
Ni	1326	-1.50	$T_{ox}>T_o$	β>1	Al	β<0	6.29	12.81
Ti	1313	0.86	$T_{ox}<T_o$	β<1	Fe	β>0	-1.88	-2.57
Mo	1330	5.58	$T_{ox}>>T_o$	β>>1	Fe	β>0	8.81	213.88
Ta	1336	5.07	$T_{ox}>>T_o$	β>>1	Fe	β>0	12.58	185.89
W	1336	6.06	$T_{ox}>>T_o$	β>>1	Fe	β>0	12.58	239.07

If RPOE parameter is negative ($\beta < 0$) ternary alloying element atoms (X_I = Ni, Mn or Cr) mainly occupy Al sublattice sites and they are surrounded by Fe atoms, whereas if RPOE parameter is positive ($\beta > 0$), X alloying element atoms (X_{II} = Ti, Ta, Mo or W) preferentially substitute Fe sublattice sites and are surrounded primarily by Al atoms. Current predictions based on the RPOE parameter is consistent with the theoretical predictions on Fe-Al intermetallics, in which lattice site occupancy preference of the impurity atoms is determined by their partial SRO parameters [16]. Furthermore, the change in critical order-disorder phase transformation temperature (ΔT) upon addition of X ternary alloying elements is related with the magnitude of RPOE parameter featuring the relative bond strength of Al-X and Fe-X atomic pairs with respect to Fe-Al atomic bond of binary Fe-Al alloy. When the relative bond strength of Al-X and Fe-X atomic pairs are close to the bond strength of Fe-Al atomic pair, RPOE parameter equals almost unity ($\beta \approx 1$). This would tend to suggest that no change in order-disorder transition temperature of $Fe_{50}Al_{50-n}X_n$ alloys is predicted compared to binary Fe-Al intermetallic as in the case of Cr addition. If RPOE parameter is less than unity ($\beta < 1$), relative bond strength of Al-X and Fe-X atomic pairs becomes weaker than that of the Fe-Al atomic pair, leading to a decrease in transformation temperature as in the case of Ti addition. Similarly, when alloying elements tend to form stronger Al-X and Fe-X atomic bonds than the Fe-Al atomic bond, RPOE parameter becomes greater than unity ($\beta > 1$), implying a slight increase in transformation temperature. However, alloying elements with very strong Al-X and Fe-X atomic bonds have RPOE parameter much greater than unity ($\beta >> 1$); thus, they would have a higher potential to increase the order-disorder transition temperature.

The present experimental observations on the effects of ternary alloying additions on the B2↔A2 order-disorder phase transformation temperatures of the $Fe_{50}Al_{49}X_1$ alloys are consistent qualitatively with the current predictions, based on the relative partial ordering energy parameter.

4.4 Conclusions

The effects of ternary alloying element additions on the variation of B2↔A2 order-disorder phase transformation temperatures of $Fe_{0.5}(Al_{1-n}X_n)_{0.5}$ intermetallics (n = 0.01) have been investigated experimentally by using various ternary alloying elements of X = Cr, Ni, Mo, Ta, Mn, Ti and W. The extent of variation order-disorder phase transformation temperatures has been defined by the normalized transition temperature ($\Delta T/T_o$) and it depends strongly on the type of ternary alloying element additions. Comparisons have been made with the theoretical model and calculations; consequently, predictions based on the variation of B2↔A2 order-disorder transition temperatures of $Fe_{0.5}(Al_{1-n}X_n)_{0.5}$ intermetallics have been verified experimentally. The tendency and measure of variation of order-disorder phase transformation temperature has been determined exclusively by defining relative partial ordering energy parameter (RPOE) which takes into account both the effects of lattice site occupation preferences of X element atoms and magnitude of partial ordering energies of Al-X and Fe-X atomic pairs relative to Fe-Al pairs. The sign of the RPOE parameter implies the distribution of ternary alloying element atoms over Fe and Al sublattices in B2-type ordered Fe-Al intermetallics and its magnitude provides an indication of the variation of order-disorder transformation temperature relative to binary FeAl alloys. Related outcomes of the study can be summarized as follows;

i. Since their RPOE parameter is negative ($\beta < 0$), alloying elements of X_I = Ni, Mn or Cr mainly prefer Al sublattice sites and they are surrounded by Fe atoms in FeAl superlattice.
ii. Since their RPOE parameter is positive ($\beta > 0$), alloying elements of X_{II} = Ti, Ta, Mo, or W prefer Fe sublattice sites and they are surrounded mainly by Al atoms in FeAl superlattice.
iii. Depending on the magnitude of the RPOE parameter, change of the B2↔A2 order-disorder transformation temperature in presence of a ternary alloying element X can be predicted as follows;
    - $\beta \approx 1$ indicates no change; thus, $T_{ox} \approx T_o$ (X = Cr)

- $\beta < 1$ indicates a small decrease; thus, $T_{ox} < T_o$ (X = Ti)
- $\beta > 1$ indicates a slight increase; thus, $T_{ox} > T_o$ (X = Mn, Ni)
- $\beta >> 1$ indicates a significant increase; thus, $T_{ox} >> T_o$ (X = Mo, Ta, W)

CHAPTER 5

EFFECT OF TERNARY ALLOYING ADDITIONS ON STRUCTURAL PROPERTIES AND ROOM TEMPERATURE MECHANICAL PROPERTIES OF $Fe_{50}Al_{50-n}X_n$ ALLOYS

5.1 Cr, Mn and Mo additions

Room temperature brittleness problem of FeAl based intermetallic compounds greatly hinders their applications as a structural material. In this particular aspect, great research effort has been performed and is still being performed to improve the room temperature ductility of this type of materials. Among them proper thermal treatments and additions of ternary alloying elements seem to be most proper ways.

Previous studies showed that ternary alloying elements having complete solid solubility in Fe-Al based alloys such as Cr, Mn, Ni, Li, Co, Si, Cu or Zn have a significant influence on increasing room temperature ductility [45]. Among these alloying elements, Cr and Mn seem to be the most effective ones that can improve room temperature ductility. However, there is still little information about Cr and Mn addition on room temperature mechanical properties of Fe-Al based alloys since the relevant literature data contains certain amount of Cr or Mn [46, 47, 54-58]. Therefore, in this study, it is of research interest to investigate the effect of Cr and Mn content on microstructures and room temperature mechanical properties of FeAl intermetallic compound in detail upon solidification and subsequent heat-treatment. Additionally, Mo is also considered as a ternary alloying element in order to make a comparison between the effect of solid solution forming elements and second phase forming elements.

5.1.1 Microstructure and Phase Analysis

Table 5.1 lists the nominal and actual compositions of suction casted and heat-treated $Fe_{50}Al_{50-n}X_n$ alloys with additions of Cr, Mn and Mo for n= 1, 3, 5, 7 and 9 at.%. Compositions of all investigated alloys except for heat-treated $Fe_{50}Al_{43}Mo_7$ and $Fe_{50}Al_{41}Mo_9$ alloys have very good agreement with their nominal compositions. The microstructures of all as-cast and heat-treated $Fe_{50}Al_{50-n}Cr_n$ and $Fe_{50}Al_{50-n}Mn_n$ alloys (Figure 5.1 and 5.2) exhibit single phase solid solutions having equiaxed coarse grains due to the large solid solubility of Cr and Mn in FeAl phase [11, 45].

Table 5.1 Nominal and actual compositions of $Fe_{50}Al_{50-n}X_n$ samples.

Nominal composition (at.%)	EDS analysis (at.%)					
	as-cast			heat-treated		
	Fe	Al	X	Fe	Al	X
Fe-50Al	50.2 ± 0.1	49.8 ± 0.1	-	50.4 ± 0.2	49.6 ± 0.2	-
Fe-49Al-1Cr	50.2 ± 0.1	48.8 ± 0.2	1.0 ± 0.1	50.1 ± 0.2	48.8 ± 0.2	1.1 ± 0.1
Fe-47Al-3Cr	49.6 ± 0.2	47.1 ± 0.2	3.3 ± 0.2	50.2 ± 0.3	46.7 ± 0.2	3.1 ± 0.2
Fe-45Al-5Cr	49.7 ± 0.1	44.7 ±0.3	5.6 ± 0.4	50.2 ± 0.3	44.6 ± 0.4	5.2 ± 0.2
Fe-43Al-7Cr	51.0 ± 0.4	42.6 ± 0.3	6.4 ± 0.8	51.3 ± 0.3	42.1 ± 0.3	6.6 ± 0.5
Fe-41Al-9Cr	49.1 ± 0.2	41.6 ± 0.3	9.3 ± 0.5	50.5 ± 0.2	39.9 ± 0.9	9.6 ± 0.8
Fe-49Al-1Mo	50.2 ± 0.1	48.8 ± 0.2	1.2 ± 0.3	50.5 ± 0.3	48.4 ± 0.3	1.1 ± 0.2
Fe-47Al-3Mo	49.5 ± 0.3	47.4 ± 0.3	3.1 ± 0.4	49.0 ± 0.4	47.7 ± 0.6	3.3 ± 0.4
Fe-45Al-5Mo	49.2 ± 0.5	45.0 ± 0.3	5.8 ± 0.9	49.4 ± 0.2	45.0 ± 0.5	5.6 ± 0.9
Fe-43Al-7Mo	51.9 ± 0.8	40.9 ± 0.9	7.2 ± 0.9	59.2 ± 0.9	34.9 ± 1.4	5.9 ± 1.0
Fe-41Al-9Mo	50.8 ± 0.6	40.6 ± 1.0	8.6 ± 1.2	59.4 ± 1.1	34.1 ± 1.3	6.5 ± 1.4
Fe-49Al-1Mn	50.1 ± 0.1	49.1 ± 0.1	0.8 ± 0.2	50.1 ± 0.2	48.8 ± 0.2	1.1 ± 0.2
Fe-47Al-3Mn	49.5 ± 0.2	46.8 ± 0.2	3.7 ± 0.3	50.0 ± 0.2	46.4 ± 0.3	3.6 ± 0.2
Fe-45Al-5Mn	50.6 ± 0.3	44.2 ± 0.2	5.2 ± 0.5	50.5 ± 0.2	44.4 ± 0.2	5.1 ± 0.2
Fe-43Al-7Mn	50.6 ± 0.3	42.1 ± 0.2	7.3 ± 0.3	50.5 ± 0.2	42.4 ± 0.2	7.1 ± 0.2
Fe-41Al-9Mn	49.9 ± 0.3	40.8 ± 0.3	9.1 ± 0.4	50.4 ± 0.2	40.8 ± 0.2	8.8 ± 0.2

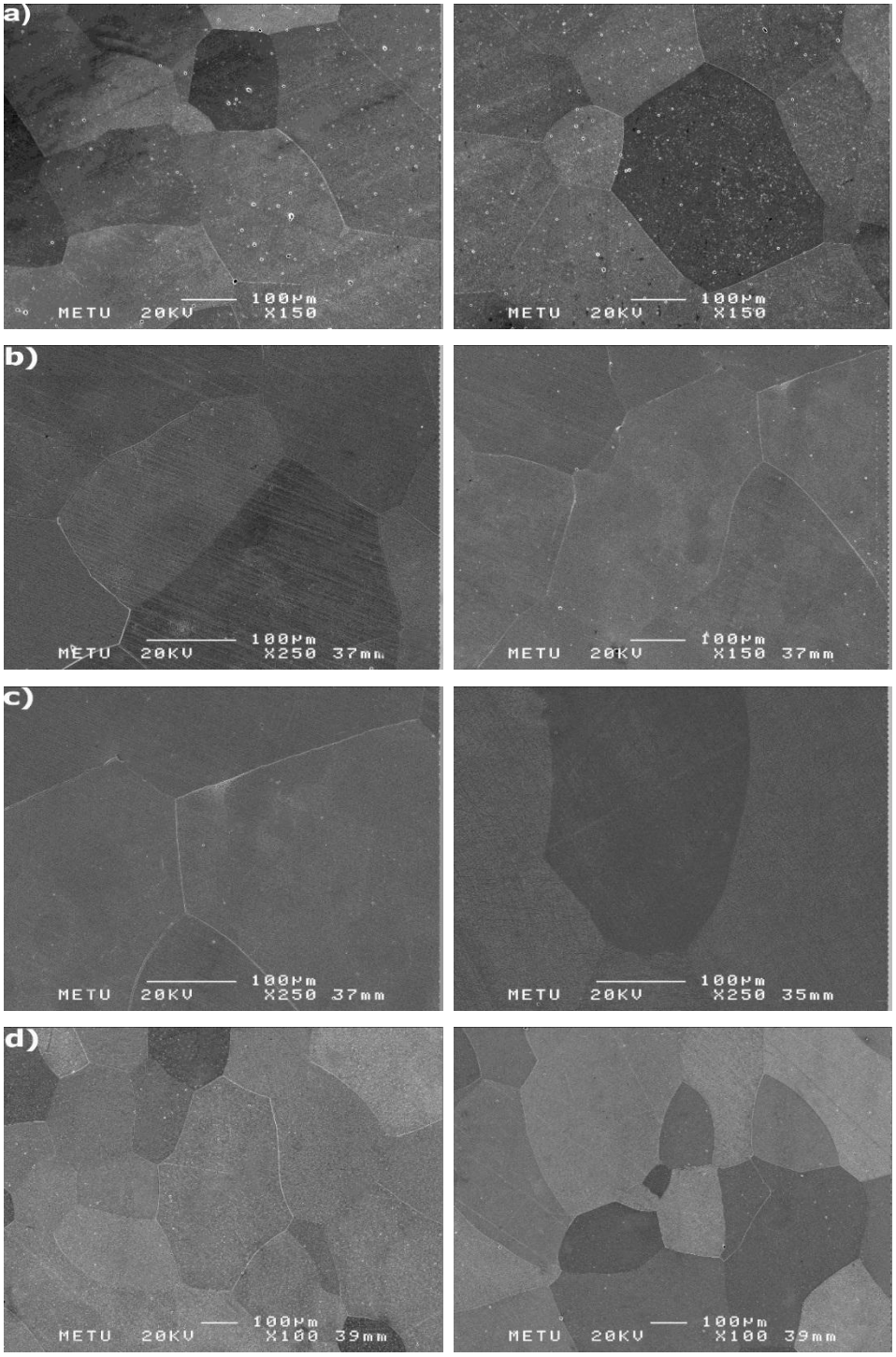

Figure 5.1 SEM micrographs of as-cast and heat-treated (right-side) $Fe_{50}Al_{50-n}Cr_n$ alloys; n= (a) 0, (b) 1, (c) 3, (d) 5, (e) 7 and (f) 9.

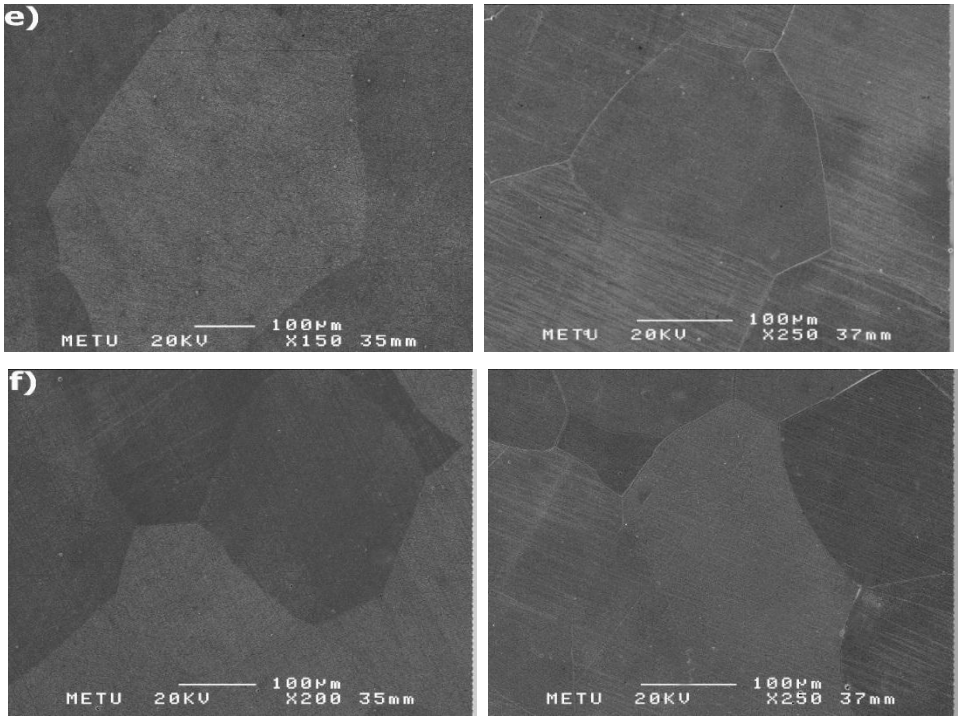

Figure 5.1 (cont'd) SEM micrographs of as-cast and heat-treated (right-side) $Fe_{50}Al_{50-n}Cr_n$ alloys; n= (a) 0, (b) 1, (c) 3, (d) 5, (e) 7 and (f) 9.

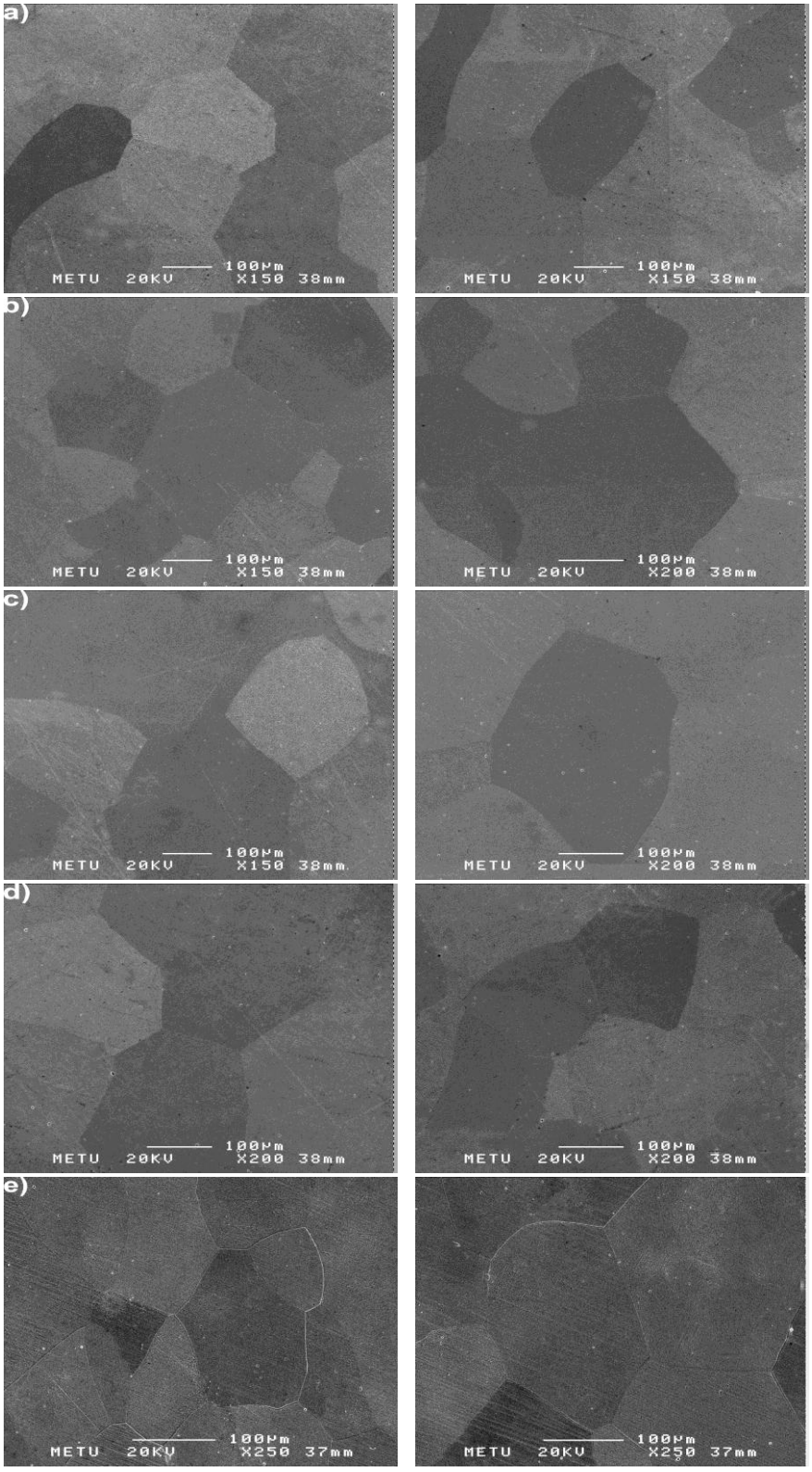

Figure 5.2 SEM micrographs of as-cast and heat-treated (right-side) $Fe_{50}Al_{50-n}Mn_n$ alloys; n= (a) 1, (b) 3, (c) 5, (d) 7 and (e) 9

Furthermore, XRD analyses of as-cast and heat-treated $Fe_{50}Al_{50-n}Cr_n$ and $Fe_{50}Al_{50-n}Mn_n$ alloys reveal almost the same diffraction pattern as that of the stoichiometric B2-type ordered FeAl intermetallic compound and confirm the presence of single phase (Figures 5.3 and 5.4). The relative intensities of diffraction lines are comparatively larger for the heat-treated than as-cast alloys due to the homogenization and ordering heat-treatment described above.

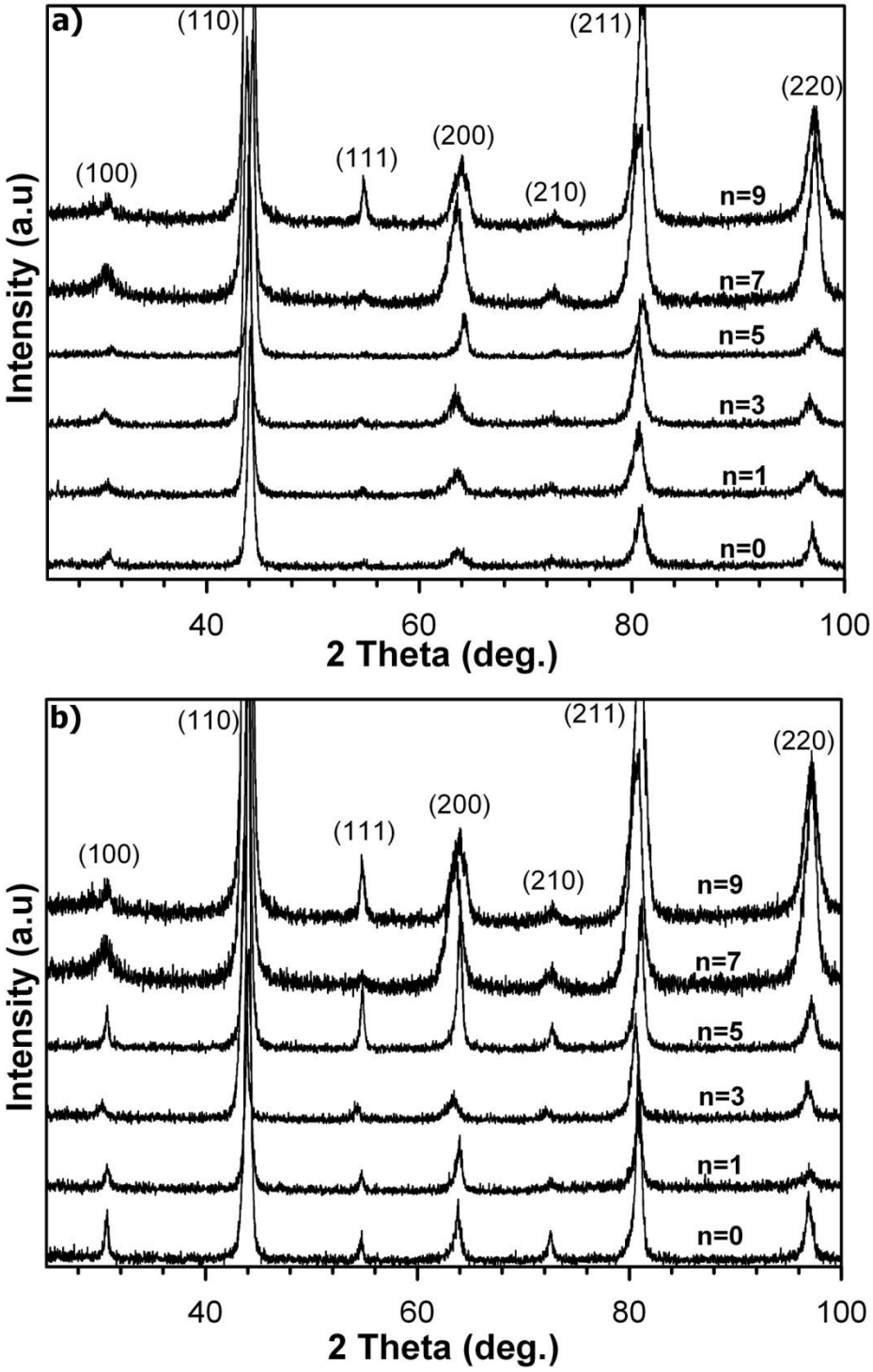

Figure 5.3 XRD patterns of $Fe_{50}Al_{50-n}Cr_n$ alloys (a) as-cast and (b) heat-treated.

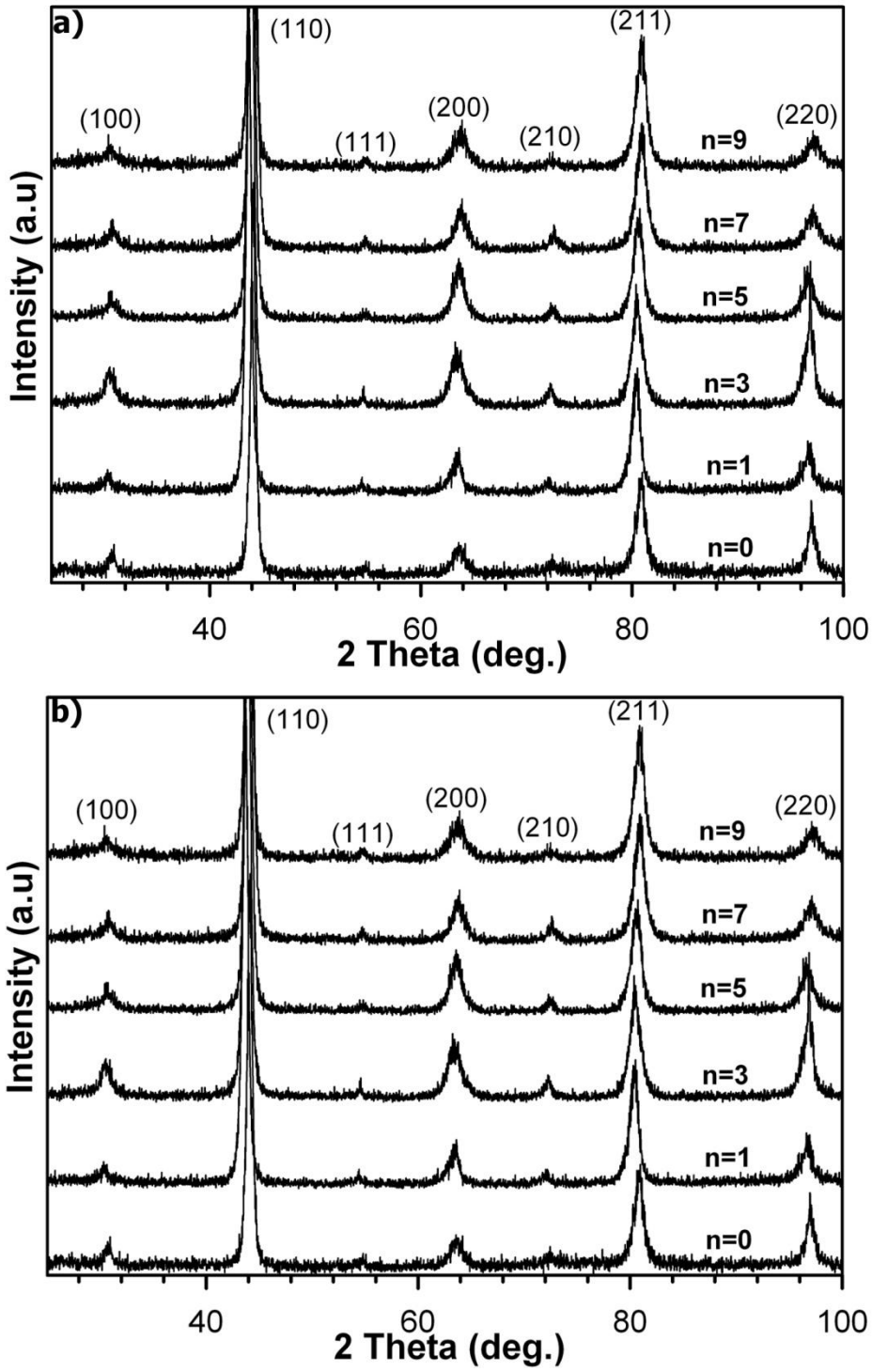

Figure 5.4 XRD patterns of $Fe_{50}Al_{50-n}Mn_n$ alloys (a) as-cast and (b) heat-treated.

However, second phase particles exist in the microstructures of all as-cast and heat-treated $Fe_{50}Al_{50-n}Mo_n$ alloys (Figure 5.5). The formation of these particles is directly attributed to limited solid solubility of Mo in FeAl intermetallic compound. Based on XRD (Figure 5.6) and EDS (Figure 5.7 and Table 5.2) analyses, these second phase particles can be identified as binary Mo_3Al (space group 223, Pm n) precipitates. The volume fraction of Mo_3Al particles increase with increasing Mo content.

However, Mo_3Al precipitates are only present at grain boundaries in as-cast alloys, while heat-treatment results in the precipitation of these particles also within the grains for higher Mo contents (n>3). Investigated compositions of $Fe_{50}Al_{50-n}Mo_n$ alloys lie near/within the (B2+ Mo_3Al) two phase region according to the isothermal section of Fe-Al-Mo ternary phase diagram at 1000 °C [129]. Plentiful Mo_3Al precipitation after heat-treatment is directly related to the solid solubility behaviour of Mo in Fe-Al phase in equilibrium with Mo_3Al. Heat-treatment results in extra nucleation of Mo_3Al particles and growth existing particles for supersaturated as-cast alloys. Moreover, the solubility of Mo in B2 type ordered FeAl phase in equilibrium with Mo_3Al decreases with decreasing temperature during cooling [129]. Hence, amount of Mo_3Al precipitates increase substantially with heat-treatment followed by furnace cooling.

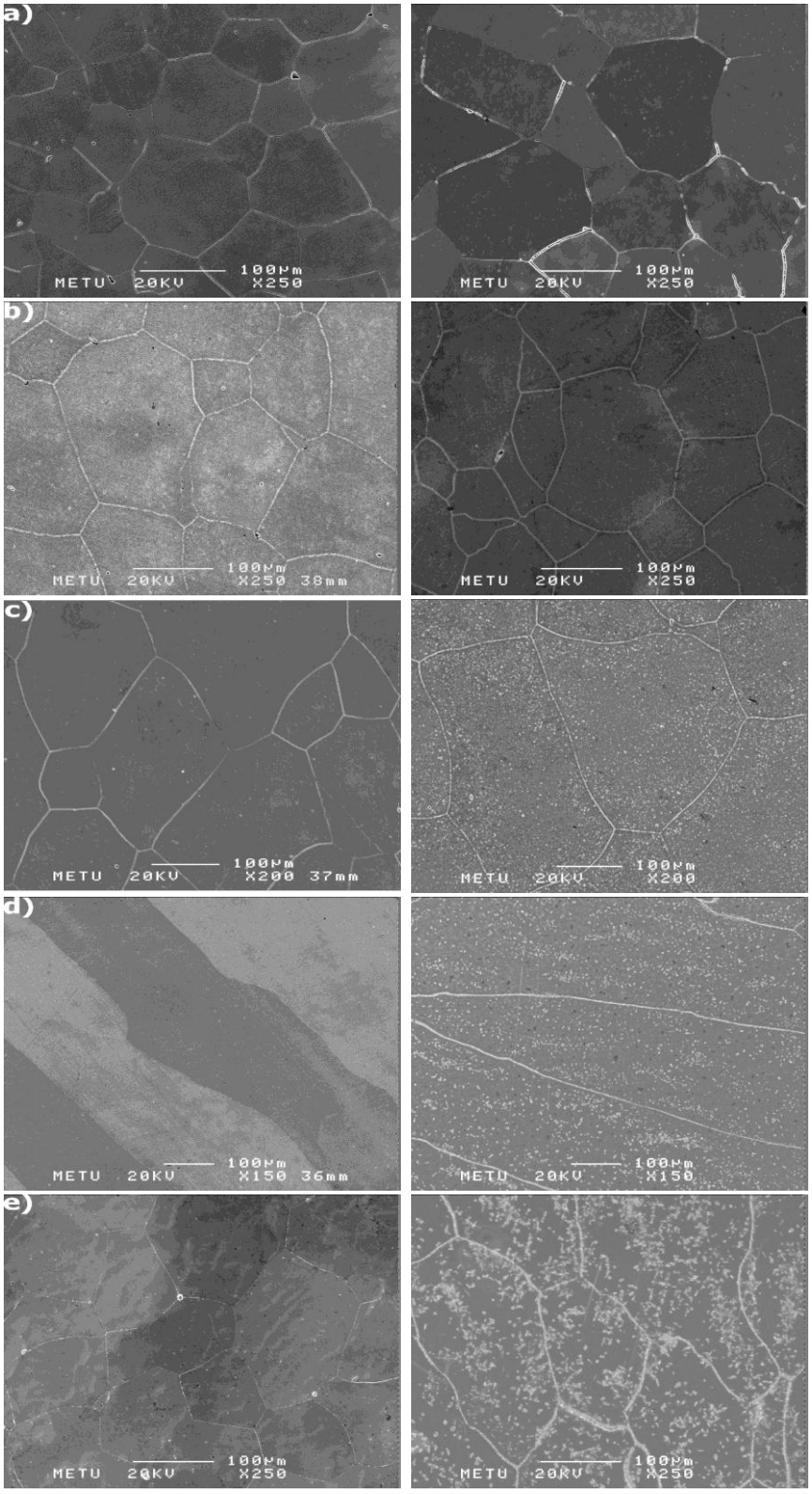

Figure 5.5 SEM micrographs of as-cast and heat-treated (right-side) $Fe_{50}Al_{50-n}Mo_n$ alloys; n= (a) 1, (b) 3, (c) 5, (d) 7 and (e) 9.

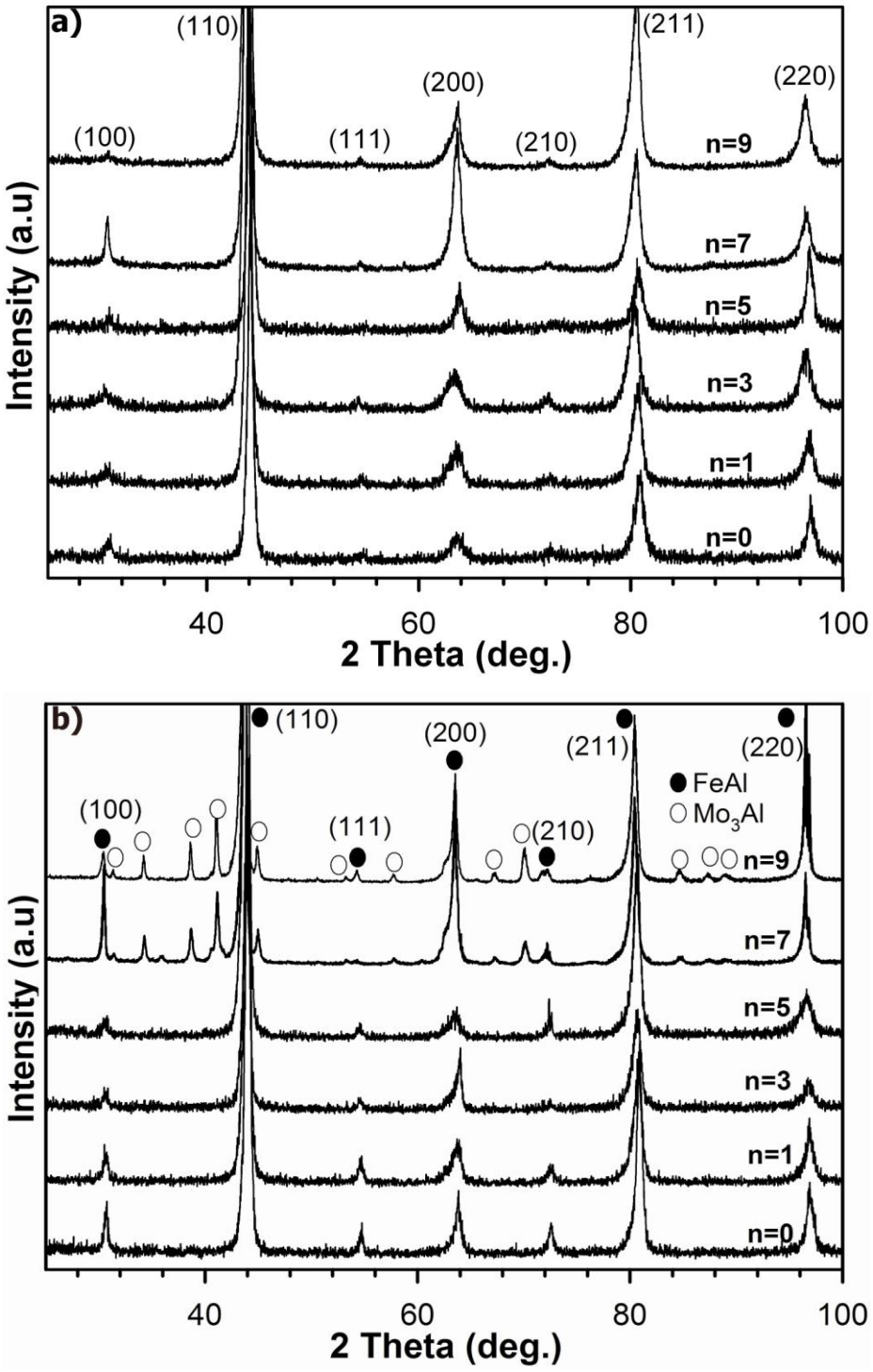

Figure 5.6 XRD patterns of $Fe_{50}Al_{50-n}Mo_n$ alloys (a) as-cast and (b) heat-treated.

High magnification FESEM (Figure 5.7) analyses were performed in order to investigate the morphology, size, distribution and volume fraction of Mo_3Al precipitates for $Fe_{50}Al_{43}Mo_7$ and $Fe_{50}Al_{41}Mo_9$ alloys. The volume fraction and size of the Mo_3Al precipitates are summarized in Table 5.3. the volume fractions are in very good agreement with the expected amounts of Mo_3Al precipitates [84]. Mo_3Al precipitates do not have any specific morphology and they are uniformly distributed along grain boundaries and grain interior without forming any precipitate free zones.

Table 5.2 Results of EDS analysis of Mo_3Al precipitates.

EDS analysis (at.%)		
Mo	Al	Fe
74.9 ± 1.1	20.7 ± 0.4	4.3 ± 0.4

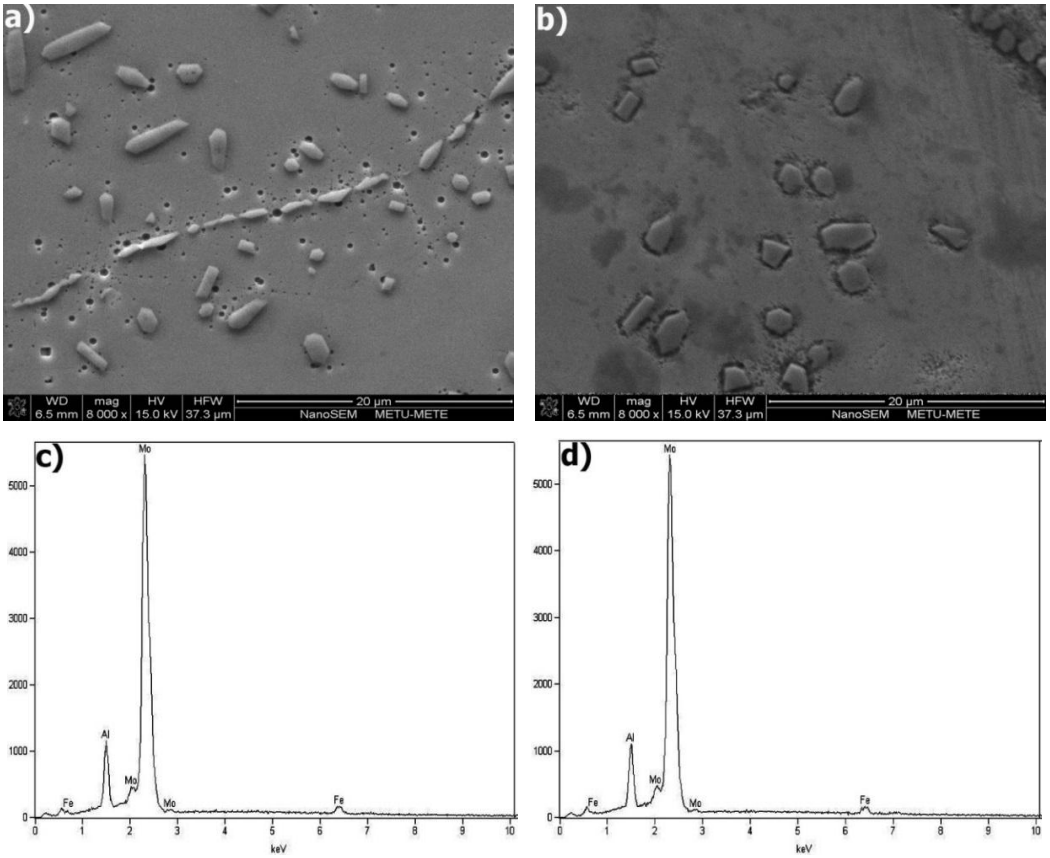

Figure 5.7 FESEM micrographs and EDS analysis of heat-treated $Fe_{50}Al_{50-n}Mo_n$ alloys; (a), (c) n = 7 and, (b), (d) n = 9.

Table 5.3 Size and volume fraction of the Mo_3Al precipitates for heat-treated $Fe_{50}Al_{43}Mo_7$ and $Fe_{50}Al_{41}Mo_9$ alloys.

at.% Mo	7	9
precipitate size (grain interior), μm	2.1 ± 0.2	2.7 ± 0.1
precipitate size (grain boundary), μm	3.8 ± 0.8	4.3 ± 0.7
vol.% of precipitate	2.21	5.76

5.1.2 Determination of B2↔A2 Order-Disorder Phase Transition Temperatures

Additionally, DSC measurements were performed in order to investigate the effect of Cr, Mn and Mo additions on B2↔A2 order-disorder phase transition temperatures of B2-type ordered FeAl intermetallic compound. DSC heating curves of heat-treated $Fe_{50}Al_{50-n}X_n$ alloys are presented in Figure 5.8 and measured order-disorder transition, solidus and liquidus temperatures are listed in Table 5.4. It is important to note that the extent of variation in order-disorder transition temperatures depend on the type of ternary alloying addition and its solid solubility behaviour in B2 type Fe-Al based phase.

In the Section 4.1.2, it was shown that the effect of ternary alloying additions at small amounts ($n \leq 1$) is directly related to the site occupancy character of X element in B2 type superlattice and relative bond strength of Fe-X and Al-X pairs. However, variation in transition temperatures for ternary alloying additions at amounts higher than 1 at.% is associated to the solid solubility behaviour of X in Fe-Al based phase and phase relationships. Although all Cr, Mn and Mo additions higher than 1 at.% decrease the B2↔A2 order-disorder phase transition temperatures, the tendency of decrease for Mo additions are strongly higher than those for Cr and Mn additions.

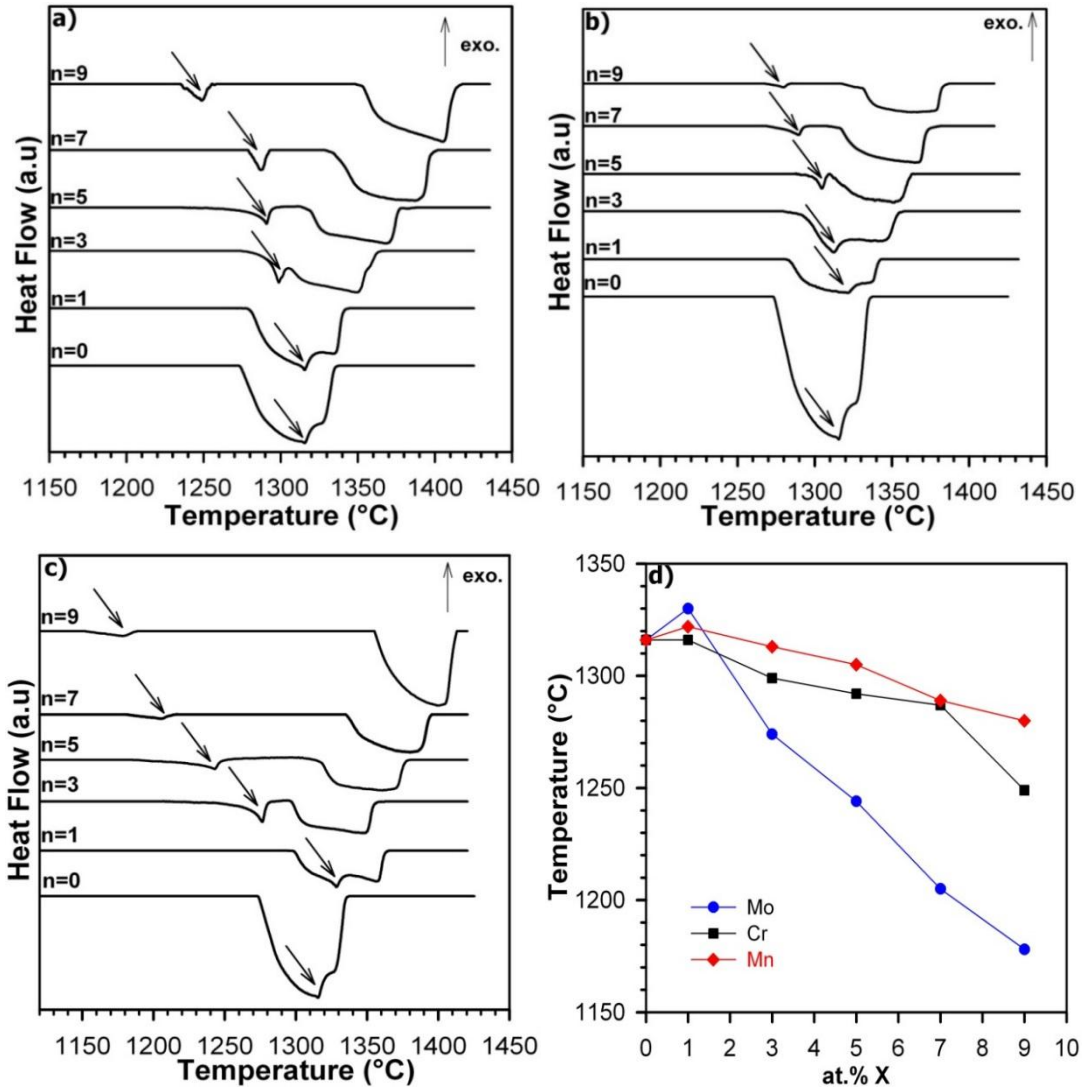

Figure 5.8 DSC heating (at a heating rate of 10K/min) curves of heat-treated $Fe_{50}Al_{50-n}X_n$ alloys, X= (a) Cr, (b) Mn, (c) Mo and (d) order-disorder transition temperature versus amount of alloying addition curves.

Table 5.4 Experimentally measured order-disorder transition, solidus and liquidus temperatures of heat-treated $Fe_{50}Al_{50-n}X_n$ alloys.

Alloy	$T_{B2\leftrightarrow A2}$ (°C)	$T_{sol.}$ (°C)	$T_{liq.}$ (°C)
FeAl	1316	1270	1325
Fe-49Al-1Mo	1330	1277	1334
Fe-47Al-3Mo	1274	1298	1347
Fe-45Al-5Mo	1244	1317	1365
Fe-43Al-7Mo	1205	1338	1398
Fe-41Al-9Mo	1178	1346	1408
Fe-49Al-1Cr	1316	1283	1333
Fe-47Al-3Cr	1299	1307	1357
Fe-45Al-5Cr	1292	1317	1370
Fe-43Al-7Cr	1287	1339	1380
Fe-41Al-9Cr	1249	1353	1394
Fe-49Al-1Mn	1322	1283	1337
Fe-47Al-3Mn	1313	1293	1346
Fe-45Al-5Mn	1305	1309	1354
Fe-43Al-7Mn	1289	1317	1362
Fe-41Al-9Mn	1280	1331	1374

The Al composition in the Fe-Al based matrix phase is very close to the its nominal composition in the presence of ternary alloying elements that readily form a single phase solid solution such as Cr and Mn due to their extended solid solubility in Fe-Al phase. On the other hand, the Al composition in the Fe-Al based matrix phase is importantly lower than its nominal composition in the case of ternary alloying additions form second phase particles such as Mo due to their limited solid solubility in Fe-Al phase (Table 5.1). According to the binary Fe-Al phase diagram [28], B2↔A2 order-disorder phase transition temperature decrease approaching to $D0_3$ side, whereas melting temperature increase with decreasing Al content. Therefore, much more reduction is observed in transition temperature for Mo additions rather

than Cr or Mn additions. Mo_3Al precipitation for heat-treated $Fe_{50}Al_{43}Mo_7$ and $Fe_{50}Al_{41}Mo_9$ alloys decreased the Al amount in the matrix phase that results in a sharp reduction of transition temperature. As a summary, Al content in the matrix phase is the dominant factor which affects the order-disorder transition temperature.

5.1.3 Room Temperature Mechanical Properties

Before going through a detailed analysis of the effect of Cr, Mn and Mo additions on the room temperature mechanical properties and deformation mechanism of FeAl intermetallic compound, uniaxial compression tests for as-cast and heat-treated binary FeAl intermetallic compound (Figure 5.9) have been performed and measured parameters have been compared with other data on mechanical properties of Fe-Al alloys given in the literature. Compared to as-cast alloy, heat-treated FeAl exhibits considerably improved plasticity with reduced yield stress. Moreover, fracture mode changed from intergranular decohesion to transgranular cleavage (Figure 5.10).

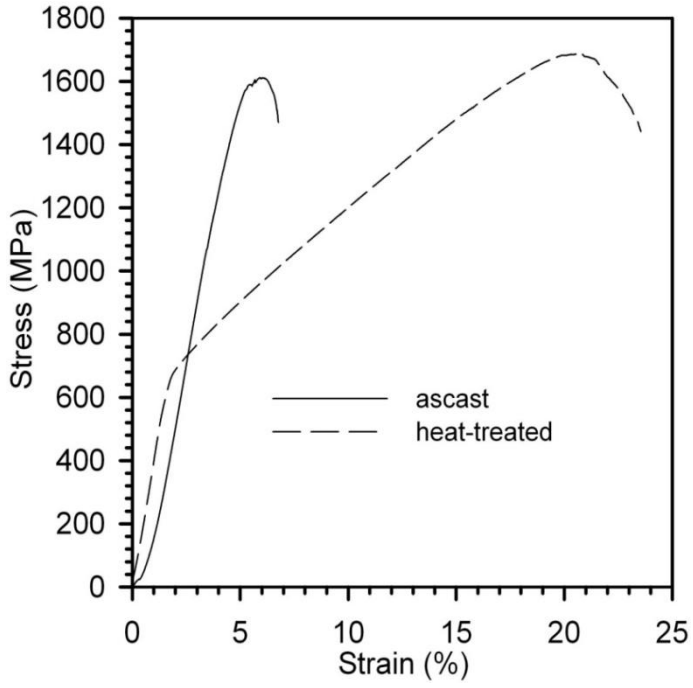

Figure 5.9 Room temperature stress-strain compression curves of binary FeAl intermetallic.

Nagpal and Baker [42] proposed that ductility of Fe-Al decrease with increasing Al content and stoichiometric FeAl alloy is extremely brittle with displaying no tensile ductility. They also showed that the fracture mode of FeAl is intergranular. In addition, yield stresses more than 1000 MPa in Al rich Fe-Al alloys have been observed in several studies [35-37]. Extremely brittle nature of B2-type FeAl with respect to other Fe-Al alloys is directly attributed to the thermal vacancy concentrations. It is well known that vacancy concentration increases with Al content and becomes maximum around Fe-50Al stoichiometric composition [38, 39]. Vacancy concentration is significantly reduced after long heat-treatment and finally FeAl shows substantial ductility at room temperature.

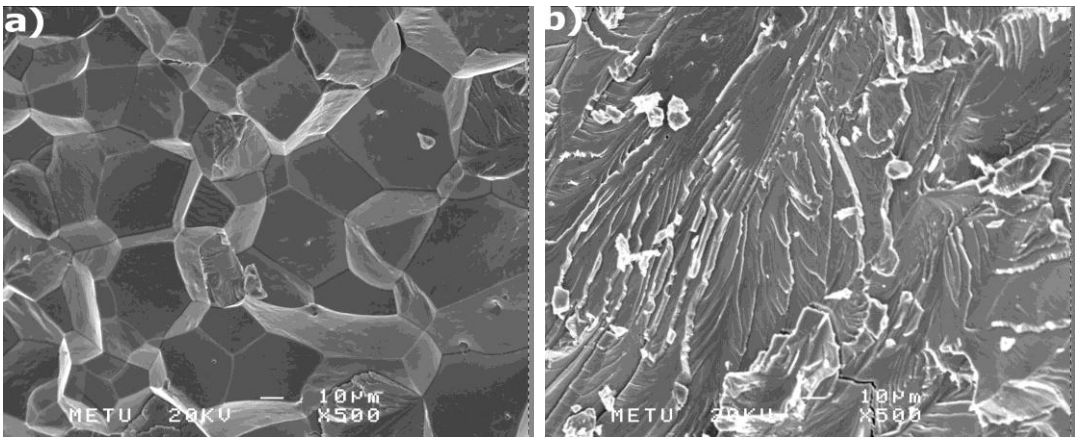

Figure 5.10 Fracture surfaces of binary FeAl intermetallic after compressive testing at room temperature (a) as-cast and (b) heat-treated.

However, it is of research interest to further increase the room temperature ductility by means of ternary alloying additions. Room temperature compressive stress-strain curves for $Fe_{50}Al_{50-n}X_n$ alloys are given in Figures 5.11, 5.12 and 5.13 for X=Cr, Mn and Mo, respectively and measured yield stress (σ_y), ultimate compressive stress (σ_{max}), yield strain (ε_y) and plastic strain (ε_p) values are listed in Table 5.5.

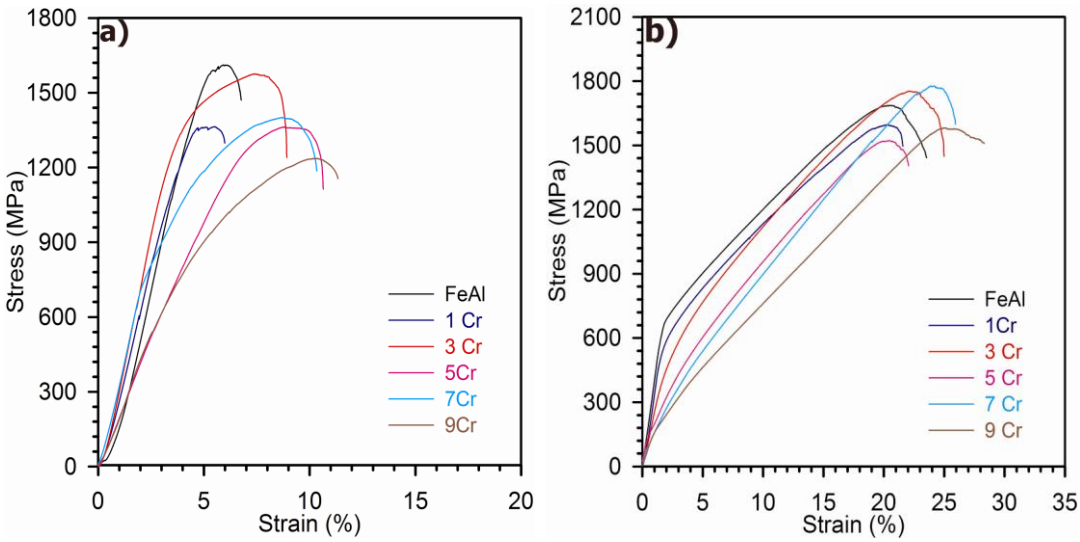

Figure 5.11 Room temperature stress-strain compression curves of $Fe_{50}Al_{50-n}Cr_n$ alloy (a) as-cast and (b) heat-treated.

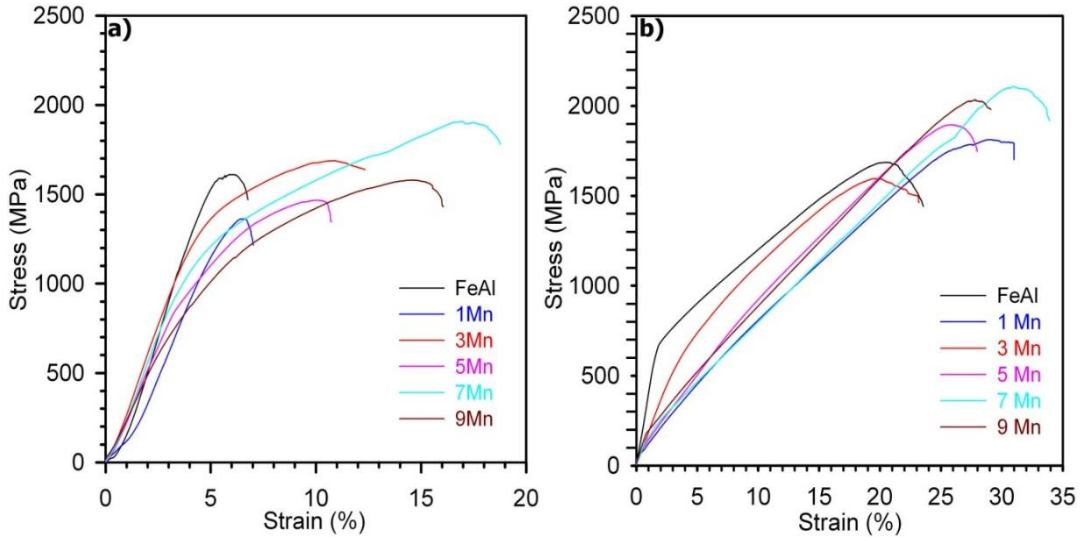

Figure 5.12 Room temperature stress-strain compression curves of $Fe_{50}Al_{50-n}Mn_n$ alloys (a) as-cast and (b) heat-treated.

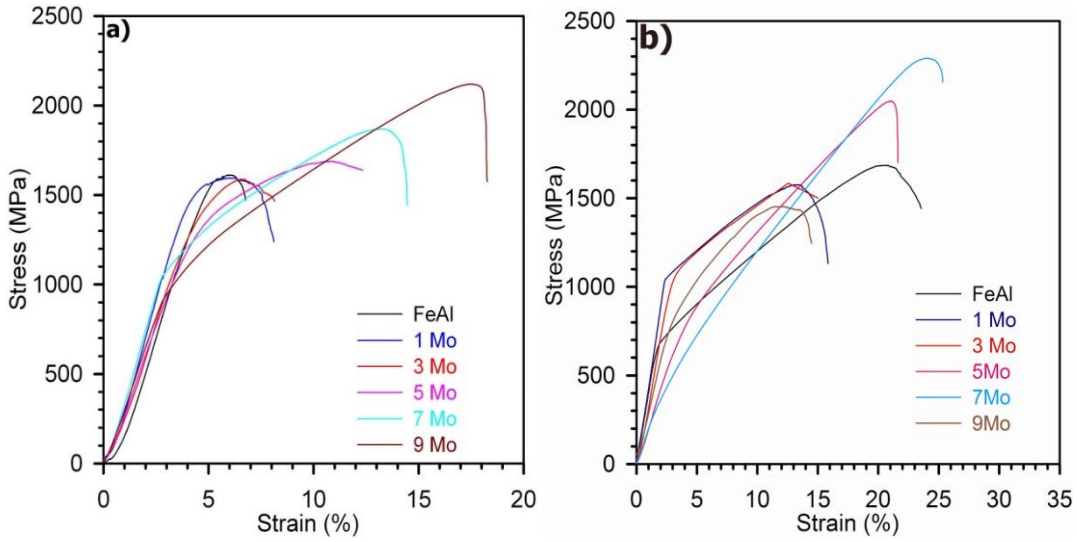

Figure 5.13 Room temperature stress-strain compression curves of $Fe_{50}Al_{50-n}Mo_n$ alloys (a) as-cast and (b) heat-treated.

Based on these findings, all investigated as-cast alloys exhibit softening of Fe-Al matrix compared to stoichiometric FeAl intermetallic compound. The yield stress decreases and plastic strain increases with increasing alloying addition content except for $Fe_{50}Al_{41}Mn_9$ alloy. There is a good correlation between softening effect and Al content for Fe-Al based alloys. The yield stress reduces noticeably with only small deviations from stoichiometric composition and certain amount of plasticity can be observed before failure [35, 130]. Although all as-cast ternary alloys possess lower yield stress values than binary FeAl, $Fe_{50}Al_{50-n}Mo_n$ alloys display larger hardening effects during plastic deformation in comparison to $Fe_{50}Al_{50-n}Cr_n$ and $Fe_{50}Al_{50-n}Mn_n$ alloys due to Mo_3Al precipitation at grain boundaries.

Table 5.5 Mechanical properties for the as-cast and heat-treated $Fe_{50}Al_{50-n}X_n$ alloys: yield stress σ_y (0.2% offset), ultimate compressive stress σ_{max}, strain at the yield point ε_y and plastic strain ε_p.

Alloy	As-cast				Heat-treated			
	σ_y (MPa)	σ_{max} (MPa)	ε_y (%)	ε_p (%)	σ_y (MPa)	σ_{max} (MPa)	ε_y (%)	ε_p (%)
FeAl	1449 ± 92	1657 ± 69	4.4 ± 0.4	2.4 ± 0.3	673 ± 55	1687 ± 46	1.9 ± 0.1	21.7 ± 0.6
1Cr	1199 ± 73	1415 ± 87	3.5 ± 0.3	2.5 ± 0.3	575 ± 43	1588 ± 54	2.1 ± 0.1	19.4 ± 0.4
3Cr	1149 ± 69	1565 ± 99	3.4 ± 0.4	5.6 ± 0.6	481 ± 24	1821 ± 71	2.3 ± 0.2	22.7 ± 0.5
5Cr	820 ± 78	1353 ± 77	4.2 ± 0.6	6.4 ± 0.6	427 ± 39	1500 ± 67	3.2 ± 0.2	18.9 ± 0.3
7Cr	754 ± 65	1407 ± 90	2.6 ± 0.3	7.8 ± 0.8	388 ± 36	1731 ± 78	3.4 ± 0.3	21.6 ± 0.4
9Cr	627 ± 71	1255 ± 78	2.6 ± 0.4	8.7 ± 0.7	365 ± 33	1971 ± 75	3.0 ± 0.1	25.3 ± 0.3
1Mn	1202 ± 87	1363 ± 87	5.3 ± 0.8	1.8 ± 0.1	657 ± 56	1812 ± 65	7.8 ± 0.4	23.6 ± 0.4
3Mn	1158 ± 76	1706 ± 101	3.9 ± 0.4	8.5 ± 0.4	637 ± 23	1708 ± 54	3.5 ± 0.1	19.7 ± 0.3
5Mn	1003 ± 54	1530 ± 98	5.0 ± 0.5	5.7 ± 0.2	482 ± 25	1837 ± 38	2.7 ± 0.1	25.3 ± 0.4
7Mn	989 ± 61	1917 ± 107	3.6 ± 0.4	15.2 ± 1.5	255 ± 18	2008 ± 71	1.6 ± 0.1	32.3 ± 0.5
9Mn	913 ± 65	1675 ± 99	4.2 ± 0.3	11.9 ± 0.9	233 ± 21	2100 ± 69	1.0 ± 0.1	27.3 ± 0.4
1Mo	1297 ± 97	1581 ± 95	3.7 ± 0.3	4.5 ± 0.4	949 ± 87	1492 ± 46	2.6 ± 0.2	13.3 ± 0.3
3Mo	1255 ± 89	1606 ± 101	4.8 ± 0.6	3.3 ± 0.3	1019 ± 85	1583 ± 51	2.9 ± 0.2	12.1 ± 0.3
5Mo	1140 ± 78	1749 ± 98	3.4 ± 0.7	8.9 ± 0.7	633 ± 75	2095 ± 89	3.3 ± 0.3	18.3 ± 0.2
7Mo	1130 ± 69	1890 ± 107	3.2 ± 0.4	11.2 ± 1.0	504 ± 54	2295 ± 98	3.8 ± 0.5	21.6 ± 0.3
9Mo	1059 ± 72	2180 ± 114	3.6 ± 0.5	14.7 ± 1.1	745 ± 46	1515 ± 49	2.6 ± 0.4	11.9 ± 0.4

In order to explain the room temperature mechanical properties, deformation and fracture mechanisms of investigated alloys fracture surfaces after room temperature compression tests were examined by SEM, as presented in Figures 5.14-5.16. It is evident that all as-cast alloys are failured by intergranular decohesion independent of type and content of ternary alloying addition. These results indicate that investigated as-cast alloys are still very brittle despite the reduced yield stresses and increased plastic strains after alloying additions.

On the other hand, elimination of solidification artifacts and lattice defects with long heat-treatment resulted in generation of enhanced room temperature mechanical properties compared to as-cast counterparts. However, all heat-treated $Fe_{50}Al_{50-n}Mo_n$ alloys display lower ductility than binary heat-treated FeAl intermetallic compound because of the formation of plentiful amount of Mo_3Al precipitates after heat-treatment. Mo_3Al particles weaken the grain boundaries and lead $Fe_{50}Al_{50-n}Mo_n$ alloys to failure by intergranular decohesion (Figure 5.16) in contrast to the transgranular cleavage of heat-treated FeAl.

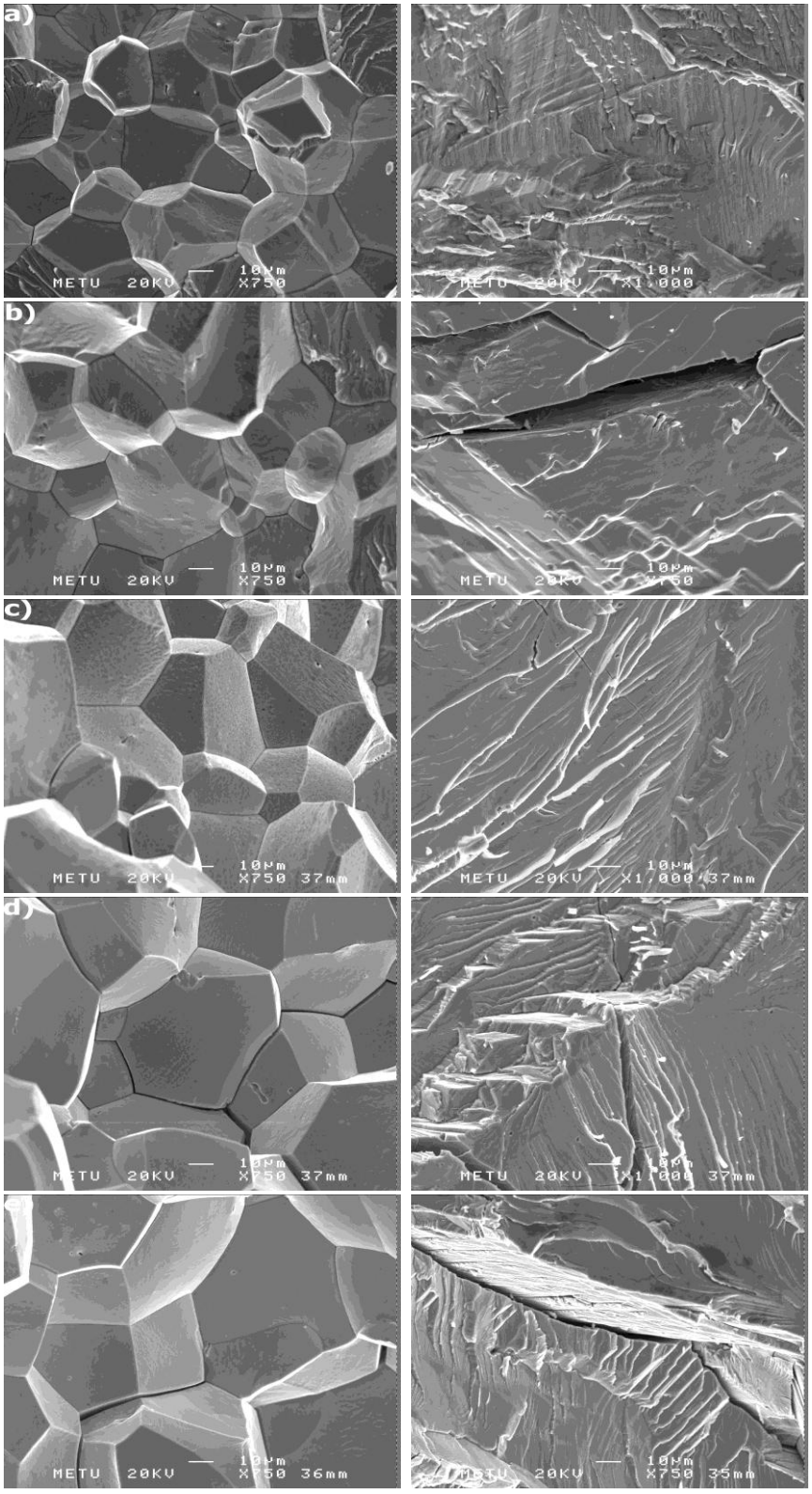

Figure 5.14 Fracture surfaces of as-cast and heat-treated (right-side) $Fe_{50}Al_{50-n}Cr_n$ alloys after compressive testing; n= (a) 1, (b) 3, (c) 5, (d) 7 and (e) 9.

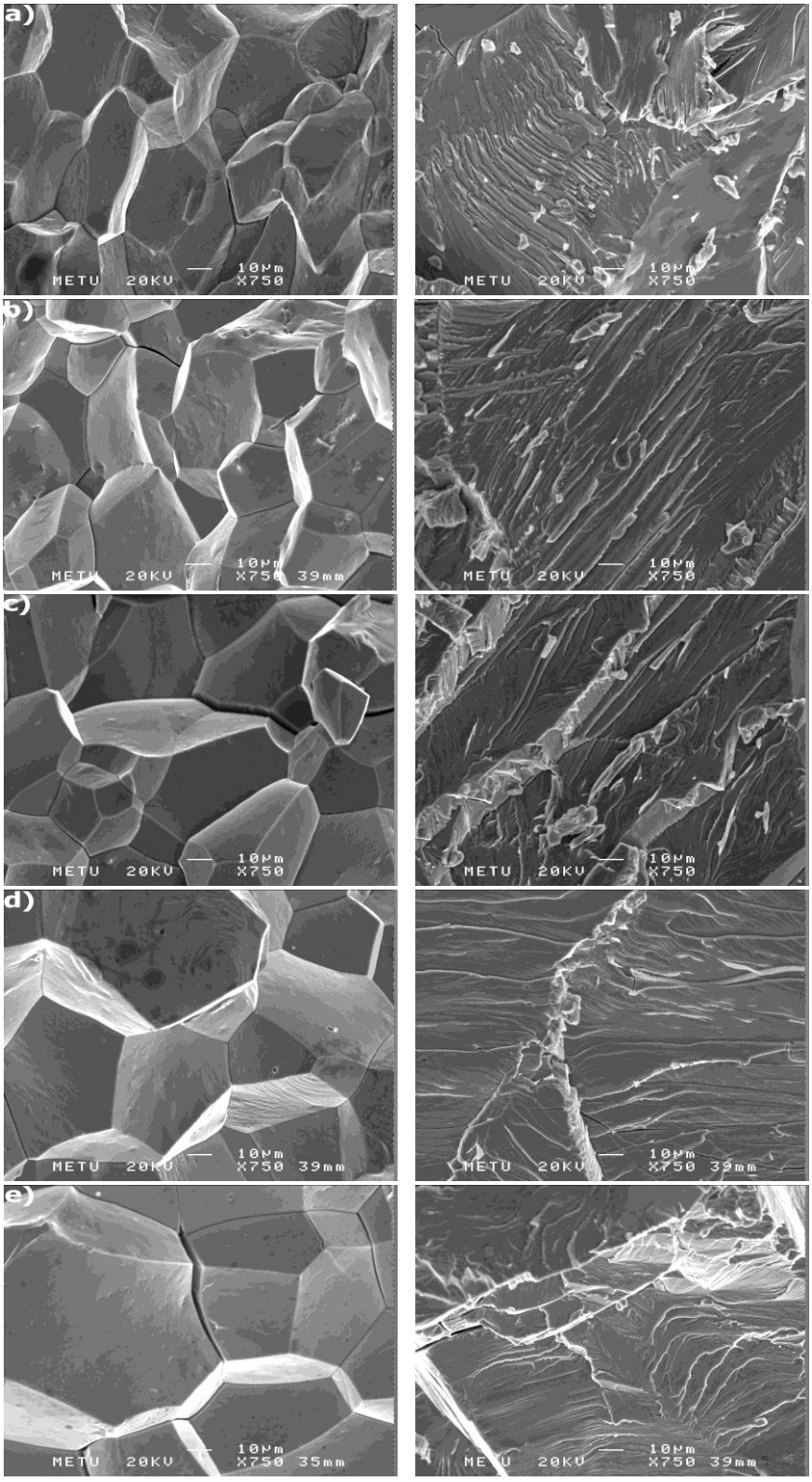

Figure 5.15 Fracture surfaces of as-cast and heat-treated (right-side) $Fe_{50}Al_{50-n}Mn_n$ alloys after compressive testing at; n= (a) 1, (b) 3, (c) 5, (d) 7 and (e) 9.

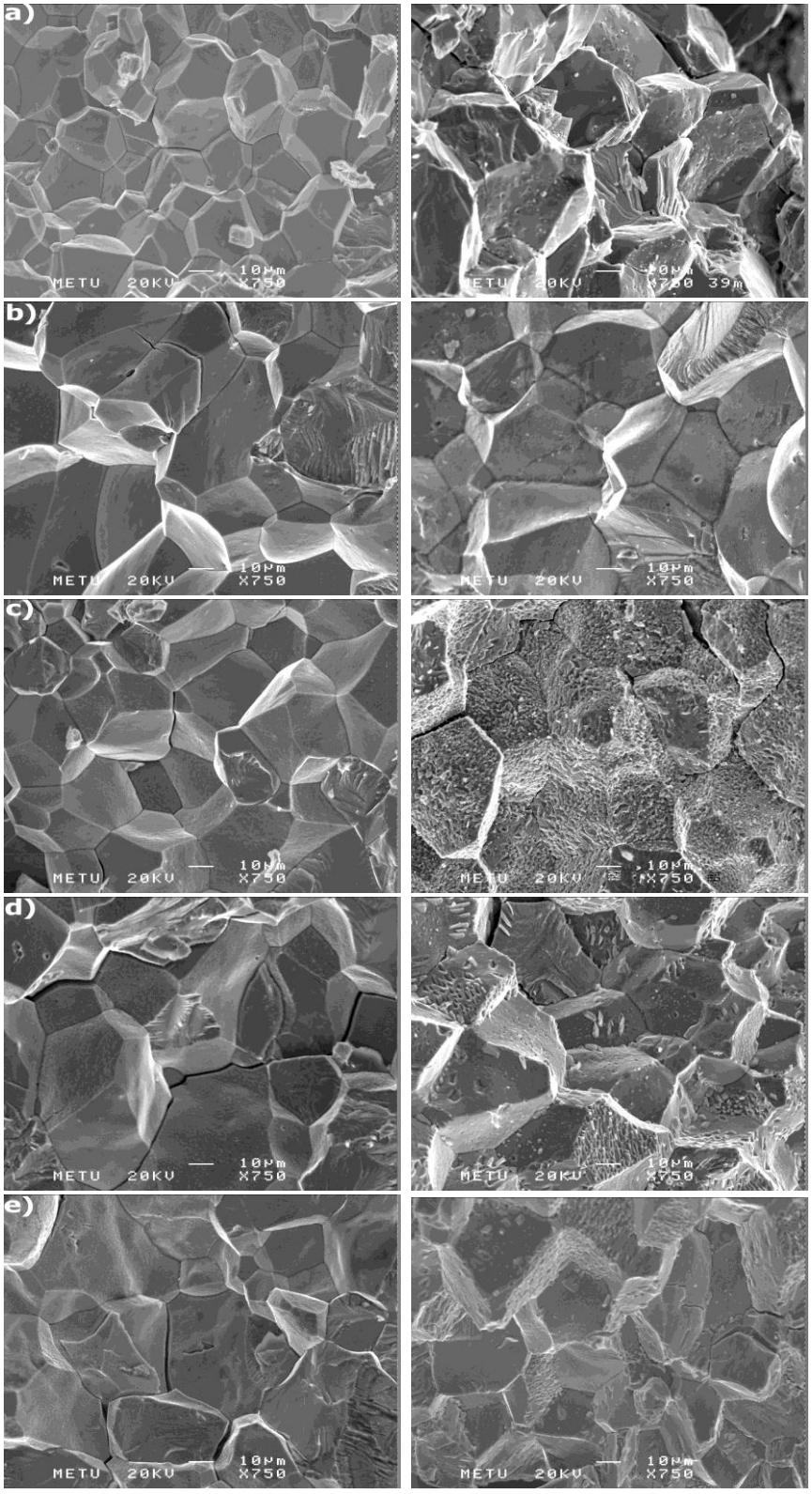

Figure 5.16 Fracture surfaces of as-cast and heat-treated (right-side) $Fe_{50}Al_{50-n}Mo_n$ alloys after compressive testing; n= (a) 1, (b) 3, (c) 5, (d) 7 and (e) 9.

Yield stresses of both $Fe_{50}Al_{50-n}Cr_n$ and $Fe_{50}Al_{50-n}Mn_n$ heat-treated alloys decrease gradually with increasing Cr and Mn content. This decrease is due to solid-solution softening effect of Cr and Mn which was also observed in earlier studies [46, 48]. In this study, since all investigated alloys have grain sizes around 300-400 μm, the effect of grain size on room temperature mechanical properties are excluded. Heat-treated $Fe_{50}Al_{41}Cr_9$ and $Fe_{50}Al_{43}Mn_7$ alloys exhibit the highest plastic strain values of 25.3 % and 32.3 %, in $Fe_{50}Al_{50-n}Cr_n$ and $Fe_{50}Al_{50-n}Mn_n$ alloys, respectively. In addition, fracture mechanisms of both alloy systems changed from intergranular to transgranular cleavage after heat-treatment.

5.1.4 Conclusions

Microstructures and room temperature mechanical properties of as-cast and heat-treated $Fe_{50}Al_{50-n}X_n$ with X= Cr, Mn and Mo (n= 1, 3, 5, 7 and 9 at.%) intermetallics have been investigated. All studied $Fe_{50}Al_{50-n}Cr_n$ and $Fe_{50}Al_{50-n}Mn_n$ alloys exhibit single phase solid solutions due to extended solid solubility of Cr and Mn in FeAl phase, whereas microstructures of all $Fe_{50}Al_{50-n}Mo_n$ compositions is composed of FeAl + Mo_3Al precipitates due to limited solid solubility of Mo in FeAl phase. Volume fraction of Mo_3Al precipitates increase with increasing Mo content. The summary of the outcomes related to the room temperature mechanical properties is as follows. In as-cast alloys, yield stress decreases and plastic strain increases with increasing alloying element content. All as-cast alloys failure by intergranular decohesion. Room temperature mechanical properties significantly increased after heat-treatment except for $Fe_{50}Al_{50-n}Mo_n$ alloys. Heat-treated $Fe_{50}Al_{50-n}Mn_n$ alloys display best room temperature ductility. Among them, $Fe_{50}Al_{43}Mn_7$ alloy has the highest plastic strain value of 32.3 %. Cr addition does not have important effect on room temperature ductility of heat-treated FeAl. The fracture mechanism of $Fe_{50}Al_{50-n}Cr_n$ and $Fe_{50}Al_{50-n}Mn_n$ alloys changed from intergranular to transgranular after heat-treatment. Heat-treated $Fe_{50}Al_{50-n}Mo_n$ alloys have lower plastic strain values than binary FeAl due to plentiful formation of Mo_3Al precipitates after heat-treatment.

5.2 Nb addition

Much attempt has been performed and is still being performed in order to improve the insufficient mechanical properties of Fe-Al based alloys at room temperature. In this particular aspect, doping iron aluminides with ternary alloying additions and thermal treatments seem to be the effective ways to increase room temperature ductility and toughness [8, 11, 13, 14].

However, ternary alloying element additions generally resulted in either enhanced plasticity with reduced strength in the case of solid solution strengtheners [9, 11, 49, 56, 58] or improved strength with reduced plasticity in the case of precipitation hardeners [59, 62, 63, 81, 131, 132]. Therefore, it is of research interest to develop an alloy that provides the best combination of mechanical properties by means of large plasticity with high strength at room temperature. In this manner, ultrafine eutectic alloys show extraordinary mechanical properties at ambient temperatures owing to their bimodal microstructure composed of relatively soft micrometer scale dendrites and hard nanoscale eutectic mixture which are responsible for high plasticity and high strength, respectively [73, 74, 133-136]. Among Fe-Al based eutectic alloys, Fe-Al-Nb alloys having such a bimodal solidification microstructure are the attractive ones as the Fe-Al-Nb ternary phase diagram contains several eutectic points due to the deep eutectic valley between C14 $(Fe, Al)_2Nb$ Laves phase and A2 (α-Fe) and B2 FeAl phases [68-71].

Park et al. [73] reported that as-cast hypoeutectic $Fe_{54}Al_{40}Nb_6$ alloy exhibits a combination of compressive strength of 2.24 GPa and 12 % plasticity. In other study, they also presented an as-cast hypoeutectic $Fe_{56}Al_{40}Nb_4$ alloy showing compressive strength of 2.32 GPa and plasticity of 11 % [74]. On the other hand, eliminating solidification artefacts and lattice defects with proper heat-treatment would be very important for getting highly enhanced ductility at room temperature. Therefore, it is predicted that heat-treatment might further improve the room temperature mechanical properties of ultrafine Fe-Al-Nb alloys. In this study, we report on a systematic investigation of the microstructures, room temperature mechanical

properties and deformation mechanisms of off-eutectic and eutectic $Fe_{50}Al_{50-n}Nb_n$ alloys (n=1, 3, 5, 7 and 9 at.%) upon solidification and subsequent heat-treatment. We find that heat-treated hypoeutectic $Fe_{50}Al_{47}Nb_3$ alloy exhibits best combination of ultimate compressive strength of 3.02 GPa and ductility of 28.1 %, which is highly larger than that of as-cast alloys. Moreover, emphasis was directed toward providing the correlation between microstructures and room temperature mechanical properties.

5.2.1 Microstructure and Phase Analysis

Solidification microstructure of as-cast and heat-treated $Fe_{50}Al_{50-n}Nb_n$ ($0 < n < 9$) alloys consists of primarily solidified B2-type Fe-Al based dendrites and interdendritic eutectic regions (Figures 5.17(a) through (d)). Volume fraction of the eutectic mixture increases with increasing Nb content up to 9 at.% Nb (Table 5.6), at which eutectic mixture undergoes one phase instability leading to development of ultrafine eutectic morphology free of primarily solidified dendrites (Figure 5.17(e)).

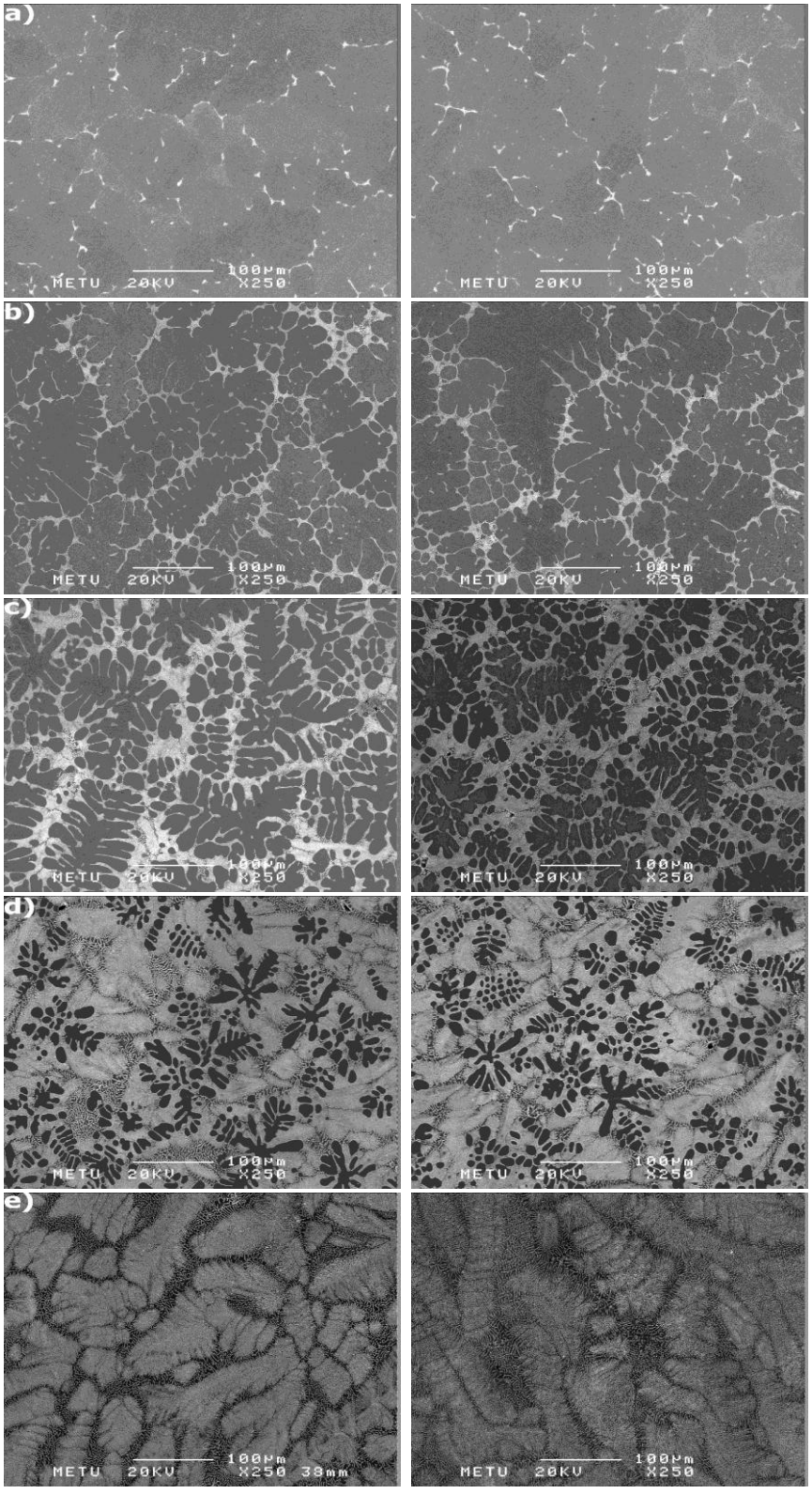

Figure 5.17 SEM micrographs of as-cast and heat-treated (right-side) $Fe_{50}Al_{50-n}Nb_n$ alloys; n= (a) 1, (b) 3, (c) 5, (d) 7 and (e) 9.

Table 5.6 Volume fraction of the eutectic mixture determined from SEM micrographs of as-cast and heat-treated $Fe_{50}Al_{50-n}Nb_n$ alloys.

Alloy	Volume fraction of eutectic	
	As-cast	Heat-treated
1 Nb	1.0	1.0
3 Nb	10.2	9.6
5 Nb	29.5	26.0
7 Nb	74.8	71.5
9 Nb	100.0	100.0

Addition of Nb into B2-type ordered FeAl intermetallic compound, even at a very small amount (i.e., 1 at.%), results in formation of C14-type $(Fe, Al)_2Nb$ Laves phase (space group 194, $P6_3/mmc$), which is one of the main constituent phase of the eutectic microstructure with B2-type Fe-Al based phase (space group 221, Pm m) as shown by the XRD analyses (Figure 5.18). The increase in the relative intensities of $(Fe, Al)_2Nb$ Laves phase strongly indicates the increase in volume fraction of this phase.

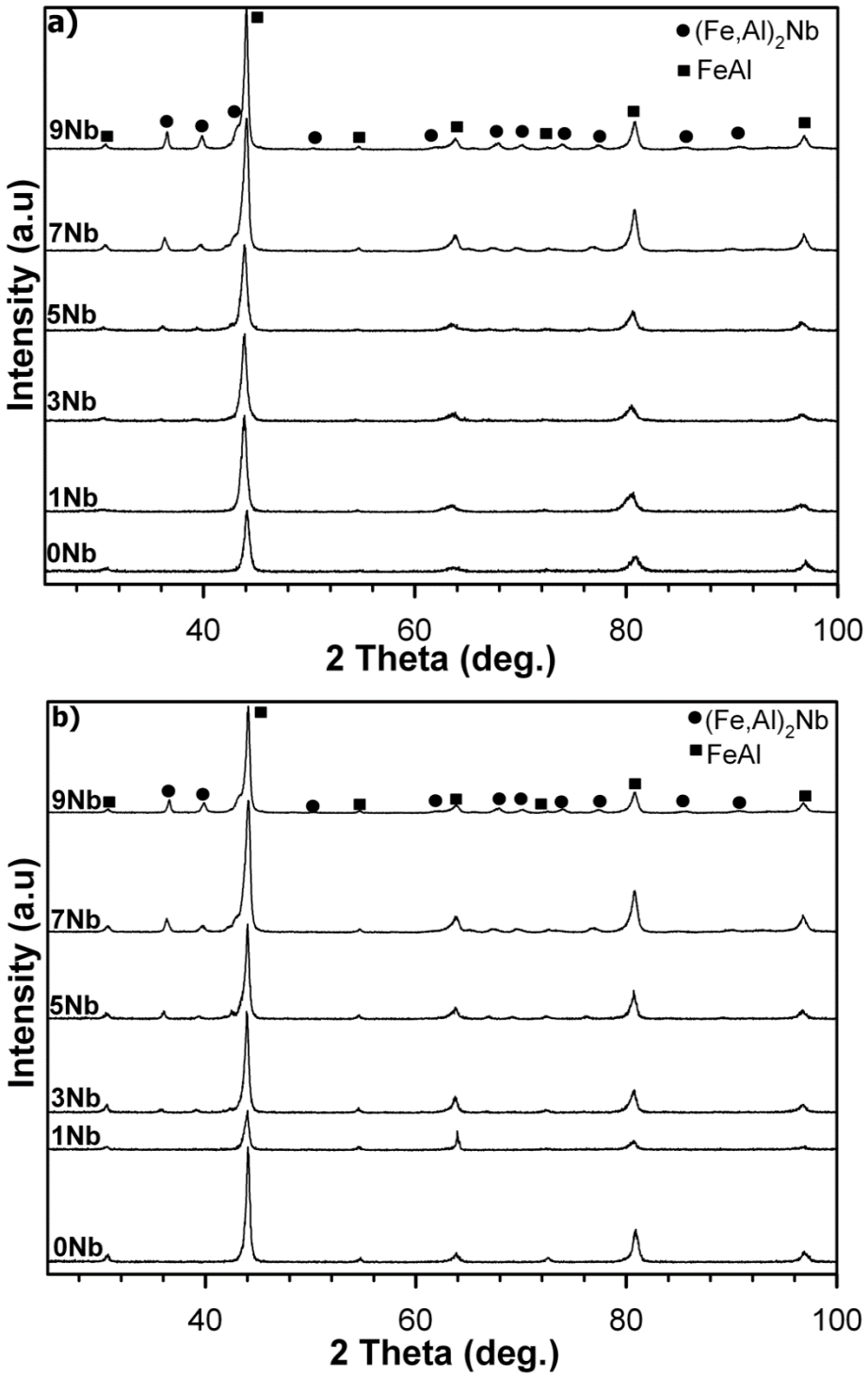

Figure 5.18 XRD patterns of $Fe_{50}Al_{50-n}Nb_n$ alloys (a) as-cast and (b) heat-treated.

The primary solidified phases can be identified as non-faceted B2-type Fe-Al based dendrites having equiaxed morphology for all off-eutectic compositions. The amount of Nb dissolved in the Fe-Al based proeutectic phases is nearly 3 at.% as determined by the EDS analysis (Table 5.7). Moreover, EDS analysis also demonstrated that Fe and Al contents in the Fe-Al based phases deviate from their actual composition especially for 5 and 7 at.% Nb containing alloys because of the higher volume fraction of Laves phase. The eutectic composition ($Fe_{50}Al_{41}Nb_9$) determined from microstructural examinations and solubility of Nb in Fe-Al based phase have very good agreement with literature data. Prymak and Stein [69] reported the solubility of Nb in B2 type Fe-Al as nearly 3 at.%, while Mota et al. [71] found the eutectic composition as Fe-41.2Al-9.1Nb for higher Al containing Fe-Al-Nb ternary alloys.

Table 5.7 The results of the EDS analysis of primary solidified dendrites of $Fe_{50}Al_{50-n}Nb_n$ alloys.

Nb content (at.%)	EDS analysis (at.%)					
	As-cast			Heat-treated		
	Fe	Al	Nb	Fe	Al	Nb
1	49.7 ± 0.4	49.0 ± 0.3	1.3 ± 0.1	49.9 ± 0.4	49.0 ± 0.3	1.1 ± 0.1
3	50.1± 0.4	46.8± 0.4	3.1± 0.3	49.8 ± 0.4	46.9 ± 0.4	3.3 ± 0.3
5	53.9± 0.4	42.9± 0.5	3.2± 0.1	54.1 ± 0.4	42.7 ± 0.5	3.2 ± 0.2
7	55.4± 0.8	41.6± 0.7	3.0± 0.2	55.8 ± 0.8	41.2 ± 0.7	3.1 ± 0.2

Closer inspection of the microstructure by high magnification SEM analyses (Figure 5.18) has revealed that eutectic structure is composed of ultrafine lamellas and fibers of $(Fe, Al)_2Nb$ Laves phase for as-cast $Fe_{50}Al_{50-n}Nb_n$ alloys ($1<n\leq9$). No significant differences in morphology, distribution and volume fraction of existent phases have been observed after annealing.

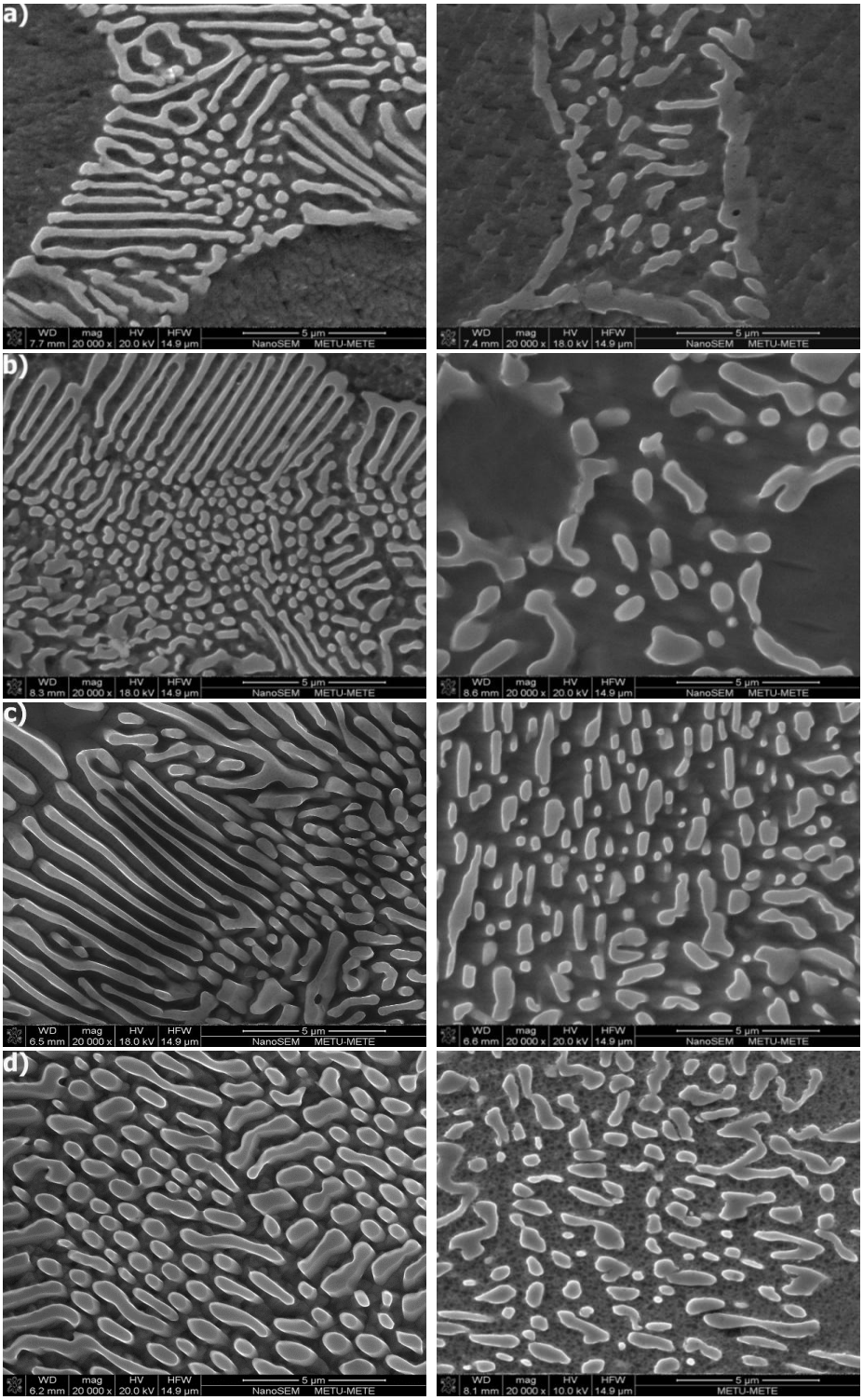

Figure 5.19 FESEM micrographs of as-cast and heat-treated (right-side) $Fe_{50}Al_{50-n}Nb_n$ alloys n= (a) 3, (b) 5, (c) 7 and (d) 9.

However, coarsening of the eutectics took place with increasing interlamellar and fiber distances, and increasing the fraction of eutectic free space. Lamellas of (Fe, $Al)_2Nb$ Laves phase transformed to fibers and particles after heat-treatment. At high temperatures, eutectic structures may tend to coarsen in order to reduce the interfacial area and improve the interfacial bond strength [137, 138]. Coarsening behavior of eutectics is a critical factor in high temperature applications, determines the thermal stability of alloy over long period of time at sufficiently high temperatures [72, 133]. These microstructural observations illustrate that investigated $Fe_{50}Al_{50-n}Nb_n$ alloys possess good thermal stability, which makes them suitable candidates for structural applications at high temperatures.

5.2.2 Compression Test and Fractographic Analysis

The effect of microstructural observations on room temperature mechanical properties of as-cast and heat-treated $Fe_{50}Al_{50-n}Nb_n$ alloys have been investigated by uniaxial compression test as shown in Figure 5.20. Compressive stress-strain curves for as-cast and heat-treated FeAl intermetallic compound are also provided for comparison. Table 5.8 summarizes the values of yield strength, maximum compressive strength, yield strain and plastic strain determined from room temperature compression tests. Compared to as-cast binary FeAl, heat-treated FeAl exhibit significantly improved plasticity. Moreover, its fracture mode (Figure 5.21(a)) changed from intergranular decohesion to transgranular cleavage after heat-treatment.

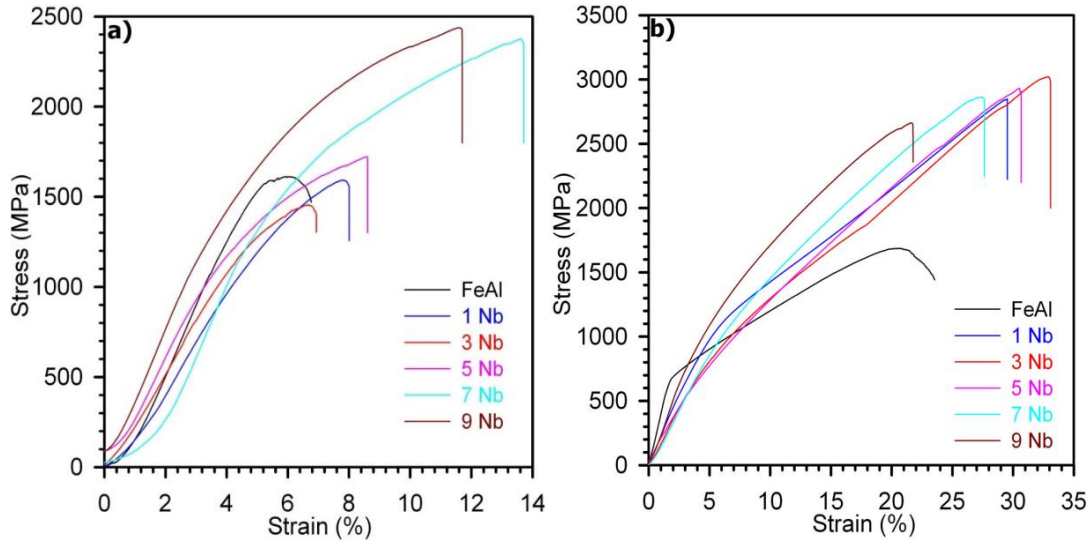

Figure 5.20 Room temperature stress-strain compression curves of $Fe_{50}Al_{50-n}Nb_n$ alloys (a) as-cast (b) heat-treated.

Among as-cast ternary alloys, hypoeutectic $Fe_{50}Al_{50-n}Nb_n$ alloys with 1, 3 or 5 at.% Nb show similar mechanical properties with binary as-cast FeAl. They all exhibited low plastic strain values at room temperature. Brittle nature of these specimens has also been observed with fracture surface analysis (Figure 5.21(b)-(f)). As-cast $Fe_{50}Al_{49}Nb_1$ alloy was failured predominantly by intergranular decohesion. Intergranular facets exhibited roughness because of the presence of brittle Laves phase particles on the grain boundaries. However, the fracture surfaces of as-cast $Fe_{50}Al_{47}Nb_3$ and $Fe_{50}Al_{45}Nb_5$ specimens consist of dendrites and pores in interdendritic regions. The formation of the pores is attributed to the solidification shrinkage which arises from the temperature difference between the solidus and liquidus/eutectic temperatures [139, 140]. In addition, the amount of pores is large when the volume fraction of the dendrites is high. These pores led $Fe_{50}Al_{47}Nb_3$ and $Fe_{50}Al_{45}Nb_5$ specimens to failure along the free surfaces of dendrites and spaces between dendrites, which are responsible for poor mechanical properties at room temperature [141].

Table 5.8 Mechanical properties for the as-cast and heat-treated $Fe_{50}Al_{50-n}Nb_n$ alloys: yield stress σ_y (0.2% offset), ultimate compressive stress σ_{max}, strain at the yield point ε_y and plastic strain ε_p.

Nb content (at.%)	As-cast				Heat-treated			
	σ_y (MPa)	σ_{max} (MPa)	ε_y (%)	ε_p (%)	σ_y (MPa)	σ_{max} (MPa)	ε_y (%)	ε_p (%)
0	1449 ± 92	1657 ± 69	4.4 ± 0.4	2.4 ± 0.3	673 ± 55	1687 ± 46	1.9 ± 0.1	21.7 ± 0.6
1	1175 ± 86	1592 ± 93	4.9 ± 0.5	3.1 ± 0.3	973 ± 62	2841 ± 104	4.7 ± 0.2	24.8 ± 0.7
3	1223 ± 72	1454 ± 47	4.7 ± 0.5	2.2 ± 0.3	909 ± 58	3020 ± 95	5.0 ± 0.3	28.1 ± 0.6
5	1257 ± 65	1713 ± 71	3.5 ± 0.4	5.1 ± 0.5	935 ± 71	2932 ± 86	6.5 ± 0.3	24.2 ± 0.7
7	1302 ± 76	2376 ± 98	5.0 ± 0.4	8.7 ± 0.7	1012 ± 65	2863 ± 78	6.1 ± 0.3	21.5 ± 0.5
9	1318 ± 61	2437 ± 107	3.6 ± 0.4	8.1 ± 0.7	1051 ± 73	2662 ± 76	4.8 ± 0.2	17.0 ± 0.4

When the amount of Nb reached to 7 or 9 at.%, the compressive strength and room temperature plasticity considerably increased. Nevertheless, it is important to note that eutectic $Fe_{50}Al_{41}Nb_9$ alloy without any primary dendrites show relatively enhanced mechanical properties. These results are primarily related to the microstructural features including the volume fraction, size, morphology and distribution of the constituent phases. Higher volume fraction of relatively harder $(Fe, Al)_2Nb$ Laves phase and the length scale of the eutectic mixture resulted in generation of higher compressive strength. On the other hand, the reasonably higher plasticity of these alloys is mainly attributed to the morphologies of the fracture surfaces. The fracture surfaces of as-cast near-eutectic $Fe_{50}Al_{43}Nb_7$ and eutectic $Fe_{50}Al_{41}Nb_9$ alloys reveal that there is smooth cleavage in the Fe-Al based matrix and interface decohesion at the (Fe-Al)/$(Fe, Al)_2Nb$ eutectics. Ashby et al. [142] presented that interface decohesion has a significant effect on improvement of fracture toughness and Li et al. [138] pointed out that interface decohesion play an important role to increase plasticity. Thus, better mechanical properties of $Fe_{50}Al_{43}Nb_7$ and $Fe_{50}Al_{41}Nb_9$ alloys can be explained above microstructural and fractographic observations. Moreover, mechanical properties of 7 or 9 at.% Nb containing alloys are comparable to previously reported ternary Fe-Al-Nb alloys [73, 74]. For example, Park et al. [73] presented that hypoeutectic $Fe_{54}Al_{40}Nb_6$ alloy has yield strength, compressive strength and plastic strain of 1.25 GPa, 2.24 GPa and 12 %, respectively. They also reported [74] that hypoeutectic $Fe_{56}Al_{40}Nb_4$ alloy show yield strength, compressive strength and plastic strain of 1.12 GPa, 2.32 GPa and 11 %, respectively.

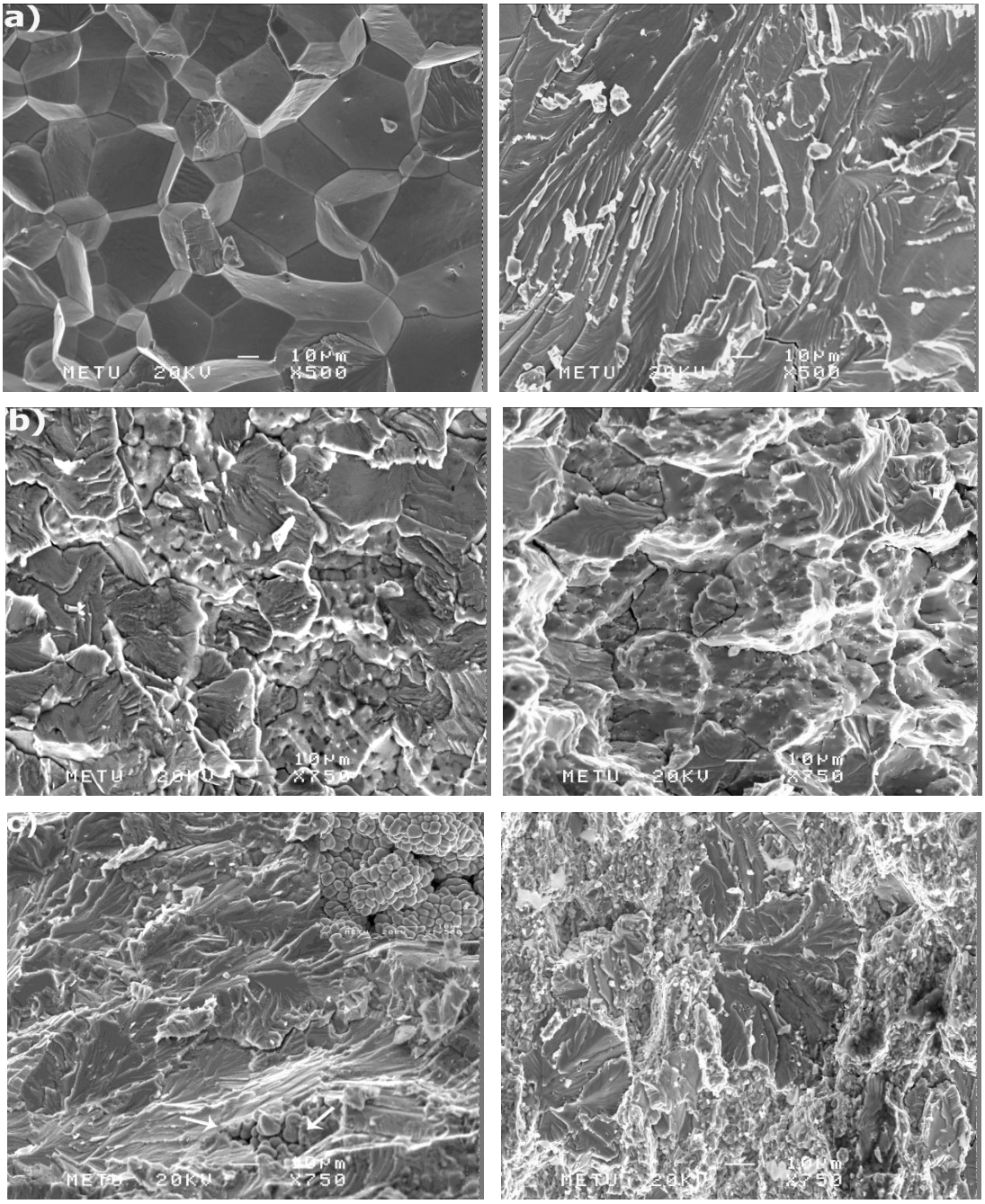

Figure 5.21 SEM images of the fracture surfaces of as-cast and heat-treated (right-side) $Fe_{50}Al_{50-n}Nb_n$ alloys after compression test at room temperature n= (a) 0, (b) 1, (c) 3, (d) 5, (e) 7 and (f) 9.

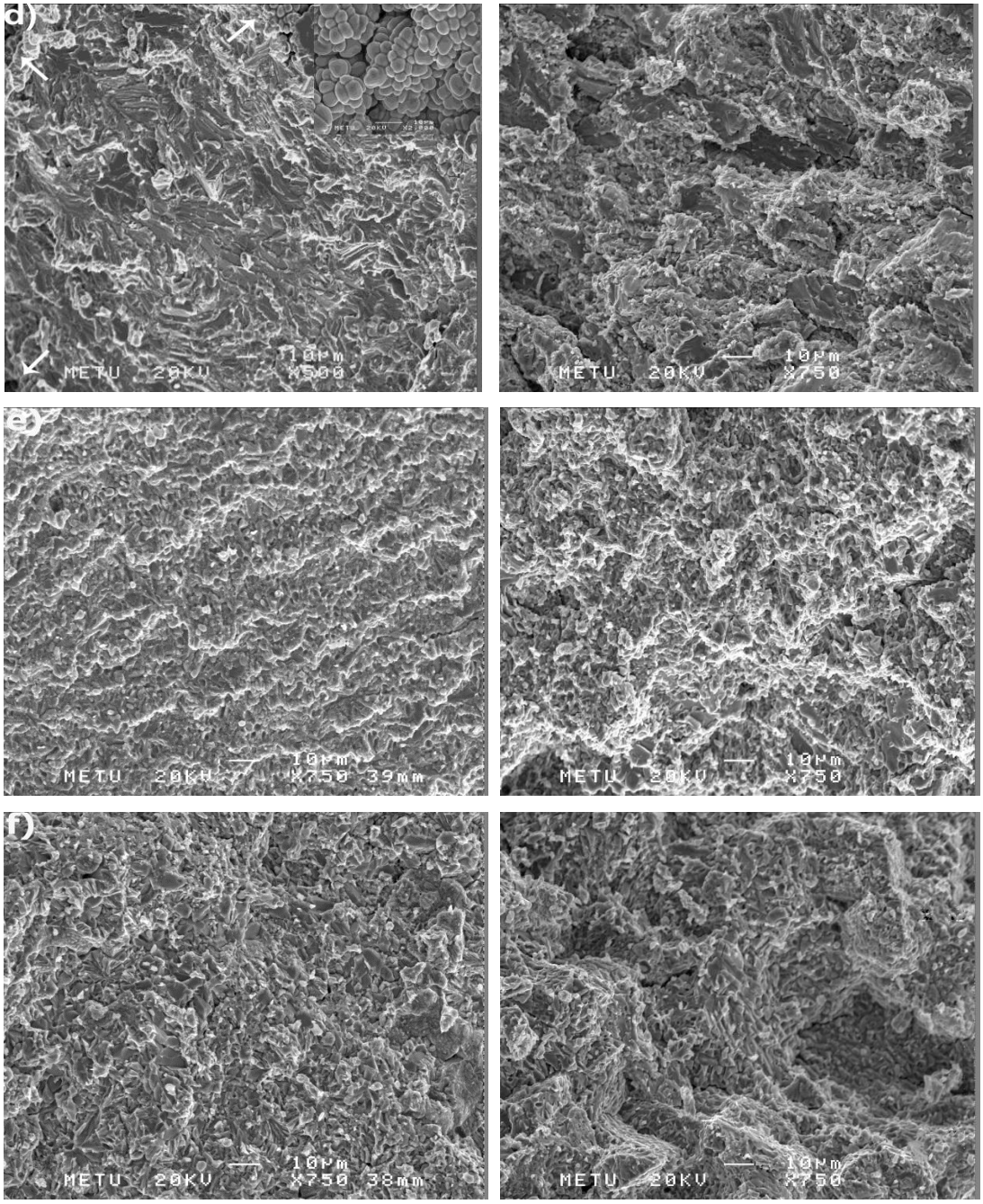

Figure 5.21 (cont'd) SEM images of the fracture surfaces of as-cast and heat-treated (right-side) $Fe_{50}Al_{50-n}Nb_n$ alloys after compression test at room temperature n= (a) 0, (b) 1, (c) 3, (d) 5, (e) 7 and (f) 9.

Uniaxial compressive stress-strain curves for heat-treated $Fe_{50}Al_{50-n}Nb_n$ alloys are shown in Figure 5.20(b). Although as-cast and heat-treated alloys have similar microstructural features, room temperature mechanical properties were significantly improved after annealing. All heat-treated alloys exhibit lower yield strength, higher compressive strength and higher plastic strain compared to as-cast alloys. The decreased yield strength can be attributed to the local microstructural coarsening and the improved compressive ductility can be ascribed to the elimination of solidification artifacts and lattice defects. For as-cast alloys, solidification artifacts such as pores can act as crack initiation sites and lead to generation of poor ductility at room temperature.

The yield strength, compressive strength and yield strain of heat-treated $Fe_{50}Al_{50-n}Nb_n$ alloys do not much change with respect to Nb content. However, hypoeutectic $Fe_{50}Al_{47}Nb_3$ alloy shows the highest plastic strain of 28.1% and eutectic $Fe_{50}Al_{41}Nb_9$ alloy shows the lowest plastic strain of 17.0% due to the lack of relatively softer primary Fe-Al dendrites. In spite of the significantly high plastic strains, there is no significant evidence of plastic deformation in fracture surfaces of heat-treated specimens. Nevertheless, there is an important difference between the morphology of the fracture surfaces of as-cast and heat-treated alloys which plays an essential role to interpret enhanced mechanical properties. Heat-treated $Fe_{50}Al_{49}Nb_1$ alloy was failured by mixed transgranular cleavage and interface decohesion. Fracture surface of heat-treated $Fe_{50}Al_{47}Nb_3$ alloy, having highest plastic strain and compressive strength, shows that large primary Fe-Al based phase was fractured by transgranular cleavage, while the fracture mode of the eutectic is mainly by debonding of the interface between Fe-Al based phase and fine $(Fe, Al)_2Nb$ Laves phase. The thick river patterns are clearly seen in the primary Fe-Al phase. Contrary to heat-treated $Fe_{50}Al_{47}Nb_3$ alloy, the occurrence of smooth cleavage in the primaries of $Fe_{50}Al_{45}Nb_5$ alloy led to decrease in plastic strain values. On the other hand, heat-treated $Fe_{50}Al_{43}Nb_7$ and $Fe_{50}Al_{41}Nb_9$ alloys have very similar fracture surfaces that do not contain any features related to the presence of primary phase. Their decohesion surfaces show the interfaces between the constituents of eutectic.

The fracture surface of heat-treated specimens revealed that the fracture mode is predominantly cleavage except for $Fe_{50}Al_{49}Nb_1$ alloy despite the high plastic strains. This behavior can be explained regarding the presence of heterogeneous microstructure. In such alloys, fracture mechanism depends on various factors including the volume fraction, size and distribution of constituent phases, the strength of the interfaces, microstructural inhomogeneity and brittle cracking of intermetallics [137, 141]. For example, Sha et al. [139] reported that a mismatch at interfaces, caused by elastic modulus and thermal expansion coefficient mismatch, may result in discontinuity of deformation and different damage modes. Meanwhile, Li et al. [138] presented that the release of the dislocations from the interfaces between alternating phases firstly lets plasticity while finally cleavage is created as the local stress reaches the cleavage stress. The difference between the yield and cleavage stresses determines the amount of plasticity in the matrix phase.

Compared to other ternary intermetallic phase forming elements (Zr, Hf, Ta or Ti), Nb has the best positive effect on room temperature mechanical properties, especially the ductility of Fe-Al intermetallics. Among these transition elements, Nb, Ta and Ti show relatively larger solid solubility in Fe-Al alloys rather than Zr or Hf. Thus, the volume fraction of the hard and brittle ternary intermetallic phase is less in the case of Nb, Ta and Ti additions.

Although Nb, Ta and Ti have very similar solid solubility, Ta and Ti have detrimental effects on room temperature ductility of Fe-Al based alloys in contrast to positive effect of Nb addition [59, 135]. For the following reasons, Nb containing Fe-Al intermetallics would be good potential as an engineering material for structural applications: (i) Nb has solid solution strengthening effect due to its limited but sufficient solid solubility [143], (ii) strong work hardening during plastic deformation and (iii) enhancement of room temperature ductility because of its duplex structure.

5.2.3 Conclusions

Microstructural evolution, room temperature mechanical properties and deformation mechanisms of $Fe_{50}Al_{50-n}Nb_n$ alloys (n=1, 3, 5, 7 and 9 at.%) have been investigated in detail upon solidification and subsequent heat-treatment. $(Fe, Al)_2Nb$ Laves phase is found to form even at 1 at.% Nb addition due to limited solid solubility of Nb in FeAl. $(Fe, Al)_2Nb$ Laves phase is shown to develop a eutectic phase mixture with the Fe-Al based phase at all other investigated compositions and its volume fraction increases with increasing Nb content. The Nb concentration of the Fe-Al based phase and the eutectic composition is found to be 3 and 9 at.%, respectively. Among as-cast alloys, near-eutectic $Fe_{50}Al_{43}Nb_7$ and eutectic $Fe_{50}Al_{41}Nb_9$ alloys show reasonably higher compressive strength and plasticity. Heat-treated alloys have unique mechanical properties at room temperature by means of highly enhanced plasticity with very high compressive strength. Hypoeutectic $Fe_{50}Al_{47}Nb_3$ alloy exhibits highest ultimate compressive strength and plastic strain of 3.02 GPa and 28.1%, respectively. Eutectic $Fe_{50}Al_{41}Nb_9$ alloy shows the lowest plastic strain of 17.0 % due to the absence of relatively softer Fe-Al based primary dendrites. High strength is attributed to the presence of ultrafine eutectic mixture, while enhanced compressive plasticity is ascribed to the shear interaction between primary Fe-Al based phase and eutectic phase mixture.

5.3 Hf addition

In the preceding sections, it is shown that alloying elements with different solubilities often result in significantly different microstructural changes in Fe-Al-X alloys, which subsequently leads to a wide spectrum of mechanical properties. Among these alloying elements, Nb is the only one that exhibit remarkable combination of mechanical properties by means of high strength with large plasticity. These outstanding mechanical properties of Fe-Al-Nb alloys are attributed to the heterogeneous microstructure combined with the primary solidified Fe-Al based dendrites and ultrafine eutectic mixture.

Hafnium is an early transition metal element that is chemically close to the alloying additions of Zr, Ti, Ta and Nb, and has the potential to induce similar mechanical properties as Nb. However, there is little information provided in the literature on the structural features of Fe-Al-Hf alloys. Therefore, the potential effects of these structural features induced by Hf addition on the mechanical properties Fe-Al alloys are currently not well-known. In this study, it is of research interest to investigate the phase relationships, microstructures and microhardnesses of the off-eutectic and eutectic $Fe_{50}Al_{50-n}Hf_n$ alloys (n=1, 3, 5, 7 and 9 at.%) in detail upon solidification and subsequent heat-treatment. We find that $Fe_{50}Al_{50-n}Hf_n$ alloys solidify through a eutectic reaction, products of which are relatively soft Fe-Al based phase and a hard ternary intermetallic $HfFe_6Al_6$ phase at all investigated compositions. The solidification behavior of alloys alters from primary Fe-Al based phase to eutectic and to primary $HfFe_6Al_6$ with increasing Hf content. Based on these results, it is possible to hypothesize that the hypoeutectic $Fe_{50}Al_{50-n}Hf_n$ alloys may display superior mechanical properties like Fe-Al-Nb alloys due to their bimodal microstructure containing micrometer sized soft Fe-Al based dendrites and ultrafine eutectic mixture.

5.3.1 Microstructure and Phase Analysis

Solidification microstructure of the $Fe_{50}Al_{50-n}Hf_n$ ($0<n<7$) alloys consist of primary Fe-Al based dendrites and interdendritic eutectic structure (Figures 5.22(a)-(c)). Volume fraction of the eutectic mixture increases with increasing Hf content up to 7 at.% Hf (Table 5.9), at which eutectic mixture undergoes two phase instability leading to development of eutectic cellular morphology (Figure 5.22(d)). Addition of Hf into B2-type ordered FeAl intermetallic compound, even at a very small amount (i.e. 1 at.%), results in formation of $ThMn_{12}$-type (space group 139, I4/*mmm*) ternary intermetallic $HfFe_6Al_6$ τ_1 phase [77] which becomes one of the main constituent phases of the eutectic mixture in $Fe_{50}Al_{50-n}Hf_n$ alloys as indicated by the XRD analyses (Figure 5.23). Thermal analyses of $Fe_{50}Al_{50-n}Hf_n$ alloys reveal that the endothermic peak related to the second order FeAl (B2) ↔ α-Fe (A2) order-disorder phase transition observed in the stoichiometric FeAl intermetallic compound [28,

126, 144] is probably overshadowed by the strong eutectic reaction which takes place at 1248 °C even at 1 at.% Hf addition (Figure 5.24). A broad endothermic peak at higher temperatures refers to the liquidus of $Fe_{50}Al_{50-n}Hf_n$ alloys. This peak approaches to the eutectic reaction temperature with increasing Hf content and eventually vanishes at 7 at.% Hf which corresponds to the pseudobinary eutectic composition.

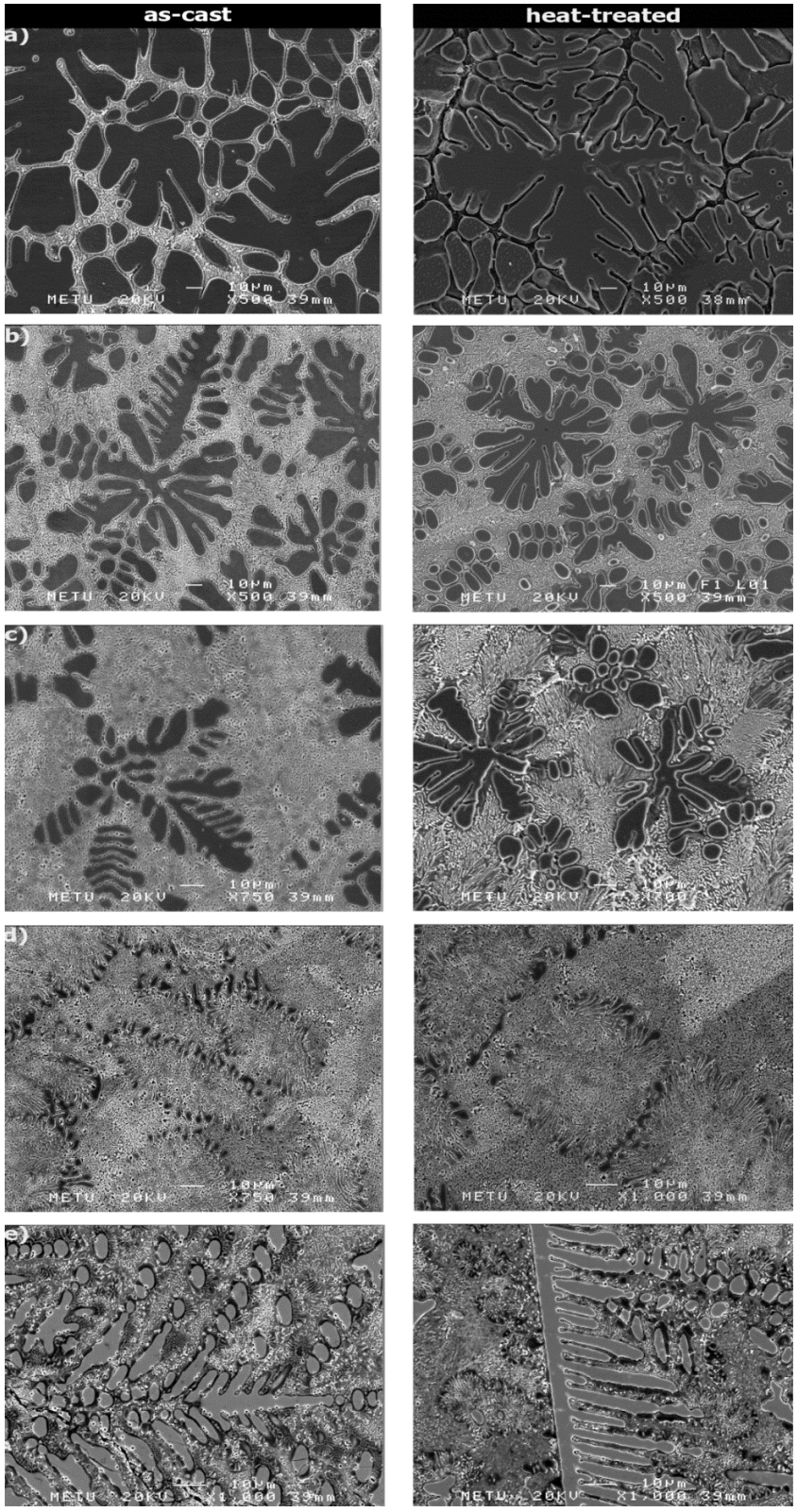

Figure 5.22 SEM micrographs of as-cast and heat-treated $Fe_{50}Al_{50-n}Hf_n$ alloys; n = (a) 1, (b) 3, (c) 5, (d) 7 and (e) 9.

Microstructural examination and XRD studies coupled with thermal analysis measurements further reveal that hypereutectic $Fe_{50}Al_{50-n}Hf_n$ alloys (n>7) solidify through the formation of primary dendrites of ternary intermetallic τ_1 phase and subsequent eutectic reaction at 1248 °C as shown in the Figure 5.22(e). However, the endothermic reaction peak corresponding to the primary solidification of the $HfFe_6Al_6$ compound does not exist in the DSC heating curve, while it is present in the DSC cooling curve shown as an inset in Figure 5.24. This is a common phenomenon that arises due to the undercooling observed when the eutectic temperature is close to the liquidus temperature [145-147]. In the heating, no change in the curve can be observed as a result of the gradual melting of the sample as temperature passes the liquidus temperature. Nevertheless, in the cooling, when a certain amount of undercooling is present in the system the first solid forms and the liquidus peak appears in the cooling curve due to the thrust of heat release [145]. Although, the primary crystallization of the phases are more pronounced in the cooling curves, the preferred method of DSC is heating since the measured transition temperatures are closer to their equilibrium values [148].

Table 5.9 Volume fraction of the eutectic mixture determined from SEM micrographs of as-cast and heat-treated $Fe_{50}Al_{50-n}Hf_n$ alloys.

Hf content	Volume fraction of eutectic	
	Heat-treated	As-cast
1	31.4	34.2
3	55.2	60.8
5	75.9	81.5
7	100	100
9	76.5	80.6

The proeutectic primary phases can be recognized as non-faceted Fe-Al based dendrites with dissolved Hf and τ_1 dendrites, for hypo- and hypereutectic alloys, respectively. The amount of Hf dissolved in the Fe-Al based primary phases is nearly 0.5 at.% as determined by the EDS analysis. In addition, EDS analyses also showed that Al content in the Fe-Al based phase deviates from its nominal composition especially for 7 and 9 at.% Hf containing alloys due to the higher volume fraction of τ_1 phase.

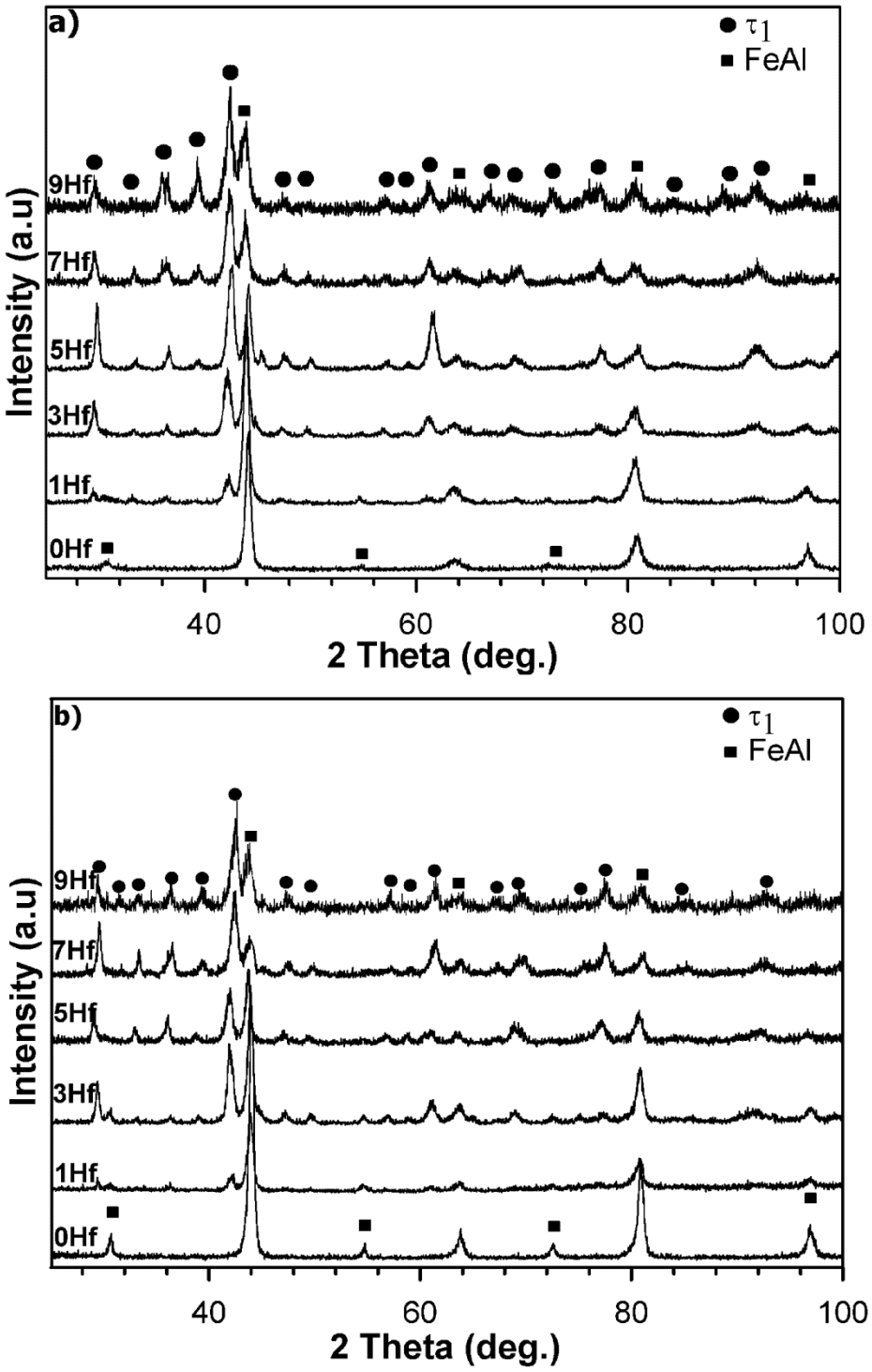

Figure 5.23 XRD patterns of $Fe_{50}Al_{50-n}Hf_n$ alloys (a) as-cast and (b) heat-treated.

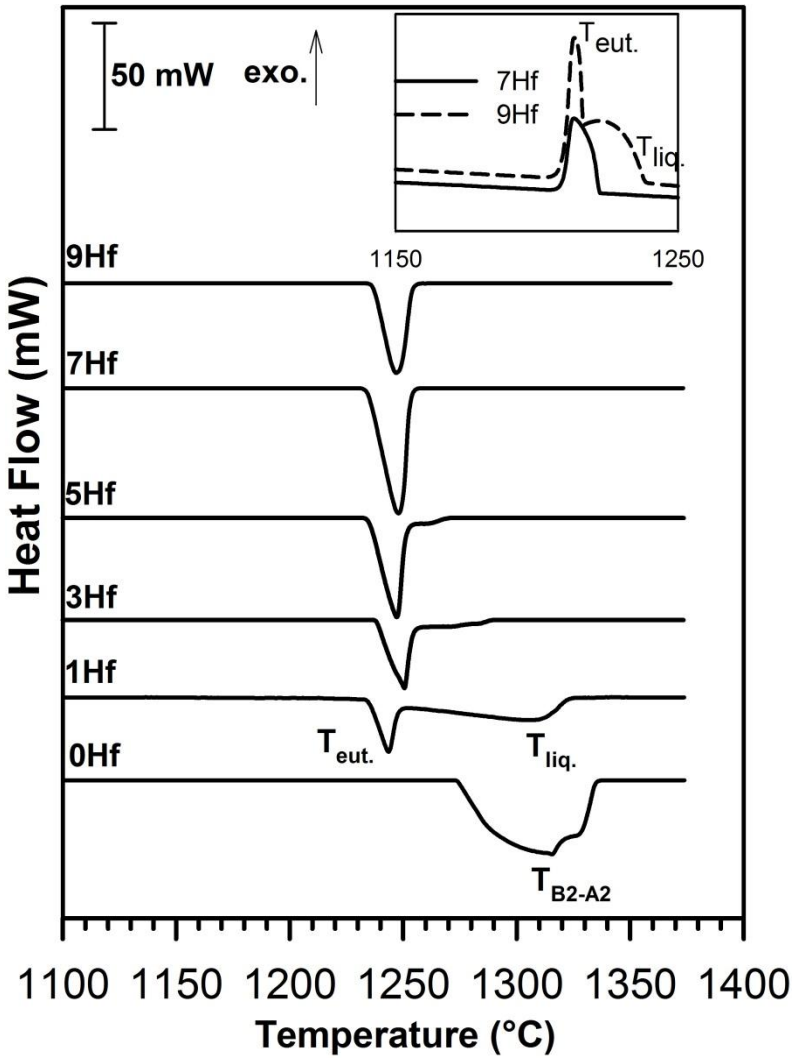

Figure 5.24 DSC heating (at a heating rate of 10K/min) curves of heat-treated $Fe_{50}Al_{50-n}Hf_n$ alloys.

In the hypereutectic $Fe_{50}Al_{41}Hf_9$ alloy (Figure 5.25), the primary τ_1 dendrites are surrounded by the halos of Fe-Al based phases. The formation of Fe-Al based halo encircling τ_1 dendrites can be explained by considering the relative interfacial energies of the existing phases [149]. According to classical nucleation theory [150, 151], interfacial energy of a phase is approximately proportional to its melting point. The τ_1 phase, therefore, is likely to have a higher interfacial energy than the Fe-Al based phase due to its higher melting point. In eutectic solidification, the phase with higher interfacial energy can generally help the nucleation of the other phase with a

lower interfacial energy, whereas the vice versa is not quite possible [152, 153]. For hypereutectic $Fe_{50}Al_{41}Hf_9$ alloy, τ_1 phase acts as an efficient substrate for the formation of the Fe-Al based phase, from which the eutectic mixture grows.

Closer inspection of the microstructure by high magnification scanning electron microscopy analyses (Figure 5.26) has revealed that hypoeutectic $Fe_{50}Al_{50-n}Hf_n$ ($0<n<7$) alloys display rod-like and/or irregular eutectic microstructures, whereas fully eutectic $Fe_{50}Al_{43}Hf_7$ alloy exhibits a cellular (colony) rod like eutectic structure (Figure 5.22(d)), with uniform distribution of fine fibers of τ_1 phase in Fe-Al based matrix. Fibers have an average thickness and an average fiber distance of 248 ± 2 nm and 550 ± 5 nm, respectively. Although the reason for the irregular lamellar to fibrous transition is not entirely understood, it is thought to be affected by the growth directions of existent phases in eutectic microstructure as reported by Motta et al. [70] for eutectic $Fe_{67.5}Al_{22.8}Nb_{9.7}$ alloy, which displays fully eutectic cellular structure like the current $Fe_{50}Al_{43}Hf_7$ alloy. According to Motta et al. [70] either the Fe-Al based phase or the τ_1 phase has an unparallel growth direction to a low-index plane, and the growth of eutectic structure takes place at low-energy semicoherent boundaries. This growth behavior yields regular fibers at the eutectic composition rather than irregular lamellas present in hypoeutectic alloys. Moreover, formation of the cellular (colony) eutectic morphology in $Fe_{50}Al_{43}Hf_7$ is probably due to destabilization of the growing solid-liquid interface by the presence of an impurity boundary layer which leads to the two-phase instability [154, 155]. A constitutionally undercooled zone is formed in front of the growing interface as a result of the rejected impurities from the eutectic. These conditions make planar solid-liquid interface unstable, and then a cellular interface can be produced [156, 157].

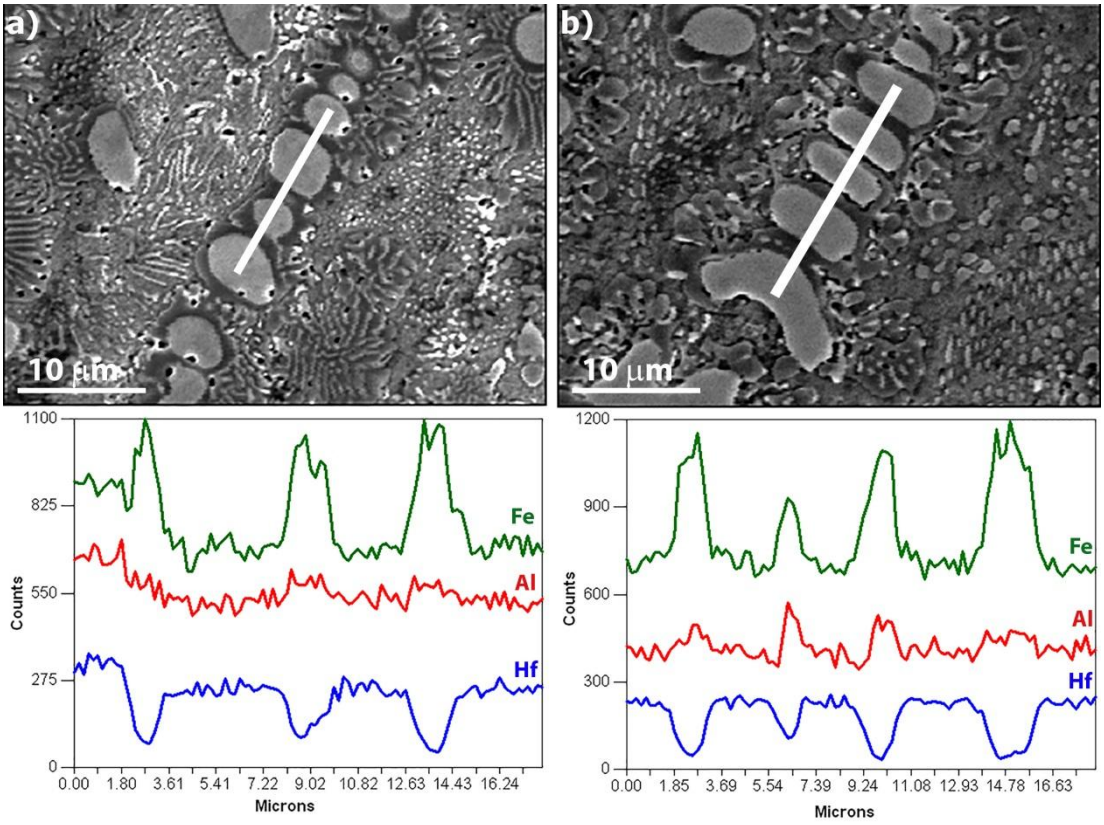

Figure 5.25 Line scan profiles of $Fe_{50}Al_{41}Hf_9$ alloys (a) as-cast (b) heat-treated.

Microstructural examination also revealed that there is no significant coarsening after long annealing times. Both as-cast and heat-treated alloys exhibit similar microstructural features. Only a decrease in volume fraction of the eutectic phase mixture (Table 5.9) is observed after annealing. These microstructural observations indicate the high thermal stability of the investigated alloys, which is a crucial factor in high temperature applications [72]. In addition to thermal stability, the ultrafine microstructure of the investigated alloys brings another advantage for fabricability and structural applications. High strengths can be achieved by the ultrafine structure of the eutectic mixture, while the bimodal microstructure can retard the shear localization and cause an enhanced plasticity at room temperature if the size and morphology of constituent phases can be controlled by proper selection of composition and solidification. Fe-Al based ternary alloys with additions of Nb, Zr, Hf, Ta or Ti may be considered as potential candidates due to their two phase nature

as a result of the limited solid solubility of Nb, Zr, Hf, Ta or Ti in Fe-Al based phases. Among these elements, Hf has a slightly larger solid solubility than Zr and less solid solubility than Nb, Ta and Ti [11, 81]. This solid solubility behavior clearly indicates that volume fraction of the ternary intermetallic compound will be considerably higher for Zr or Hf additions rather than for Nb, Ta or Ti additions even at same amount of addition.

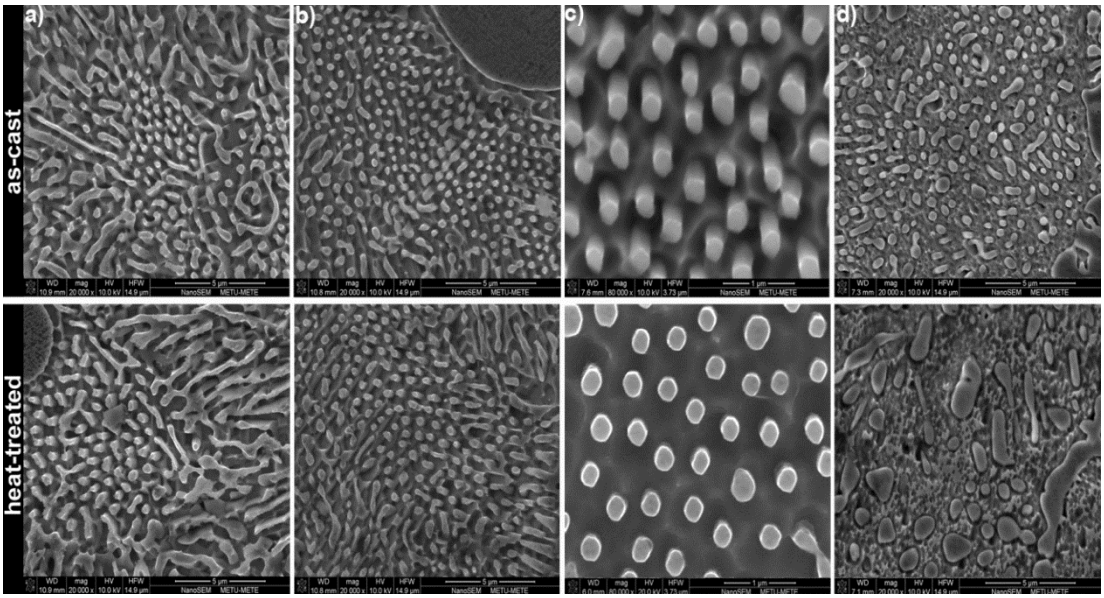

Figure 5.26 High magnification SEM micrographs of as-cast and heat-treated $Fe_{50}Al_{50-n}Hf_n$ alloys; n = (a) 3, (b) 5, (c) 7 and (d) 9.

5.3.2 Magnetic Properties

Formation of τ_1 phase in $Fe_{50}Al_{50-n}Hf_n$ alloys is further confirmed by magnetic monitoring. Magnetization measurements, presented in Figure 5.27, indicates that magnetization enhances with increasing Hf content, and hypereutectic and eutectic alloys eventually show weak ferromagnetic behavior at room temperature in contrast to the paramagnetic nature of hypoeutectic ones. Thermomagnetization measurements (Figure 5.28) and in-situ magnetic measurements (Figure 5.29) were performed in order to understand the reason for weak ferromagnetism at room temperature. According to these measurements, the measured Curie temperatures

(T_c) given in Table 5.10 for $Fe_{50}Al_{43}Hf_7$ and $Fe_{50}Al_{41}Hf_9$ ternary alloys agree well with that of $HfFe_6Al_6$ intermetallic compound reported in the literature [158], and all investigated alloys show strong ferromagnetism below their T_c. The measured transition temperatures, which are 100-120 °C below the room temperature, indicate that $HfFe_6Al_6$ τ_1 phase has no contribution to the room temperature ferromagnetism. Thus, the weak ferromagnetism at room temperature arises from the Fe-Al based phase. The Al content in the present Fe-Al based phase, which is in equilibrium with the τ_1 phase, decreases sharply in $Fe_{50}Al_{43}Hf_7$ and $Fe_{50}Al_{41}Hf_9$ ternary alloys owing to the high volume fraction of τ_1 phase. This sharp decrease also destroys the order between Fe-Al atoms and the Fe-Al phase becomes disordered. Contrary to B2-type ordered FeAl intermetallic compound, which is paramagnetic at all compositions [159, 160]; disordered Fe-Al based phase can show ferromagnetism at room temperature depending on the Al content. According to the theoretical and experimental studies [160-163], magnetic moments of Fe-Al alloys increase with decreasing Al content and alloys show ferromagnetism.

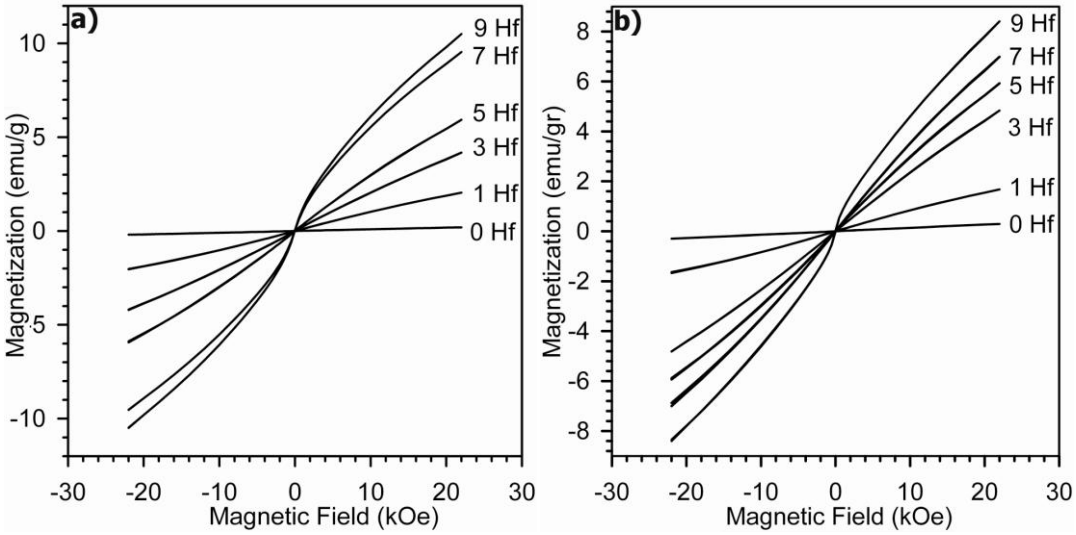

Figure 5.27 Room temperature hysteresis curves of $Fe_{50}Al_{50-n}Hf_n$ alloys (a) as-cast and (b) heat-treated.

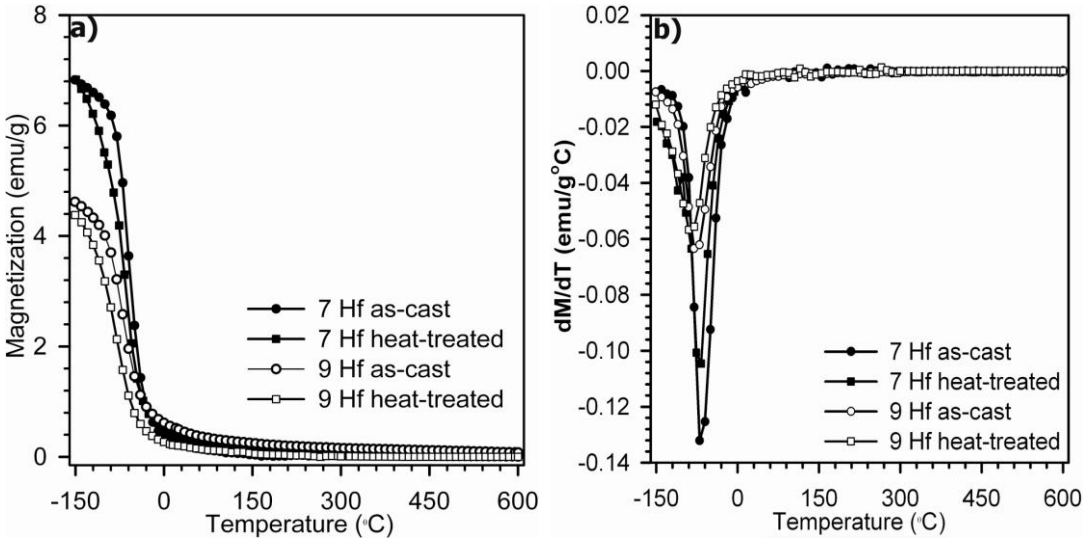

Figure 5.28 (a) Thermomagnetization and (b) (dM/dT) versus temperature curves of as-cast and heat-treated $Fe_{50}Al_{43}Hf_7$ and $Fe_{50}Al_{41}Hf_9$ alloys.

Table 5.10 Curie temperatures (T_c) of as-cast and heat-treated $Fe_{50}Al_{43}Hf_7$ and $Fe_{50}Al_{41}Hf_9$ alloys.

Alloy	T_c (°C)
$Fe_{50}Al_{43}Hf_7$ as-cast	-71.2
$Fe_{50}Al_{43}Hf_7$ heat-treated	-67.5
$Fe_{50}Al_{41}Hf_9$ as-cast	-84.7
$Fe_{50}Al_{41}Hf_9$ heat-treated	-75.0

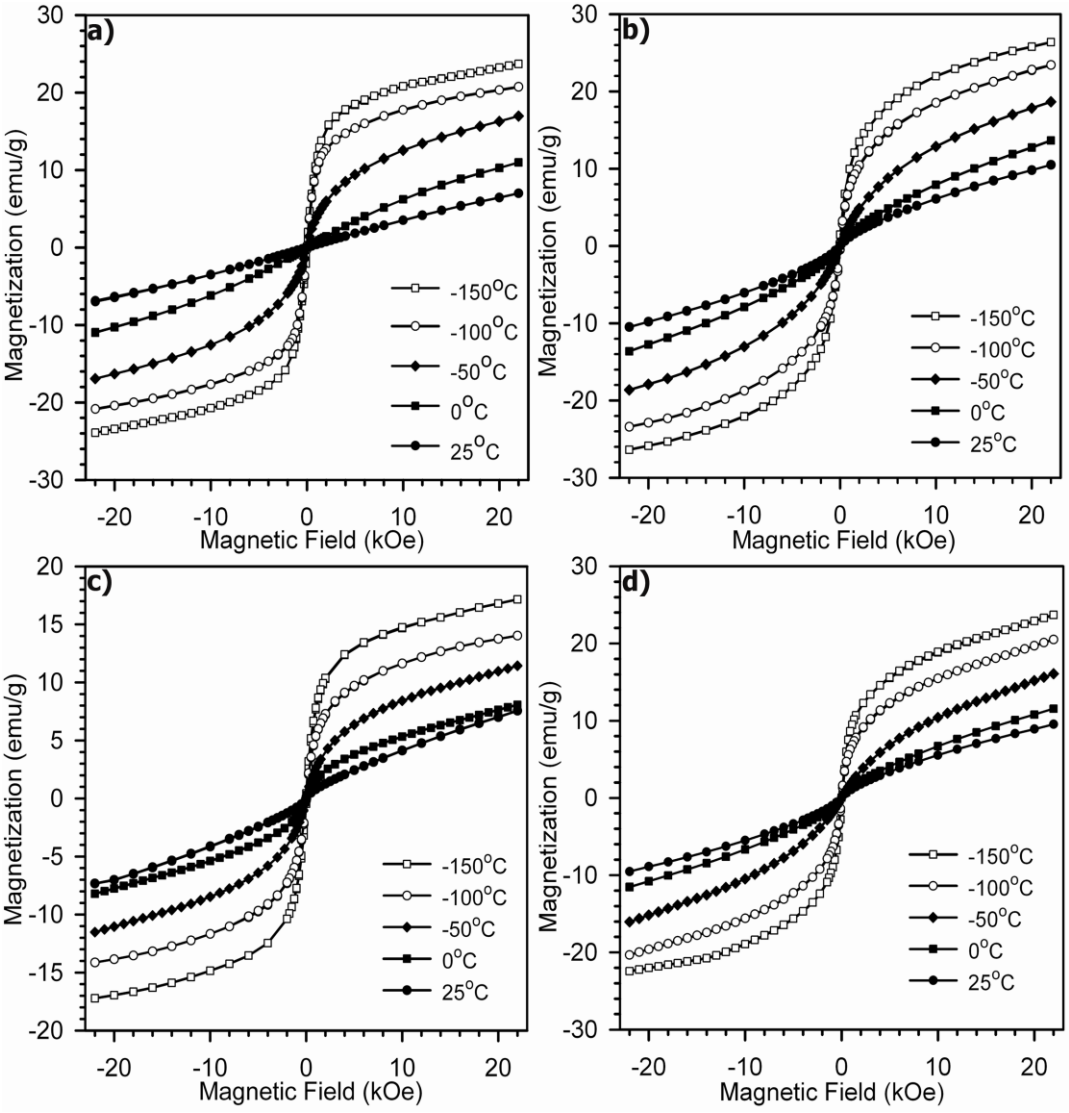

Figure 5.29 In-situ hysteresis curves for $Fe_{50}Al_{43}Hf_7$ alloy for $Fe_{50}Al_{43}Hf_7$ alloy (a) as-cast, (b) heat-treated and $Fe_{50}Al_{41}Hf_9$ alloy (c) as-cast and (d) heat-treated.

5.3.3 Kinetic Analyses of Eutectic Phase Transitions

Reaction enthalpies of the eutectic phase transitions of ternary $Fe_{50}Al_{50-n}Hf_n$ alloys are calculated based on integrated peak area method from the DSC measurements (Figure 5.24) and listed in Table 5.11. It is important to note that there is a strong correlation between calculated reaction enthalpies and structures observed in microstructural and XRD analyses of ternary alloys. Enthalpies of the eutectic

reactions increase with increasing Hf content up to eutectic composition, $Fe_{50}Al_{43}Hf_7$, and then they begin to decrease. In other words, reaction enthalpies increase with increasing Hf content when the Fe-Al based phase is the primary phase, but they decrease with the change of the primary crystallized phase from Fe-Al based phase to τ_1 phase.

Table 5.11 Endothermic reaction enthalpies of heat-treated $Fe_{50}Al_{50-n}Hf_n$ alloys.

Hf content	$\Delta H_{eut.}$ (J/g)	$\Delta H_{liq.}$ (J/g)
1	60.2	119.4
3	66.0	n.a
5	114.4	n.a
7	137.8	n.a
9	106.5	n.a

n.a* = not available

Table 5.12 Volume fraction of the eutectic mixture determined from SEM micrographs and DSC measurements of heat-treated $Fe_{50}Al_{50-n}Hf_n$ alloys.

Hf content	Volume fraction of eutectic	
	SEM	DSC
1	31.4	43.7
3	55.2	47.9
5	75.9	83.0
7	100	100
9	76.5	77.3

Moreover, volume fraction of the eutectic mixture (*f*) is predicted using the calculated enthalpies for heat-treated $Fe_{50}Al_{50-n}Hf_n$ alloys according to the relation $f = \Delta H_e / \Delta H_f$ [164] where ΔH_e is the enthalpy of eutectic reaction at a particular condition and ΔH_f is the enthalpy of eutectic reaction for alloy having fully eutectic structure. As listed in Table 5.12, calculated *f* values are found to be in very good agreement with the results obtained from the microstructural investigations carried out with scanning electron microscopy. The activation energies of the eutectic phase transitions of ternary $Fe_{50}Al_{50-n}Hf_n$ alloys were also calculated with the well-known Kissinger [165] and Ozawa [166] methods given as [Eq.5.1] and [Eq.5.2], respectively.

$$Ln\left(\frac{\beta}{T_p^2}\right) = -\frac{E_a}{RT_p} + C \tag{5.1}$$

$$Ln\,\beta = -1.052\,\frac{E_a}{RT_p} + C \tag{5.2}$$

Here, β is the heating rate, T_p is the peak temperature, R is the universal gas constant, C is a constant and E_a is the activation energy. Applying three different heating rates of 10, 20 and 30 °C/min, we calculated the activation energies given in Table 5.13 from the slopes of the plots in Figures 5.30(a) and (b). The highest activation energy is calculated as 7454.6 kJ/mol for $Fe_{50}Al_{49}Hf_1$ and it decreases with increasing Hf content for hypoeutectic alloys, reaching a minimum value of 2468.5 kJ/mol at the eutectic composition. However, activation energy starts to increase with the alteration of primary crystallized phase from Fe-Al based phase to τ_1 phase for hypereutectic $Fe_{50}Al_{41}Hf_9$ alloy. The calculated activation energies with both of the well-known Kissinger and Ozawa methods are in very good agreement.

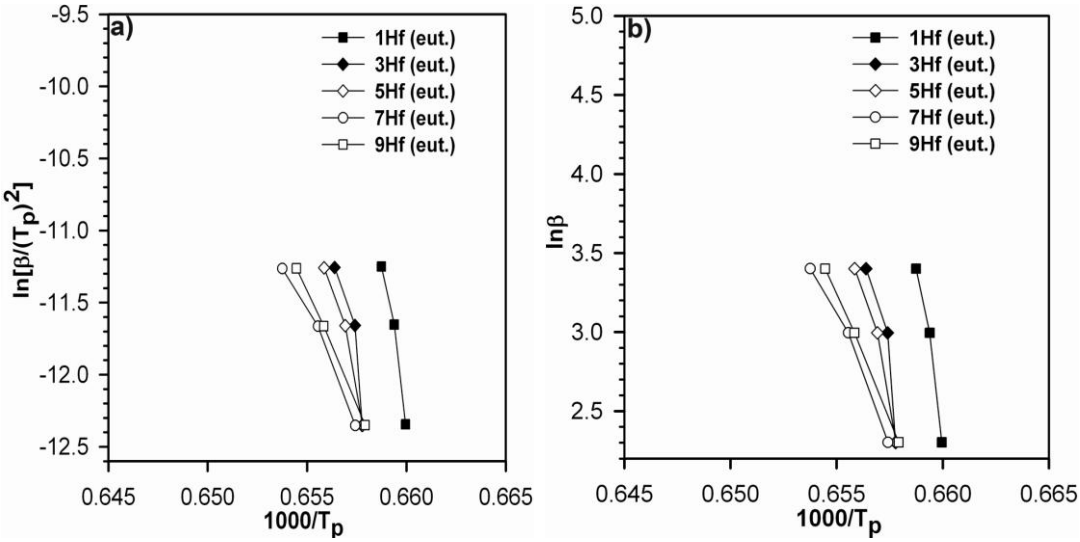

Figure 5.30 (a) The Kissinger and (b) Ozawa plots of eutectic reactions present in DSC curves of heat-treated $Fe_{50}Al_{50-n}Hf_n$ alloys.

Table 5.13 Calculated activation energies of eutectic reactions present in DSC curves of heat-treated $Fe_{50}Al_{50-n}Hf_n$ alloys according to the Kissinger and Ozawa methods (r is the linearity coefficient).

Hf content	Kissinger		Ozawa	
	E_a(kJ/mol)	$\|r\|$	E_a(kJ/mol)	$\|r\|$
1	7154.59	0.9832	7110.14	0.9833
3	5604.40	0.9126	5578.05	0.9133
5	4435.32	0.9784	4430.22	0.9786
7	2398.48	0.9901	2370.57	0.9903
9	2523.47	0.9995	2517.89	0.9995

6.1.4 Microhardness Measurements

Furthermore, strengthening effects of τ_1 phase on B2-type ordered FeAl alloys have been investigated by Vickers microhardness measurements as shown in Figure 5.31. Mean microhardness increases monotonically with Hf content, and therefore, it is maximum at 9 at.% Hf addition (the largest Hf addition in the current work). Microstructural features and phase relationships have significant effects on this observed microhardness trend in $Fe_{50}Al_{50-n}Hf_n$ alloys. For hypoeutectic compositions, heat-treated alloys have smaller microhardness values than the as-cast ones. However, for eutectic and hypereutectic compositions, heat-treated alloys have larger microhardness values than as-cast ones. The hardness of an alloy in such as-cast or heat-treated conditions strongly depends on the size and volume fraction of existing phases. Changes in the sizes of the primary phases and eutectic mixtures before and after annealing are minor in the current set of $Fe_{50}Al_{50-n}Hf_n$ alloys; thus, their microhardness values cannot be significantly influenced by the phase size. On the other hand, volume fraction of the eutectic mixtures is higher for the as-cast alloys, which implies that the volume fraction of the primary phase increases after annealing. Therefore, the increase in the volume fraction of the harder τ_1-phase after annealing results in hardening of hypereutectic alloys, whereas an increase in the volume fraction of relatively softer Fe-Al based solid solution leads to softening in the hypoeutectic alloys after annealing. Thus, as shown in Figure 5.31, annealing has opposite effects on the microhardness values of $Fe_{50}Al_{50-n}Hf_n$ alloys on either side of the eutectic composition. Compared to other alloying additions, the strengthening of Hf is similar to that of Zr because of their very similar solid solubilities in Fe-Al alloys. The volume fraction of potential ternary intermetallic compounds would obviously be higher for Zr or Hf added Fe-Al alloys rather than Nb, Ta or Ti added ones due to their minute solid solubility compared to limited solubility of Nb, Ta or Ti [11].

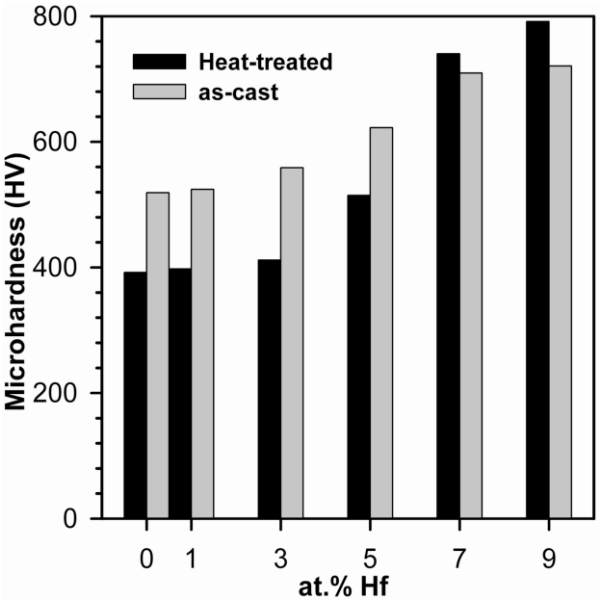

Figure 5.31 Comparison of Vickers microhardness values of as-cast and heat-treated $Fe_{50}Al_{50-n}Hf_n$ alloys.

5.3.5 Conclusions

Microstructures, phase relationships, magnetic properties and microhardness values of $Fe_{50}Al_{50-n}Hf_n$ alloys (n=1, 3, 5, 7 and 9 at.%) have been investigated. Due to the limited solid solubility of Hf in FeAl, the ternary intermetallic $HfFe_6Al_6$ τ_1 phase is found to form even at 1 at.% Hf addition. The $HfFe_6Al_6$ τ_1 phase is shown to develop a eutectic phase mixture with the Fe-Al based phase at all investigated compositions and its volume fraction increases with increasing Hf content. The Hf concentration of the Fe-Al based phase and the eutectic composition is found to be 0.5 and 7 at.%, respectively. Eutectic reaction temperature is determined as 1248 °C from the DSC measurements. Moreover, the enthalpies and activation energies (based on Kissinger and Ozawa methods) of eutectic phase transitions are calculated. Among the investigated alloys, the minimum activation energy is calculated for the fully eutectic composition. Magnetic behavior of the ternary alloys at room temperature changes from paramagnetism to weak ferromagnetism with increasing Hf content. The weak ferromagnetism observed at room temperature is attributed to the reduction in the amount of Al in the Fe-Al based phase with increasing amount of $HfFe_6Al_6$. The

magnetic moment increases with decreasing Al content, and $Fe_{50}Al_{43}Hf_7$ and $Fe_{50}Al_{41}Hf_9$ alloys exhibit ferromagnetism at room temperature. Lastly, the amount of Hf is found to have a profound effect on microhardness of the $Fe_{50}Al_{50-n}Hf_n$ alloys.

5.4 Zr Addition

In the preceding section, the effect of Hf addition on microstructures, phase relationships, magnetic properties and microhardnesses of $Fe_{50}Al_{50-n}Hf_n$ alloys (n=1, 3, 5, 7 and 9 at.%) have been investigated in detail upon solidification and subsequent heat-treatment. Zirconium is also a transition metal that is located in the same group with Hf in periodic table and is considered to have similar effects on structural properties of FeAl intermetallic compound due to their similar solid solubility behavior in FeAl phase.

In this present section, it is aimed to investigate the effect of Zr addition on structural properties of FeAl intermetallic compound and to compare the obtained results with that of preceding section. Ternary $Fe_{50}Al_{50-n}Zr_n$ alloys were prepared and examined with n=1, 3, 4, 5, 7 and 9 at.%. However, $Fe_{50}Al_{41}Zr_9$ composition was excluded since the microstructure is composed of two different ternary intermetallic phases free of any Fe-Al based phase. The solidification route of the alloys, which is very similar to that of $Fe_{50}Al_{50-n}Hf_n$ alloys, changes from primary Fe-Al based phase to eutectic and primary τ_1 $Zr(Fe, Al)_{12}$ phase. It is shown that small differences between solid solubilities of Hf and Zr may affect the microstructures and related properties.

5.4.1 Microstructure and Phase Analysis

Solidification microstructure of the $Fe_{50}Al_{49}Zr_1$ and $Fe_{50}Al_{47}Zr_3$ alloys consist of primarily solidified Fe-Al based dendrites and interdendritic eutectic mixture (Figure 5.32(a) and (b)). Volume fraction of the eutectic mixture increases with increasing Zr content up to 4 at.% Zr (Table 5.14), at which microstructure is entirely composed of eutectic free of primary phases. Addition of Zr into B2-type ordered FeAl

intermetallic compound, even at very small amount (i.e. 1 at.%), results in formation of $ThMn_{12}$-type ($D2_b$) (space group 139, I4/*mmm*) ternary intermetallic τ_1 $Zr(Fe, Al)_{12}$ phase due to very limited solid solubility of Zr in Fe-Al alloys [65, 66, 131]. $Zr(Fe, Al)_{12}$ phase becomes one of the main constituent phase of eutectic mixture with Fe-Al based phase in $Fe_{50}Al_{50-n}Zr_n$ alloys as indicated by the XRD analyses (Figure 5.33)

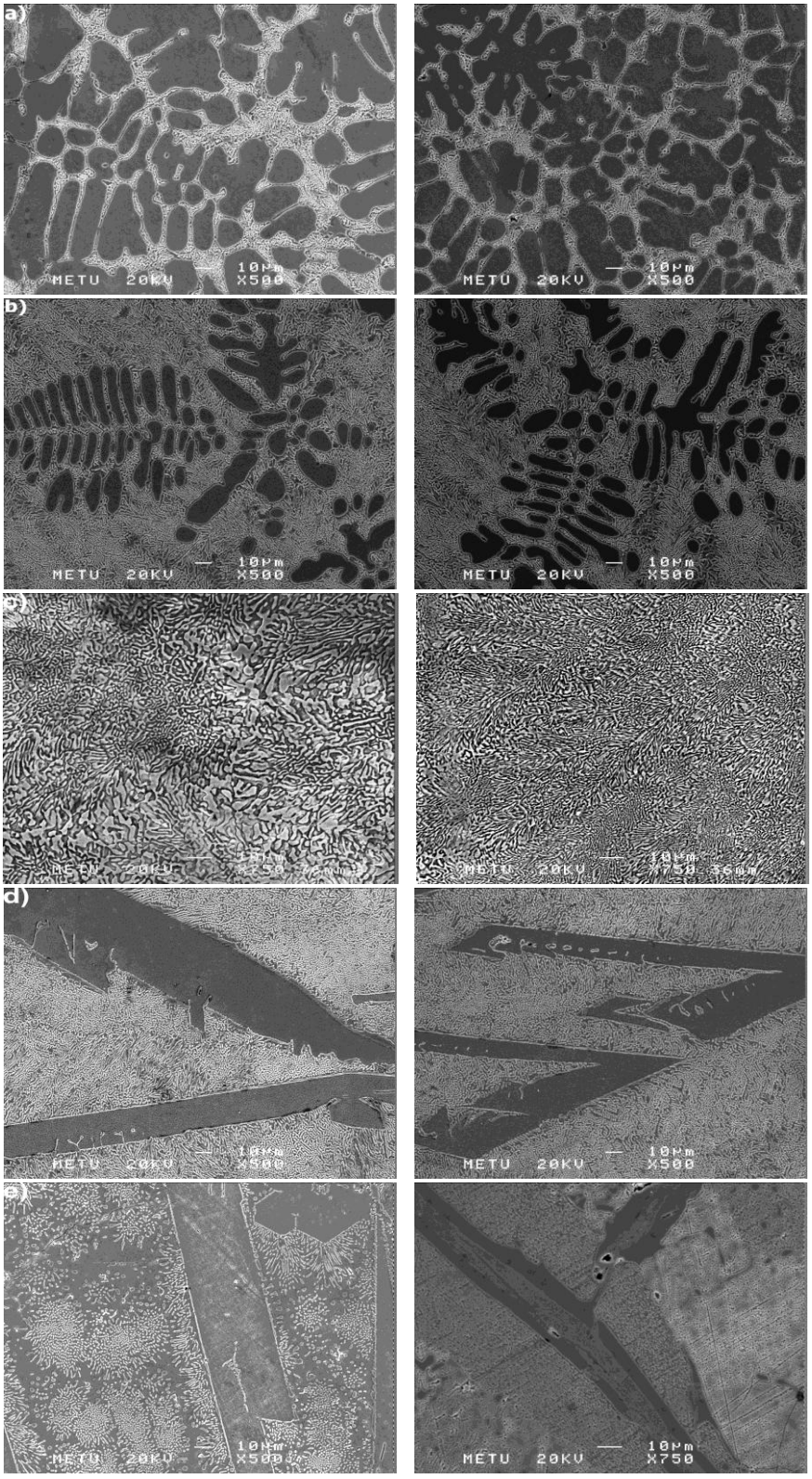

Figure 5.32 SEM micrographs of as-cast and heat-treated $Fe_{50}Al_{50-n}Zr_n$ (right-side) alloys; n = (a) 1, (b) 3, (c) 4, (d) 5 and (e) 7.

Table 5.14 Volume fraction of the eutectic mixture determined from SEM micrographs of as-cast and heat-treated Fe50Al50-nZrn alloys.

Zr content	Volume fraction of eutectic	
	Heat-treated	As-cast
1	28.7	24.6
3	73.5	73.4
4	100	100
5	77.5	72.7
7	77.7	74.3

Thermal analysis measurements of $Fe_{50}Al_{50-n}Zr_n$ alloys reveal that all alloys solidify through a eutectic reaction which takes place at nearly 1287 °C even at 1 at.% Zr addition (Figure 5.34). However, DSC heating curve of heat-treated $Fe_{50}Al_{49}Zr_1$ alloy contains an additional endothermic peak at higher temperature which refers to liquidus of this composition.

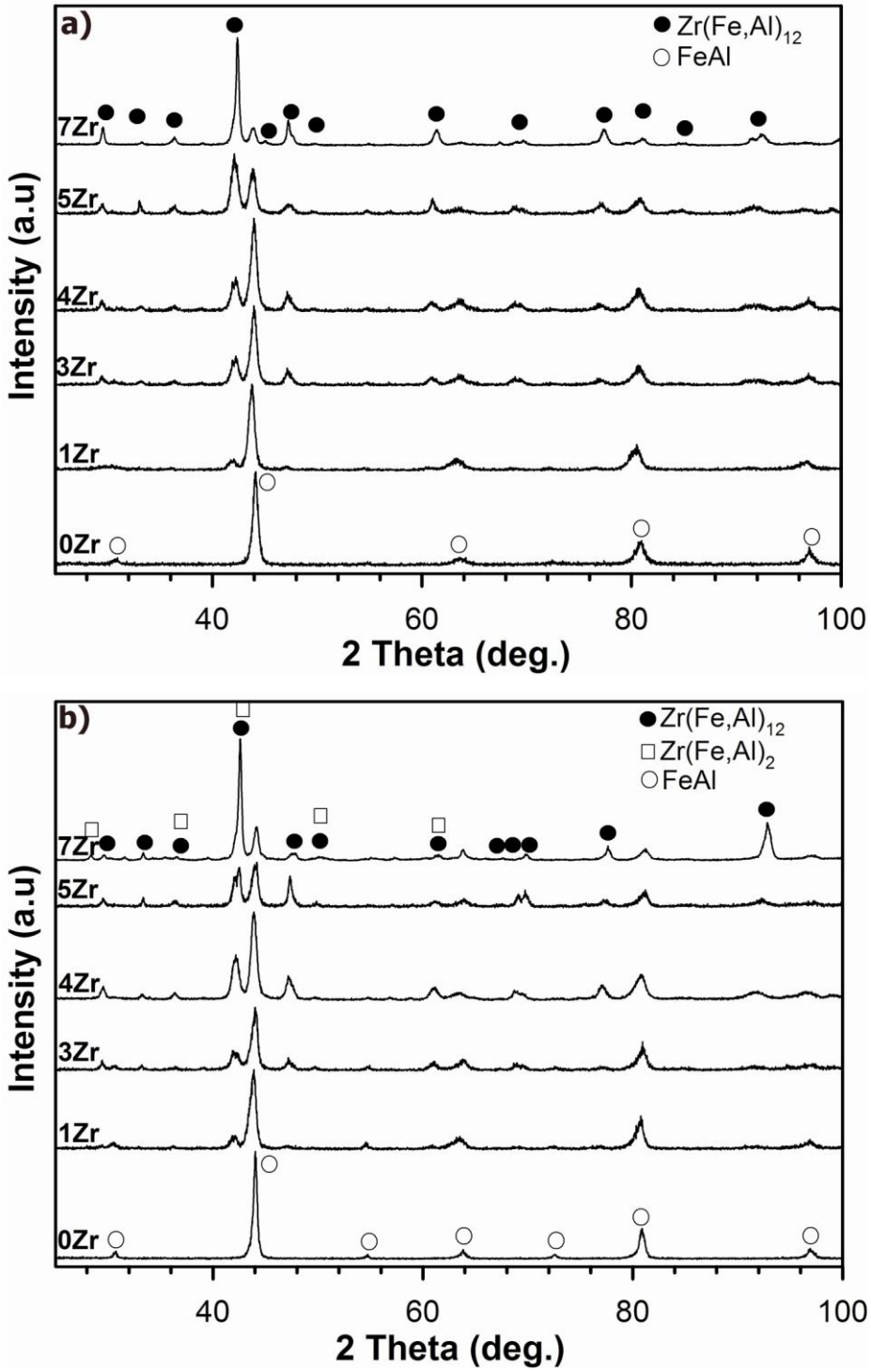

Figure 5.33 XRD patterns of (a) as-cast and (b) heat-treated $Fe_{50}Al_{50-n}Zr_n$ alloys.

Microstructural investigations coupled with EDS analyses (Table 5.15) further clarify that τ_1 Zr(Fe, Al)$_{12}$ phase is the primarily solidified phase of the hypereutectic $Fe_{50}Al_{45}Zr_5$ and $Fe_{50}Al_{43}Zr_7$ compositions. In addition, microstructural examinations also showed that the morphology of the proeutectic primary phases changed from non-faceted to faceted with alteration of primary phase from Fe-Al based phase to ternary intermetallic τ_1 Zr(Fe, Al)$_{12}$ phase. For $Fe_{50}Al_{43}Zr_7$ as-cast alloy, the amount of the τ_1 phase increased and the amount of Fe-Al based phase decreased. However, heat-treatment resulted in the formation of a new ternary intermetallic phase besides τ_1 phase for this composition. This new phase is λ_1 Zr(Fe, Al)$_2$ Laves phase. Three different phases and their elemental analysis results are shown in Figure 5.35. The microstructure indicates that laths of Laves phase is surrounded by Fe-Al based phase and τ_1 phase is distributed in the ternary eutectic.

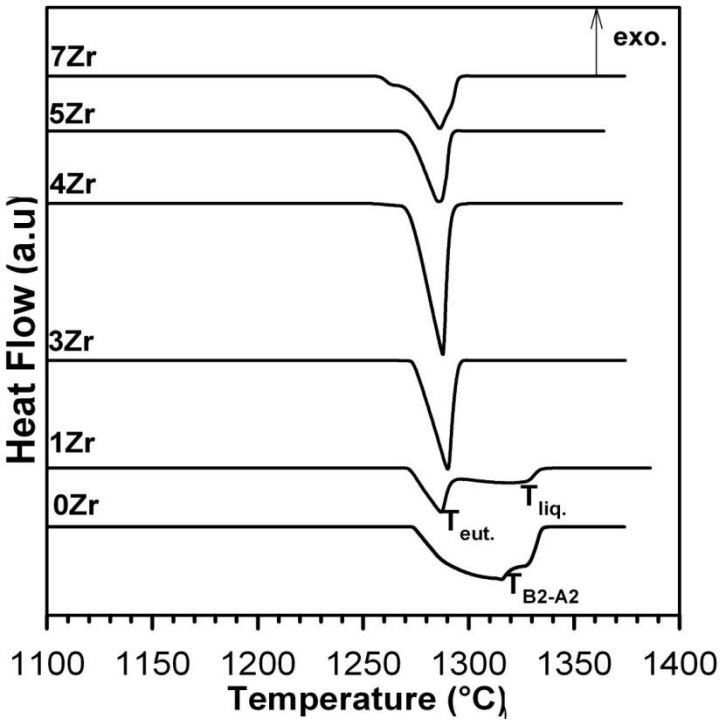

Figure 5.34 DSC heating (at a heating rate of 10K/min) curves of heat-treated $Fe_{50}Al_{50-n}Zr_n$ alloys.

Table 5.15 The results of the EDS analysis of primarily solidified phases of as-cast and heat-treated $Fe_{50}Al_{50-n}Zr_n$ alloys.

Zr content (at.%)	EDS analysis (at.%)					
	As-cast			Heat-treated		
	Fe	Al	Zr	Fe	Al	Zr
1	50.9 ± 0.2	48.9 ± 0.2	0.2 ± 0.1	50.9 ± 0.1	49.0 ± 0.1	0.1 ± 0.1
3	50.4 ± 0.2	49.5 ± 0.2	0.2 ± 0.1	52.9 ± 0.1	46.9 ± 0.2	0.2 ± 0.1
5	43.6 ± 0.9	48.1 ± 0.9	8.1 ± 0.2	41.9 ± 0.1	49.8 ± 0.1	8.9 ± 0.2
7	43.6 ± 0.1	48.0 ± 0.2	8.5 ± 0.2	50.3 ± 2.2	41.0 ± 1.1	9.0 ± 0.5

According to Fe-Al-Zr ternary phase diagram [65], $Fe_{50}Al_{43}Zr_7$ composition is located between the (B2+ τ_1) and (λ_1+ τ_1) two-phase field regions. Moreover, an additional endothermic reaction peak at 1265 °C corresponding to the formation of new phase appears in the DSC curve of heat-treated $Fe_{50}Al_{43}Zr_7$ alloy. Based on the microstructural investigations and thermal analysis measurements, it can be concluded that long heat-treatment results in the degeneration of eutectic and formation of λ_1 $Zr(Fe, Al)_2$ Laves phase.

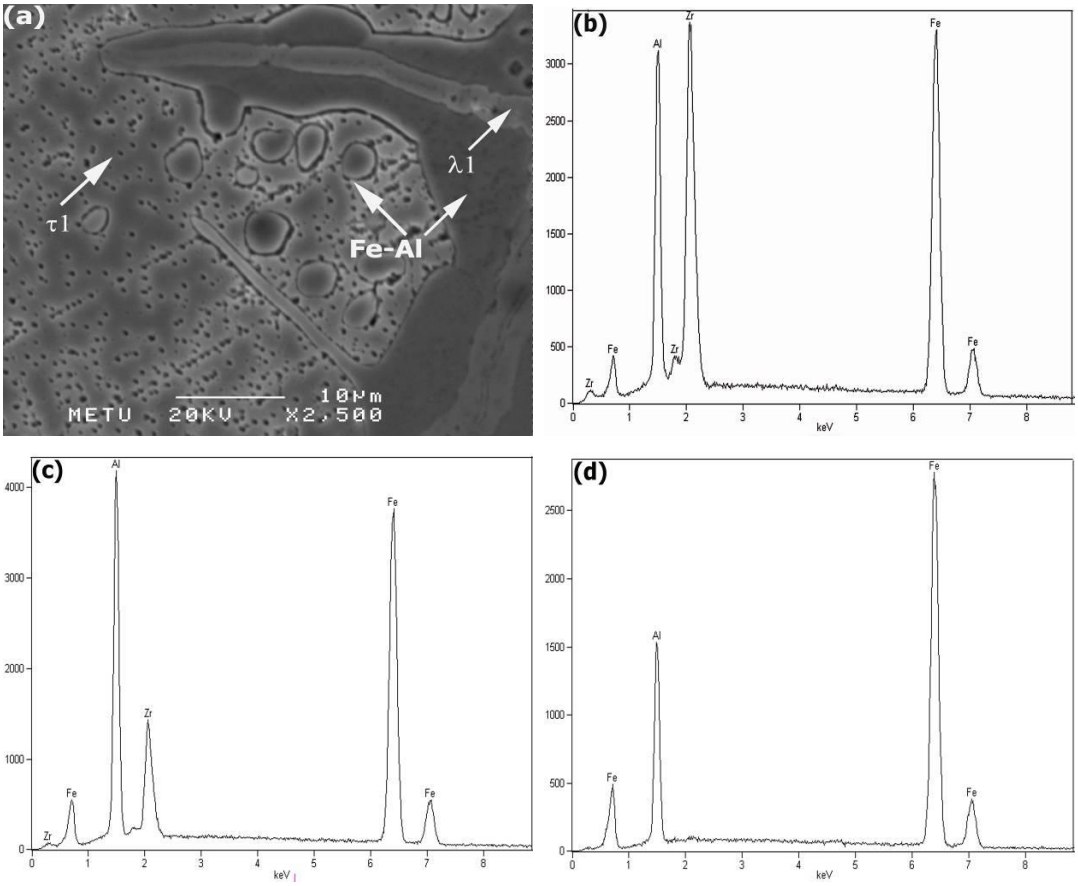

Figure 5.35 (a) High magnification SEM micrograph of heat-treated $Fe_{50}Al_{43}Zr_7$ and EDS analysis of (b) λ_1, (c) τ_1 and (d) Fe-Al based phases.

The amount of Zr dissolved in Fe-Al based dendrites and τ_1 $Zr(Fe, Al)_{12}$ primary phase is nearly 0.2 and 8.5 at.% as determined by the EDS analysis (Table 5.15) for hypo- and hypereutectic compositions, respectively. Determined Zr amounts agree well with the data present in the literature. The solid solubility of Zr in Fe-Al based phases is reported as nearly 0 at.% independent of Al content and temperature [65, 131, 167]. In addition, Raghavan [66] suggested that τ_1 $Zr(Fe, Al)_{12}$ phase contains 7.9-8.5 at.% Zr and 37.4-61.6 at.% Al.

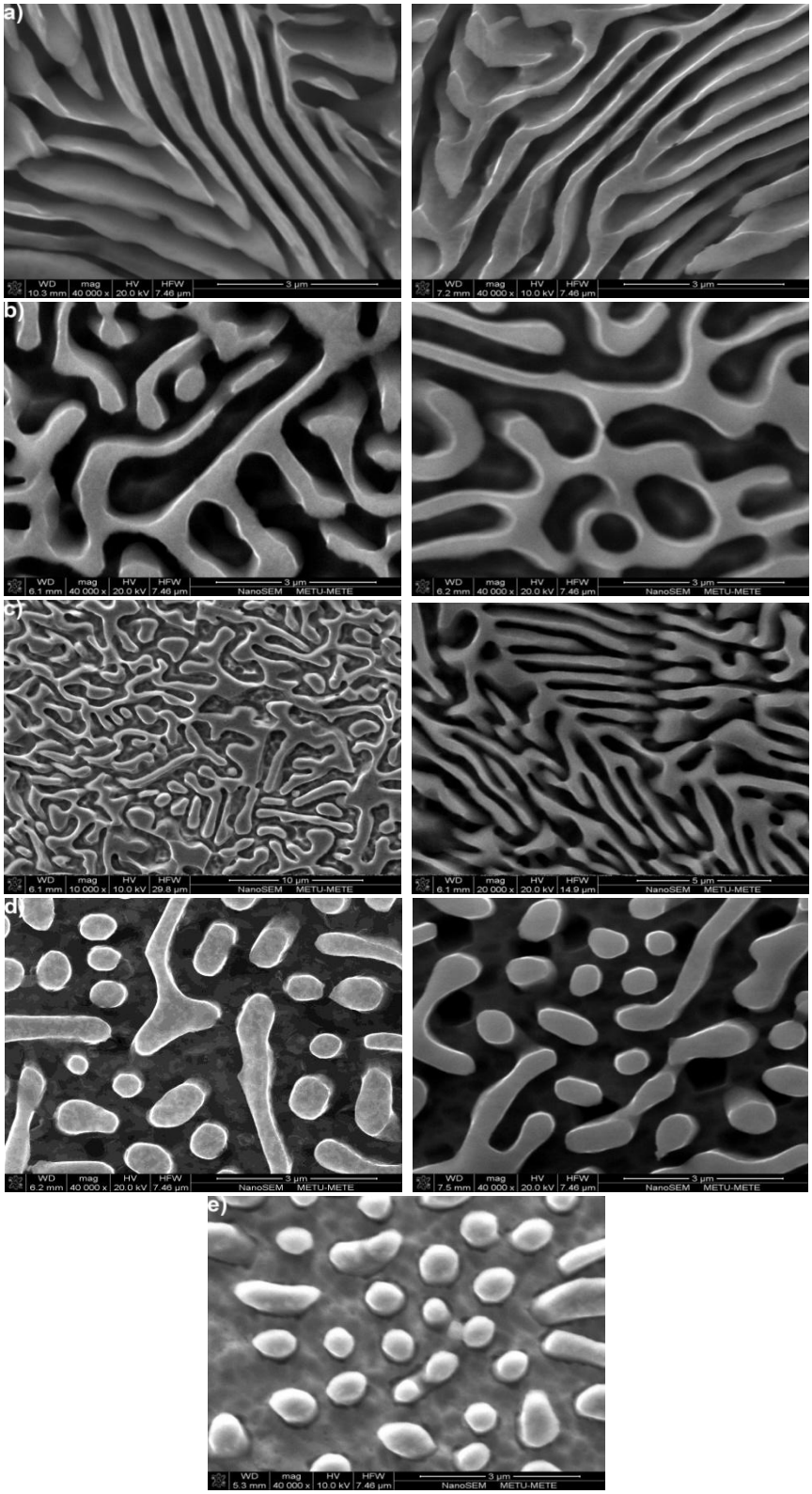

Figure 5.36 High magnification SEM micrographs of as-cast and heat-treated (right side) $Fe_{50}Al_{50-n}Zr_n$ alloys; n = (a) 1, (b) 3, (c) 4, (d) 5 and (e) 7.

Closer inspection of the microstructure by high magnification scanning electron microscopy analyses (Figure 5.36) indicated that hypoeutectic and eutectic alloys display lamellar eutectic structure, whereas ultrafine fibers of Fe-Al based phase has first appeared in the microstructure of hypereutectic $Fe_{50}Al_{45}Zr_5$ alloy. In addition, eutectic structure of hypereutectic $Fe_{50}Al_{43}Zr_7$ alloy is completely composed of ultrafine fibers having average thickness of 659.2 ± 27.0 nm. The mechanism behind lamella to rod transition in eutectic alloys is explained in detail in the preceding section.

High magnification microstructural examinations also revealed that $Fe_{50}Al_{50-n}Zr_n$ alloys do not coarsen after annealing. Both as-cast and heat-treated alloys exhibit similar microstructural features except for 7 at.% Zr containing alloy. Apart from $Fe_{50}Al_{43}Zr_7$ alloy, the size, distribution and morphology of constituent phases do not change with respect to annealing. Only a small decrease in volume fraction of the eutectic phase mixture (Table 5.14) is observed. These findings indicate that $Fe_{50}Al_{50-n}Zr_n$ alloys display high thermal stability which is a significant factor for structural applications at high temperatures [72].

5.4.2 Microhardness Measurements

Moreover, Vickers microhardness measurements (Figure 5.37) have been performed in order to investigate the strengthening effect of ternary intermetallic phases (τ_1 or λ_1) on B2-type ordered FeAl alloys. Mean microhardness value increases gradually with Zr content both in as-cast and heat-treated alloys. Microstructural observations and phase relationships have important effects on strengthening behavior of $Fe_{50}Al_{50-n}Zr_n$ alloys. For hypoeutectic $Fe_{50}Al_{49}Zr_1$ composition, heat-treated alloy has considerably smaller microhardness value than as-cast one. However, the difference between microhardness values of heat-treated and as-cast alloys becomes smaller with increasing Zr content and finally, for hypereutectic compositions, heat-treated alloys have larger microhardness values than as-cast ones.

A similar phenomenon has also been observed for $Fe_{50}Al_{50-n}Hf_n$ alloys. For such alloys, only volume fraction of eutectic mixture changes, while other microstructural features such as size, distribution and morphology of constituent phases do not much change after annealing. Volume fraction of the eutectic mixtures is higher for as-cast alloys, which implies the higher volume fraction of the primary phases of heat-treated alloys. Since the harder ternary intermetallic compounds are primary phases for hypereutectic compositions, annealing has a reverse effect on strengthening of these alloys.

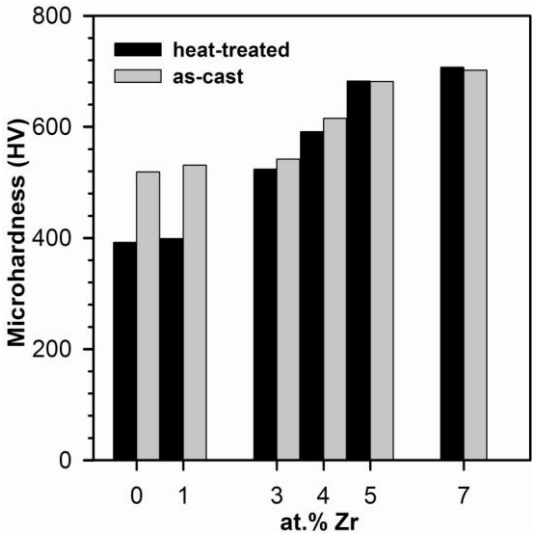

Figure 5.37 Comparison of Vickers microhardness values of as-cast and heat-treated $Fe_{50}Al_{50-n}Zr_n$ alloys.

Compared to other ternary intermetallic compound former elements such as Hf, Nb, Ti and Ta, the effect of Zr on microstructures, phase relationships and strengthening of FeAl is very similar with that of Hf. Among these ternary alloying additions, Zr is the one that having lowest solid solubility in Fe-Al based. This leads to plentiful formation of hard and brittle ternary intermetallic compound even at small amount of Zr additions. Although high volume fraction of ternary intermetallic phase have a positive effect on strengthening Fe-Al based alloys at high temperature, Fe-Al based alloys become more brittle at room temperature. Thus, Zr should be added to Fe-Al based alloys with another ternary alloying addition having large solid solubility such

as Cr, Mn or Ni in order to hinder its detrimental effect on room temperature brittleness.

5.4.3 Magnetic Properties

Phase relationships of studied $Fe_{50}Al_{50-n}Zr_n$ alloys are also investigated by magnetic monitoring. Hysteresis curves, illustrated in Figure 5.38, show that magnetization increases with increasing Zr content and hypereutectic $Fe_{50}Al_{43}Zr_7$ alloy show weak ferromagnetism at room temperature. It is known that τ_1 $Zr(Fe, Al)_{12}$ phase is paramagnetic at room temperature due to its very low Curie temperature of -80 °C [158]. Hence, weak ferromagnetic behaviour at room temperature results from either Fe-Al based phase or λ_1 $Zr(Fe, Al)_2$ Laves phase in the case of heat-treated $Fe_{50}Al_{43}Zr_7$ alloy. Because of the large amount of ternary intermetallic phase formation, the Al content in the Fe-Al based phase decreases drastically with Zr content and Fe-Al based phase can show ferromagnetism. On the other hand, λ_1 $Zr(Fe, Al)_2$ Laves phase is also ferromagnetic phase and it has a strong contribution to the room temperature ferromagnetism of heat-treated $Fe_{50}Al_{43}Zr_7$ alloy.

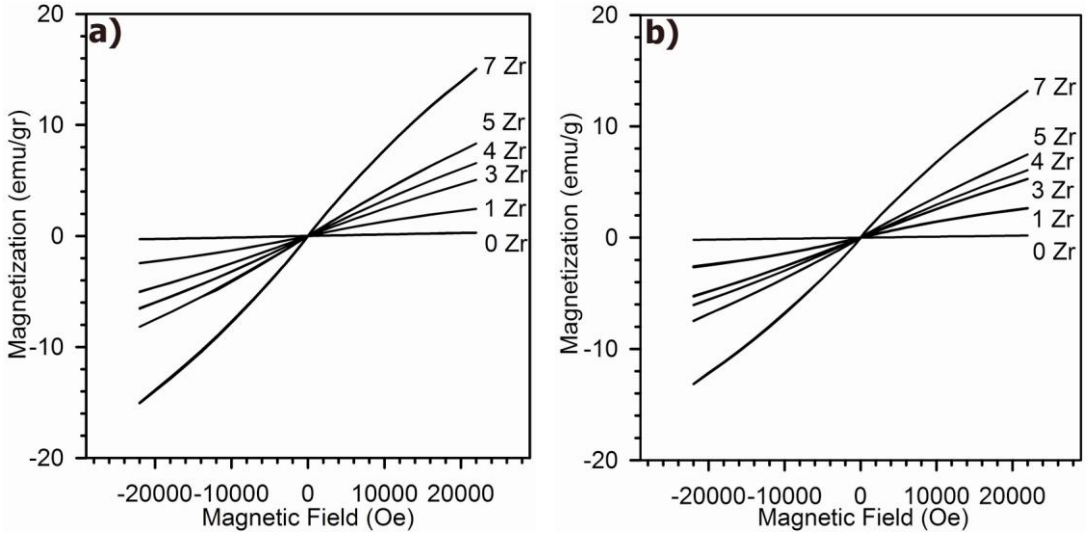

Figure 5.38 Room temperature hysteresis curves of $Fe_{50}Al_{50-n}Zr_n$ alloys (a) as-cast and (b) heat-treated.

5.4.4 Kinetic Analyses of Eutectic Phase Transitions

Reaction enthalpies of the eutectic phase transitions present in the DSC curves (Figure 5.34) of ternary $Fe_{50}Al_{50-n}Zr_n$ alloys are calculated based on integrated peak area method and listed in Table 5.16. It is important to note that there is a strong correlation between calculated reaction enthalpies and structures observed in microstructural and XRD analyses of ternary alloys. Enthalpies of the eutectic reactions increase with increasing Zr content and reach its maximum value at eutectic composition of $Fe_{50}Al_{46}Zr_4$ and then they begin to decrease.

Table 5.16 Estimated enthalpies of eutectic phase transitions present in DSC curves of the heat-treated $Fe_{50}Al_{50-n}Zr_n$ alloys.

Zr content	$\Delta H_{eut.}$ (J/g)
1	60.97
3	222.16
4	236.55
5	106.16
7	100.28

The activation energies of the eutectic phase transitions of ternary $Fe_{50}Al_{50-n}Zr_n$ alloys were also calculated with well-known Kissinger [165] and Ozawa [166] methods given as Eqs.(5.1) and Eqs.(5.2), respectively. Three different heating rates of 10, 20 and 30 °C/min were applied to samples and activation energies were calculated from the slopes of the plots (Figure 5.39). The lowest and highest activation energies were calculated as 2961.5 kJ/mol and 9081.1 kJ/mol for $Fe_{50}Al_{45}Zr_5$ and $Fe_{50}Al_{43}Zr_7$ alloys, respectively (Table 5.17).

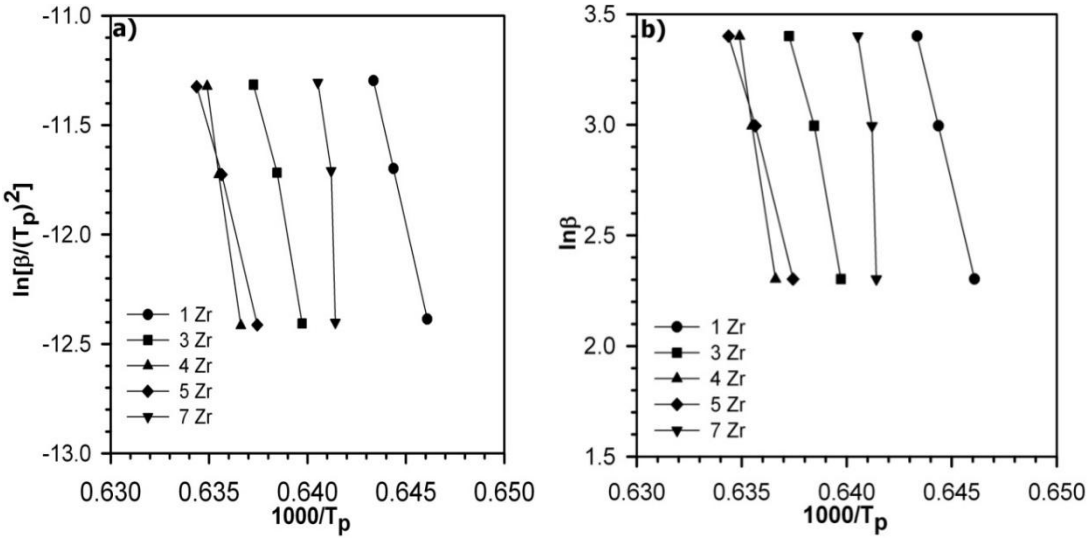

Figure 5.39 (a) The Kissinger and (b) Ozawa plots of eutectic reactions present in DSC curves of heat-treated $Fe_{50}Al_{50-n}Zr_n$ alloys.

Table 5.17 Calculated activation energies of eutectic reactions present in DSC curves of heat-treated $Fe_{50}Al_{50-n}Zr_n$ alloys according to the Kissinger and Ozawa methods (r is the linearity coefficient).

Zr content	Kissinger		Ozawa	
	E_a(kJ/mol)	$\|r\|$	E_a(kJ/mol)	$\|r\|$
1	3319.2	1.0000	3179.7	1.0000
3	3676.4	0.9911	3519.4	0.9913
4	5276.3	0.9706	5040.7	0.9708
5	2961.5	0.9987	2839.9	0.9987
7	9081.1	0.9026	9013.7	0.9031

5.4.5 Conclusions

Microstructures, phase relationships, magnetic properties and microhardness values of $Fe_{50}Al_{50-n}Zr_n$ alloys (n=1, 3, 4, 5 and 7 at.%) have been investigated. Due to the limited solid solubility of Zr in FeAl, the ternary intermetallic τ_1 $Zr(Fe, Al)_{12}$ phase is

found to form even at 1 at.% Zr addition. This phase develops a eutectic phase mixture with the Fe-Al based phase at all investigated compositions and its volume fraction increases with increasing Zr content. However, λ_1 Zr(Fe, Al)$_2$ Laves phase is formed besides τ_1 Zr(Fe, Al)$_{12}$ phase after heat-treatment for $Fe_{50}Al_{43}Zr_7$ alloy. The Zr concentration of the Fe-Al based phase and the eutectic composition is found to be 0.2 and 4 at.%, respectively. Eutectic reaction temperature is determined as 1287 °C from the DSC measurements. Magnetic behavior of the ternary alloys at room temperature changes from paramagnetism to weak ferromagnetism with increasing Zr content. The weak ferromagnetism observed at room temperature is attributed to either the reduction in the amount of Al in the Fe-Al based phase with increasing amount of Zr(Fe, Al)$_{12}$ or formation of λ_1 Zr(Fe, Al)$_2$ Laves phase in the case of heat-treated $Fe_{50}Al_{43}Zr_7$ alloy. Lastly, the amount of Zr is found to have a profound effect on microhardness of the $Fe_{50}Al_{50-n}Zr_n$ alloys.

CHAPTER 6

EFFECT OF TERNARY ALLOYING ADDITIONS ON OXIDATION BEHAVIOR OF $Fe_{50}Al_{50-n}X_n$ ALLOYS

The cyclic oxidation curves for binary heat-treated FeAl intermetallic compound are given in Figure 6.1, showing the mass gain versus time at 800 and 900 °C. FeAl intermetallic compound exhibits excellent cyclic oxidation resistance up to 500 hours without any spallation of oxides. Mass gain has initially linear curves at both temperatures indicating the rapid growth of metastable and other modifications of alumina.

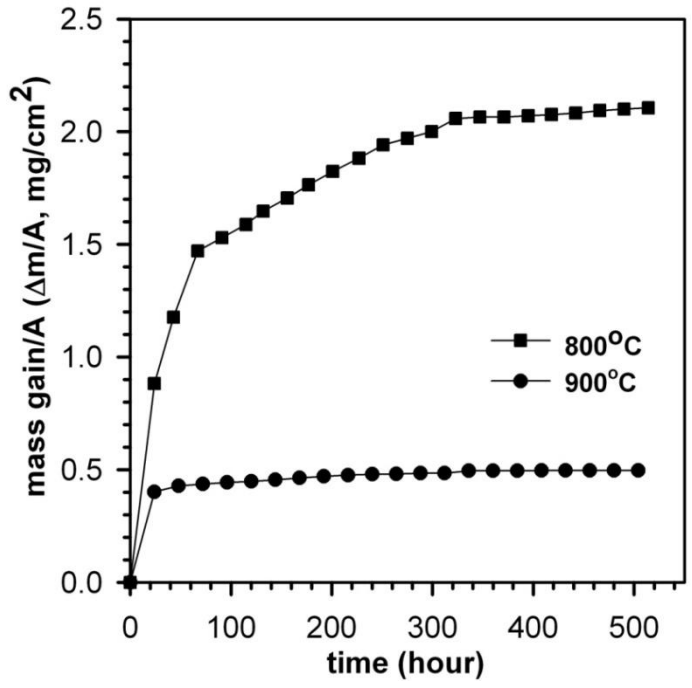

Figure 6.1 Mass gain versus time curves for cyclic oxidation of binary heat-treated FeAl intermetallic compound.

Metastable modifications transform to stable, protective and slow growing α-Al_2O_3 after some cycles and curves exhibit parabolic behaviour. Moreover, most of the mass gains are occurred at the first three cycles showing that the stable α-Al_2O_3 formation takes place fast. The mass gain rate of binary FeAl decreases with increasing temperature from 800 °C to 900 °C due to the accelerated transformation from metastable to stable, protective alumina with increasing temperature.

XRD patterns (Figure 6.2) of binary FeAl samples oxidised at 800 and 900 °C indicates the formation of nearly pure α-Al_2O_3 scale. It is important to note that small peaks corresponding to the metastable alumina reveal the presence of θ-Al_2O_3 at small amounts. Substrate, FeAl, peaks indicate the small oxide scale thickness for both investigated temperatures.

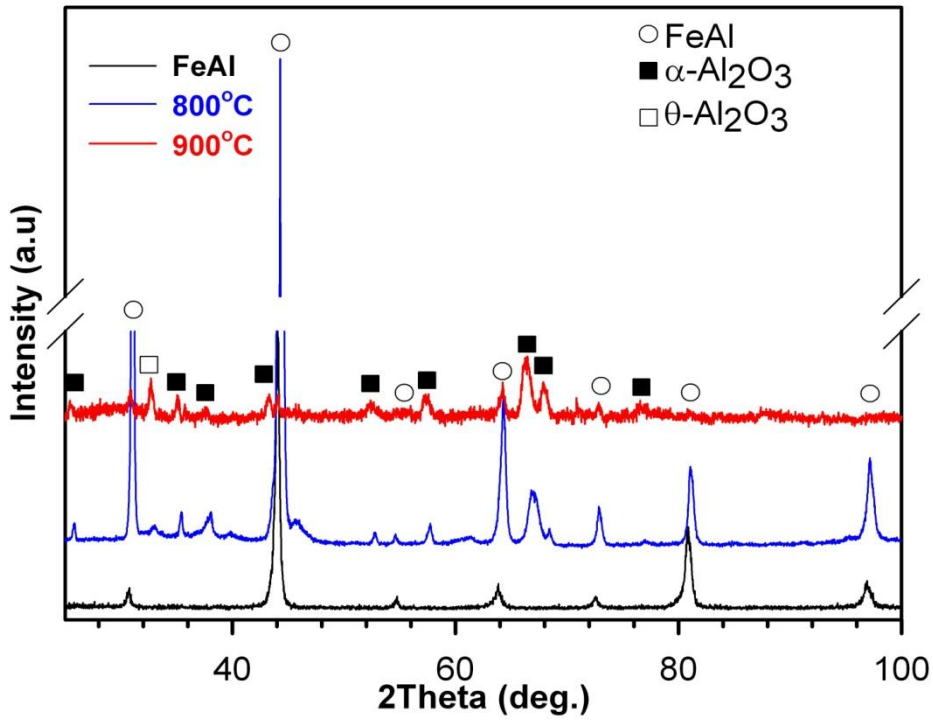

Figure 6.2 XRD patterns of FeAl intermetallic compound and oxidised FeAl samples at 800 and 900 °C.

Oxide scale morphologies of the binary FeAl samples are illustrated in Figure 6.3. SEM investigations of oxidised sample at 800 °C (Figure 6.3(a) and (b)) reveal the formation of homogenous, continuous and even oxide scale without any voids and cracks. The oxide morphology is nodular. Moreover, the results of EDS analysis (Figure 6.4(a)) indicated the nodule oxides are Al_2O_3.

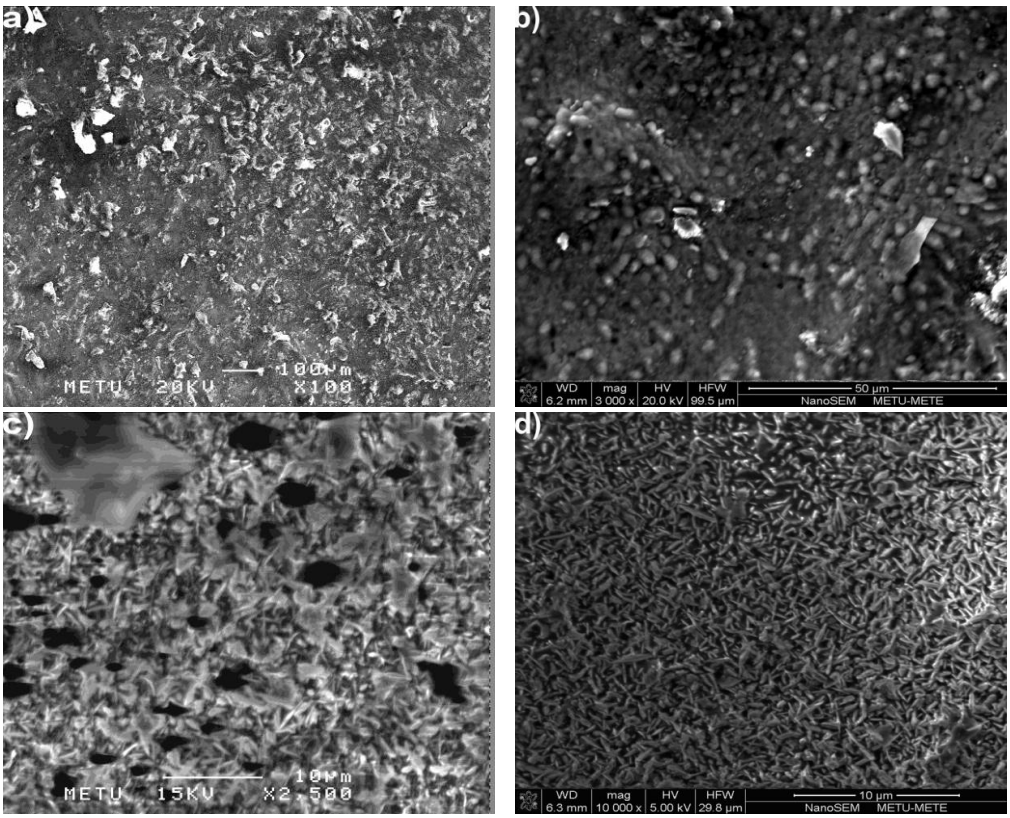

Figure 6.3 SEM micrographs showing the surface scale morphology of FeAl samples after oxidation at (a), (b) 800 and (c), (d) 900 °C.

However, oxide scale morphology altered with increasing the oxidation temperature from 800 to 900 °C. In this case, homogenous, continuous and even oxide scale is present with isolated dark zones. According to SEM observations (Figure 6.3(c)), oxide scale contains large zones covered by alumina plates and small dark zones having irregular size of 4 μm. The plate-like oxide scales correspond to the θ-Al_2O_3 which was also detected by XRD analyses, whereas dark zones were (Fe, Al)-oxides enriched in Fe according to EDS elemental analysis (Figure 6.4(c)).

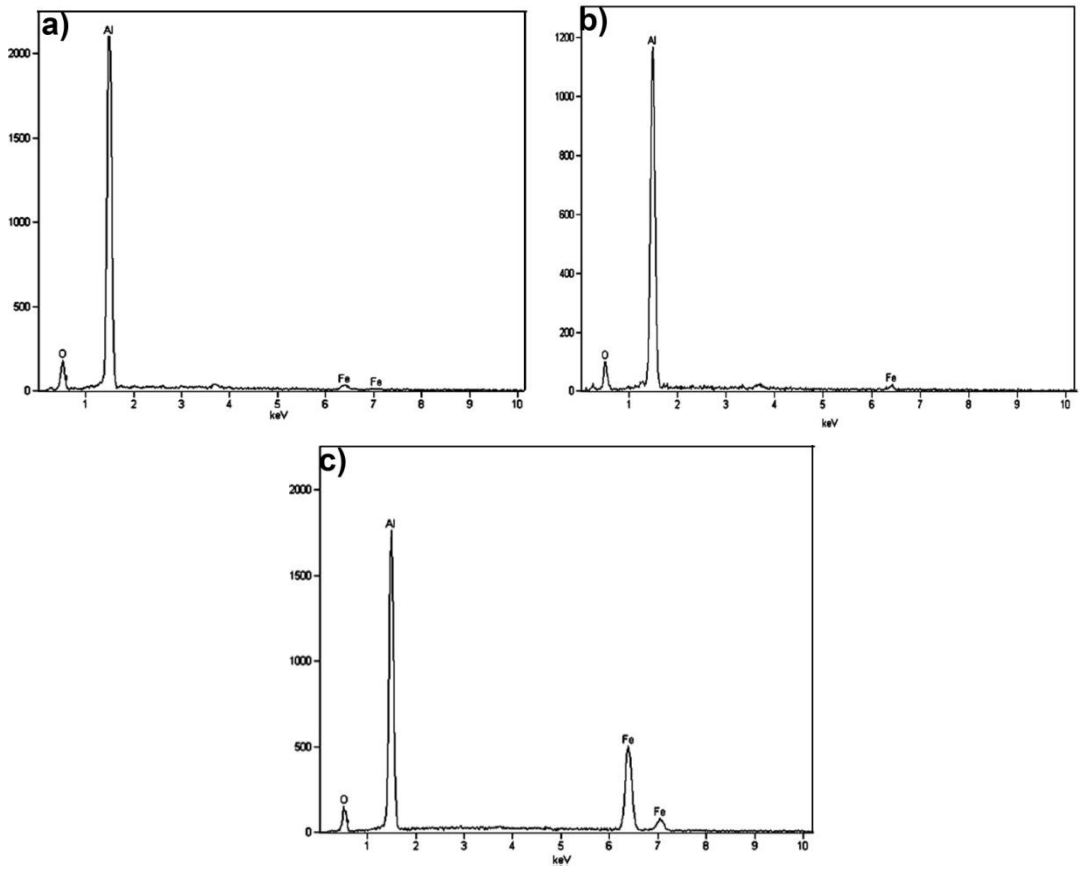

Figure 6.4 EDS elemental analyses of FeAl samples after oxidation at (a) 800 °C, (b) 900 °C (plate-like oxides) and (c) 900 °C (small dark zones).

6.1 B Addition

6.1.1 Structural Properties

Solidification microstructures of all as-cast and heat-treated $Fe_{50}Al_{50-n}B_n$ alloys (Figure 6.5) consist of primary Fe-Al based dendrites and interdendritic regions. All as-cast alloys exhibit dendritically solidified FeAl based matrix and FeAl-FeB eutectics. Volume fraction of the eutectic mixture increases with increasing B content. FeAl and FeB phases are recognized as constituents of investigated alloys by the XRD analyses (Figure 6.6). However, microstructures of as-cast alloys significantly changed after annealing. FeAl-FeB eutectic mixture coarsened and spheroidised FeB particles formed.

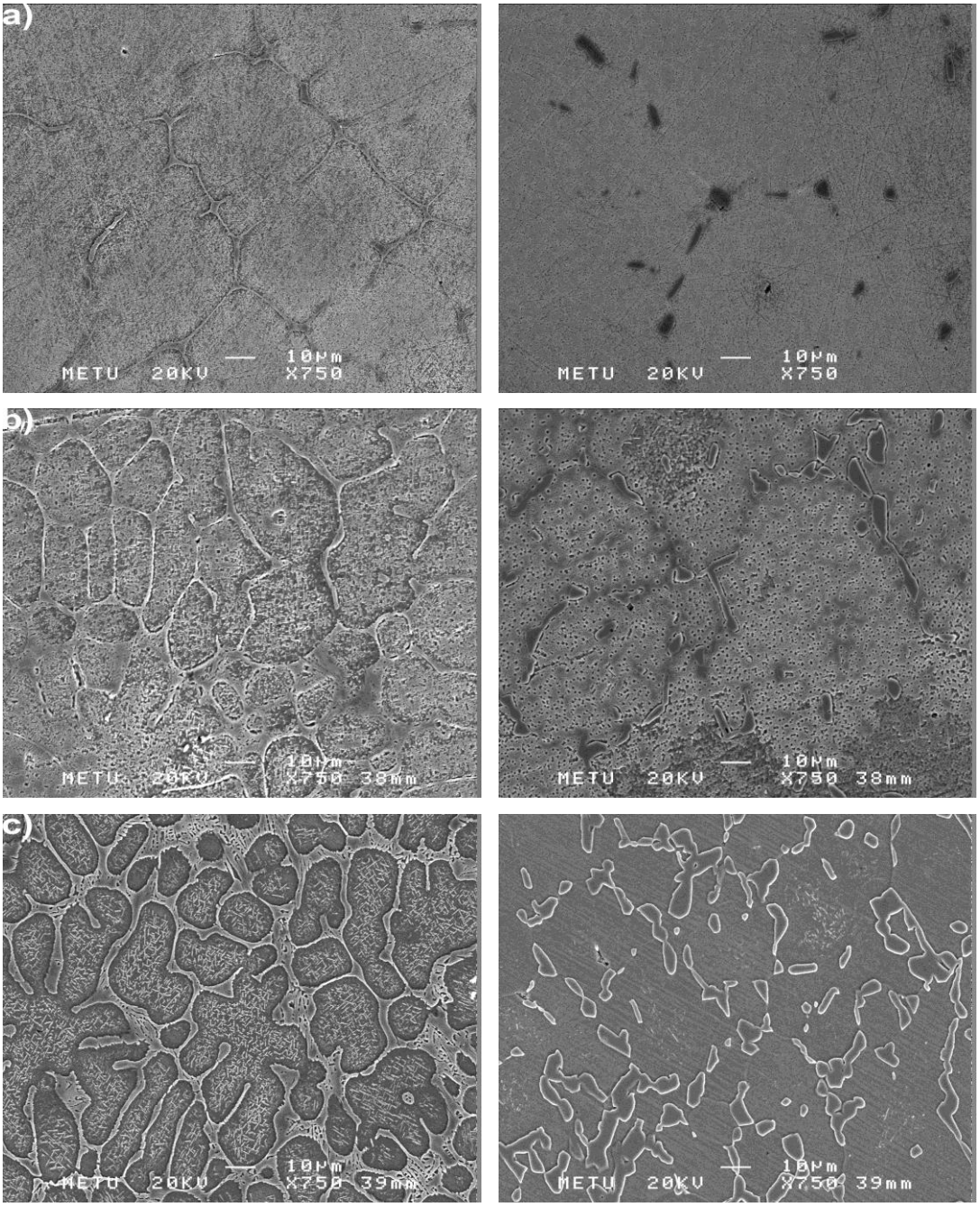

Figure 6.5 SEM micrographs of as-cast and heat-treated $Fe_{50}Al_{50-n}B_n$ (right-side) alloys; n = (a) 1, (b) 3, and (c) 5.

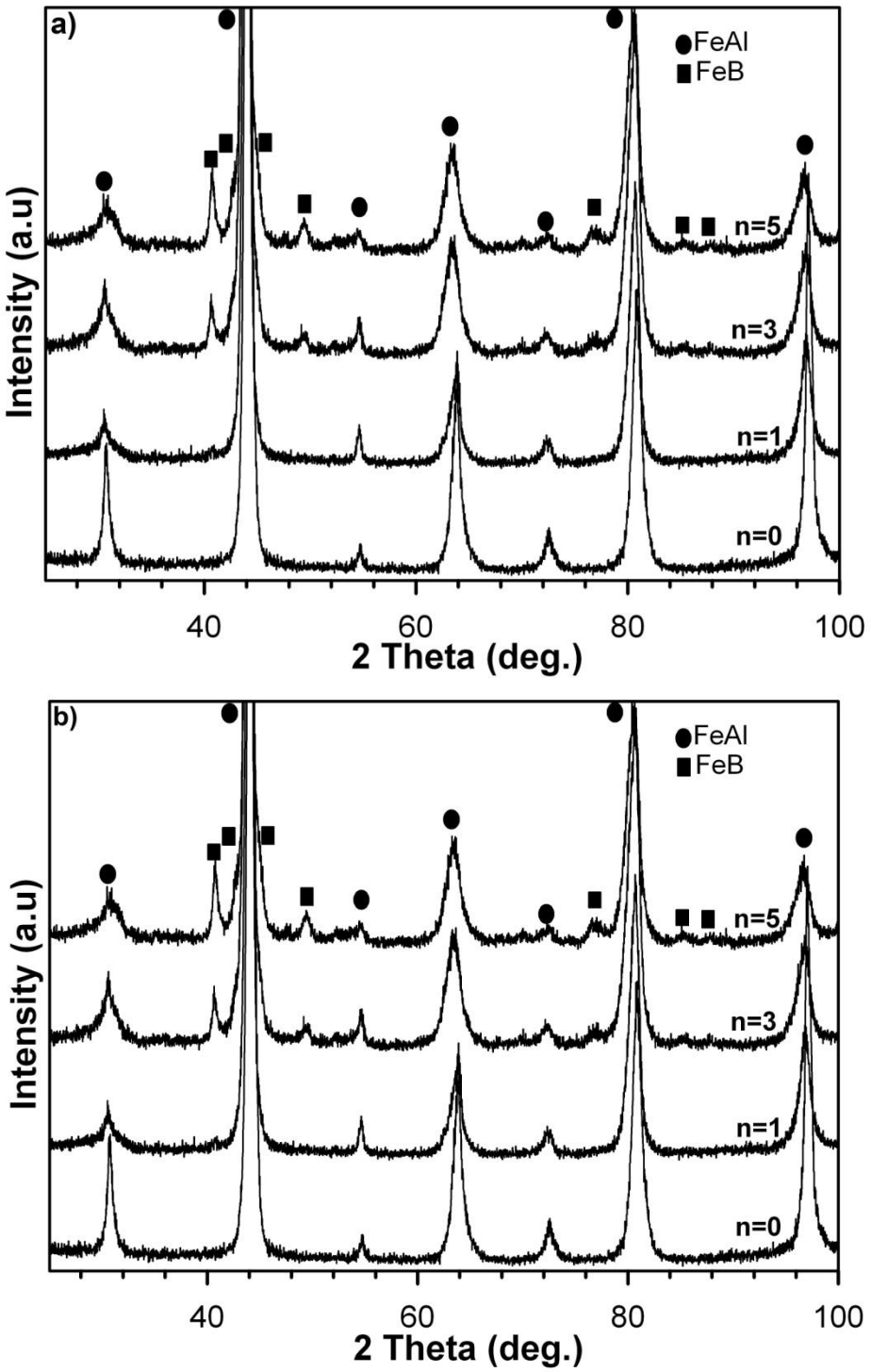

Figure 6.6 XRD patterns of (a) as-cast and (b) heat-treated $Fe_{50}Al_{50-n}B_n$ alloys.

DSC heating curves of heat-treated $Fe_{50}Al_{50-n}B_n$ alloys, given in Figure 6.7, contains two endothermic reaction peaks. The narrow peak at 1180 °C refers to eutectic phase transition, while the broader one at higher temperature pertains to liquidus. Additionally the liquidus temperature decreases with increasing B content.

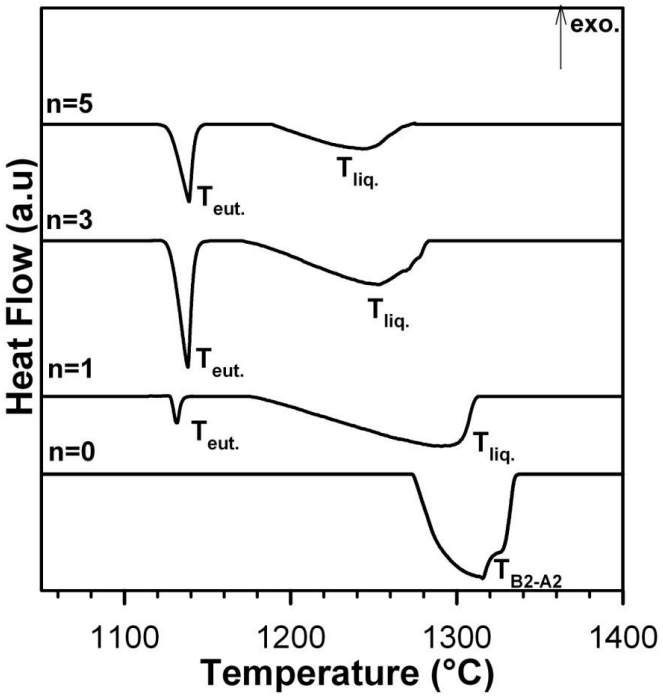

Figure 6.7 DSC heating (at a heating rate of 10K/min) curves of heat-treated $Fe_{50}Al_{50-n}B_n$ alloys.

6.1.2 Cyclic Oxidation Tests

The cyclic oxidation curves for heat-treated $Fe_{50}Al_{50-n}B_n$ samples oxidised at 900 °C are given in Figure 6.8. No scale spallation was observed for all investigated compositions. All samples exhibit an initially linear curve with steep rise in the first two cycles as an indication of the rapid growth of metastable and other forms of alumina. Most of the mass gains are occurred in these two cycles. Then, curves reach plateu-like region after transformation of metastable forms of alumina to stable, protective and adherent α-Al_2O_3. Fast formation of stable α-Al_2O_3 scale (after 3-4 cycles) is a big advantage of $Fe_{50}Al_{50-n}B_n$ samples.

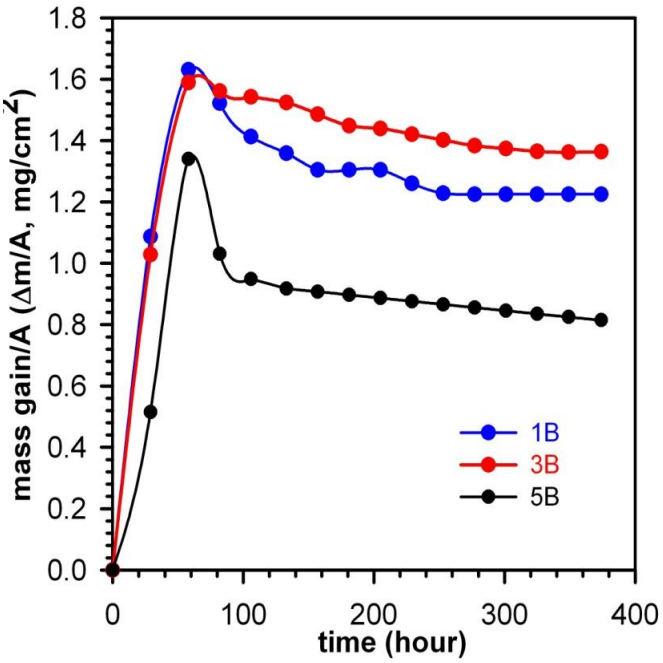

Figure 6.8 Mass gain versus time curves for cyclic oxidation tests of heat-treated $Fe_{50}Al_{50-n}B_n$ samples oxidised at 900 °C.

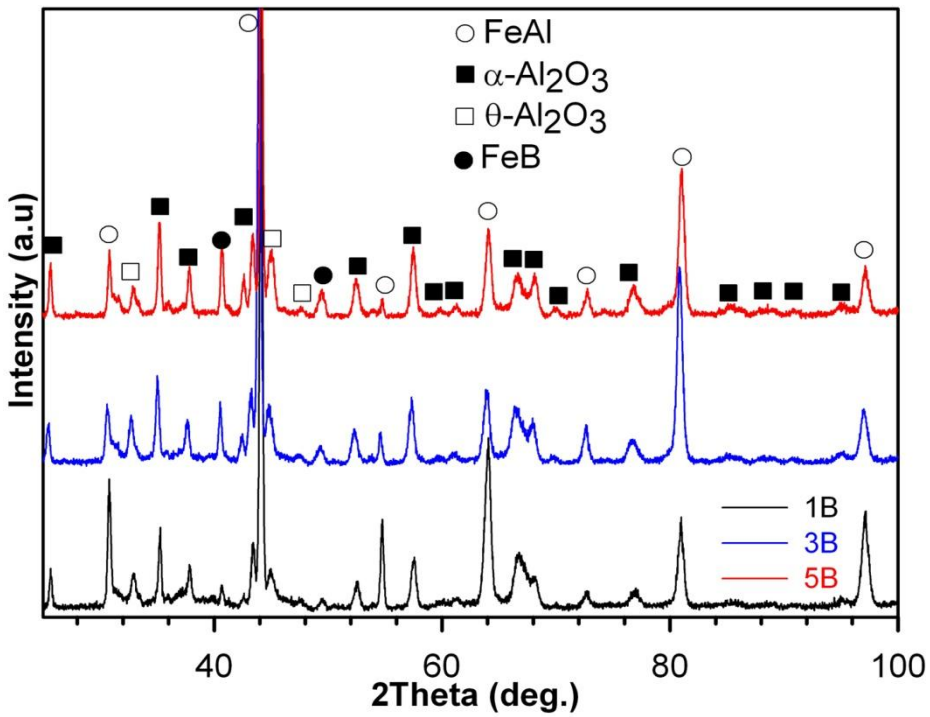

Figure 6.9 XRD patterns of heat-treated $Fe_{50}Al_{50-n}B_n$ samples oxidised at 900 °C.

XRD patterns of heat-treated $Fe_{50}Al_{50-n}B_n$ samples oxidised at 900 °C reveals that oxide scale is composed of mainly stable α-Al_2O_3 and small amount of metastable θ-Al_2O_3. The diffraction lines corresponding to the substrate FeAl-FeB indicates that oxide scale is very thin.

Oxide scale morphology of the samples has been examined by SEM analyses (Figure 6.10). All samples contain homogenous, continuous and even oxide scale without formation of any voids or cracks. Scale morphology is mainly nodular. It is assumed that the nodule oxides are stable α-Al_2O_3, whereas plate-like particles with small amount corresponds to metastable θ- Al_2O_3.

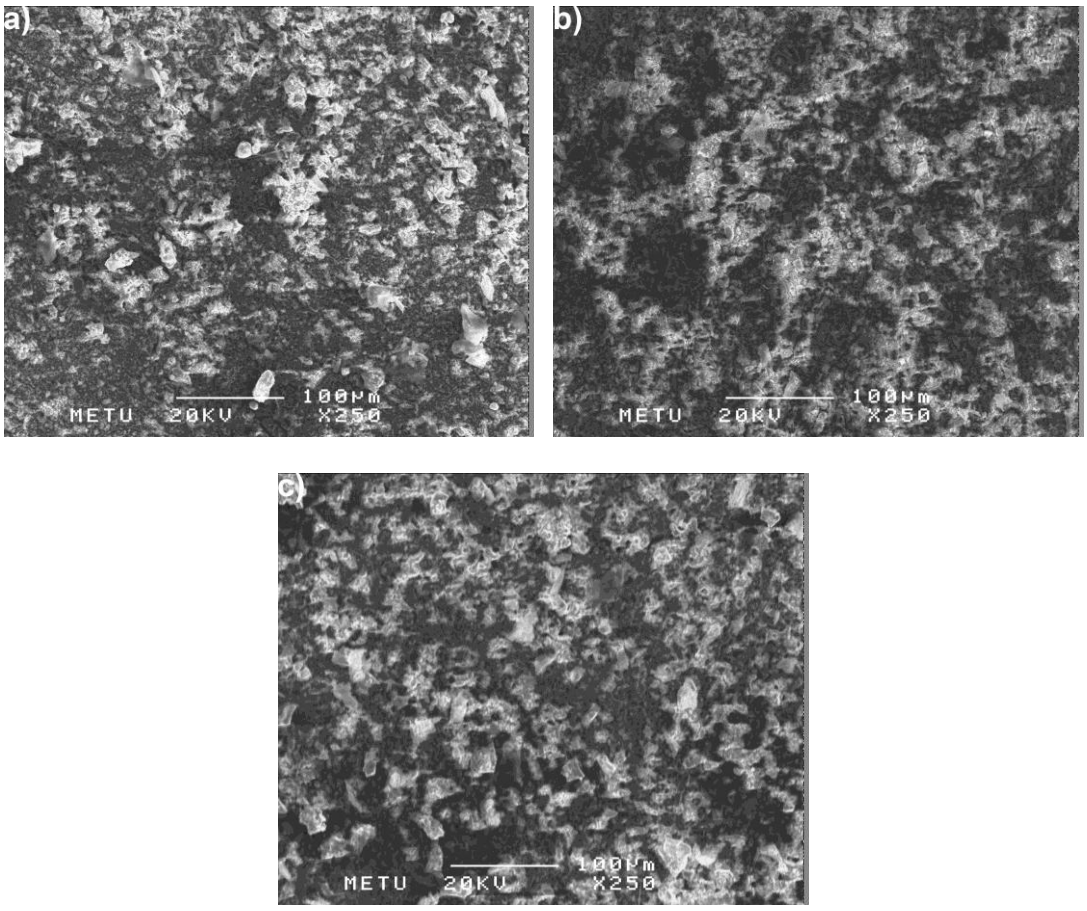

Figure 6.10 SEM micrographs of heat-treated $Fe_{50}Al_{50-n}B_n$ samples after oxidation at 900 °C n= (a) 1, (b) 3 and (c) 5.

6.1.3 Conclusions

Structural properties and oxidation behavior of $Fe_{50}Al_{50-n}B_n$ alloys (n = 1, 3 and 5 at.%) have been investigated. FeB phase forms even at 1 at.% B addition because of the incomplete solid solubility of B in FeAl phase. FeB phase makes a eutectic phase mixture with FeAl at all investigated compositions and its volume fraction increases with increasing B content. FeAl-FeB eutectic mixture coarsened and spheroidised FeB particles formed after annealing. Eutectic reaction temperature is determined as 1180 °C from the DSC measurements.

The cyclic oxidation tests performed at 900 °C showed that stable, protective and adherent α-Al_2O_3 scale forms without formation of any voids and cracks. No scale spallation was observed. The presence of substrate peaks in XRD patterns indicates the very thin oxide scale.

6.2 Ti Addition

6.2.1 Structural Properties

Solidification microstructures of all investigated $Fe_{50}Al_{50-n}Ti_n$ alloys are presented in Figure 6.11. Microstructures of as-cast and heat-treated $Fe_{50}Al_{50-n}Ti_n$ alloys with n=1, 3 and 5 at.% is composed of FeAl based grains and white precipitates at grain boundaries. Compared to microstructure of binary stoichiometric FeAl (Figure 4.1(a)), Ti addition led to significant grain refinement.

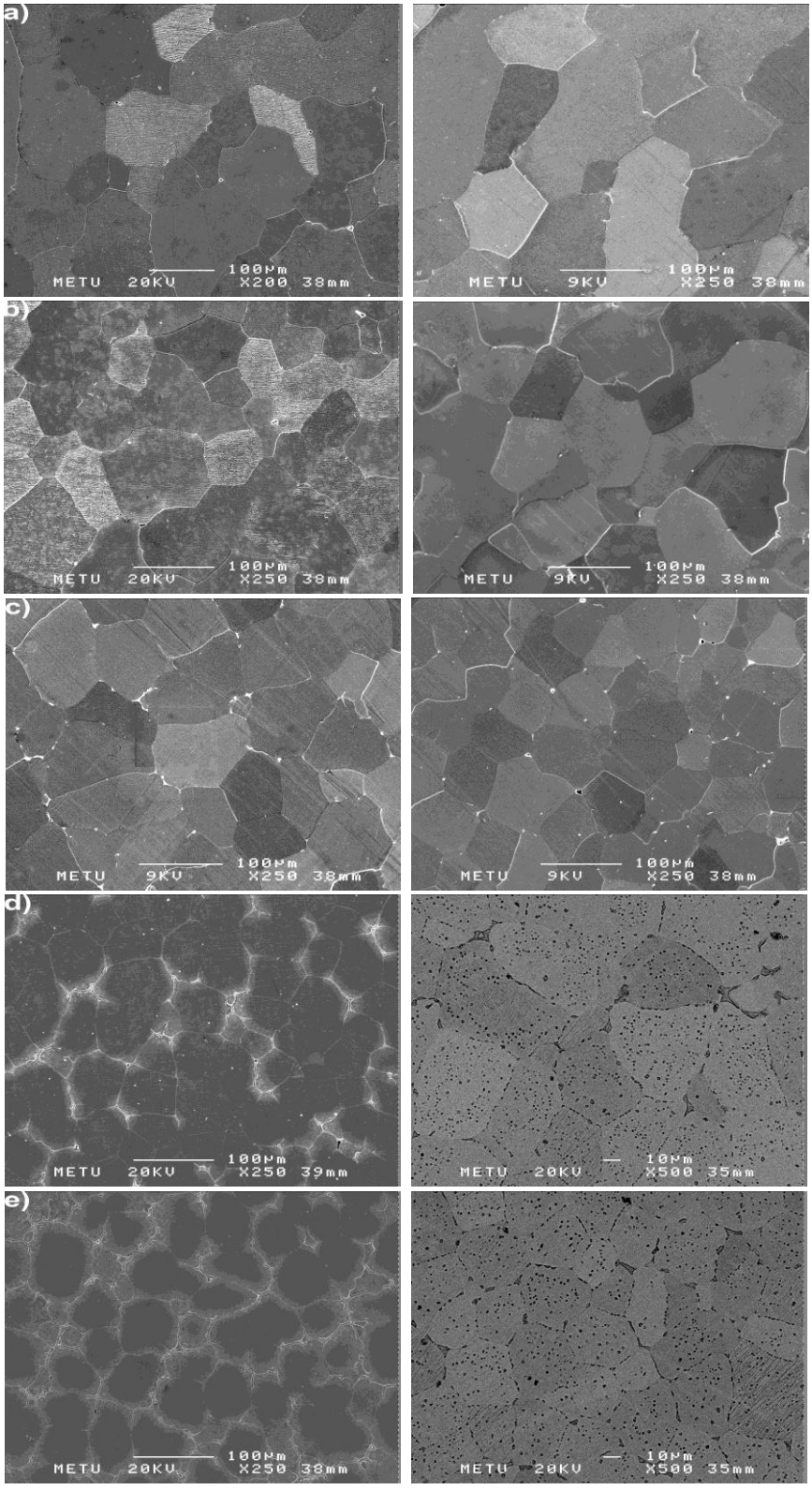

Figure 6.11 SEM micrographs of as-cast and heat-treated $Fe_{50}Al_{50-n}Ti_n$ (right-side) alloys; n = (a) 1, (b) 3, (c) 5, (d) 7 and (e) 9.

When Ti amount is increased to 7 or 9 at.%, volume fraction of second phase particles increased significantly and covered the grain boundaries as a hard skeleton. However, annealing resulted in important changes to microstructures of as –cast $Fe_{50}Al_{43}Ti_7$ and $Fe_{50}Al_{41}Ti_9$ alloys (Figures 6.11 (a) and (b)). Similar to microstructures of $Fe_{50}Al_{43}Mo_7$ and $Fe_{50}Al_{41}Mo_9$ alloys, extra second phase particles precipitated within grains formed and existing particles grew.

These second phase particles are identified as Al_2FeTi (τ_2) phase by XRD (Figure 6.12) and EDS (Figure 6.13) analyses. Solid solubility behaviour of Ti in Fe-Al based alloys have been explained in detail in previous chapters. Ti has a limited but sufficient solid solubility in B2-type ordered FeAl intermetallic compound. According to Al-Fe-Ti isothermal section at 800 °C [168], $Fe_{50}Al_{50-n}Ti_n$ alloys containing less than 7 at.% Ti lie in the B2 phase region, whereas 7 or 9 at.% Ti containing alloys lie in the (B2+ τ_2) two phase field.

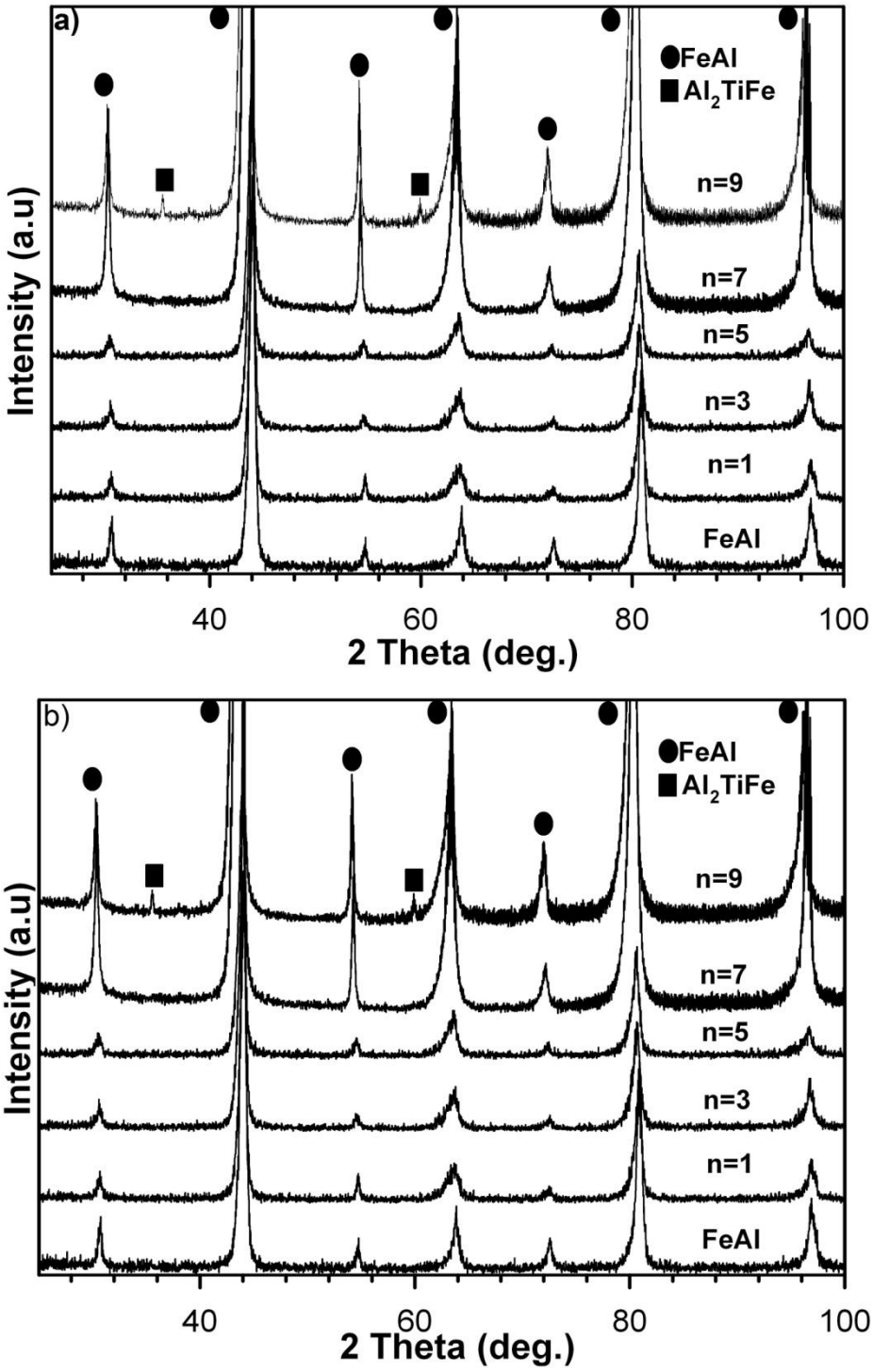

Figure 6.12 XRD patterns of (a) as-cast and (b) heat-treated $Fe_{50}Al_{50-n}Ti_n$ alloys.

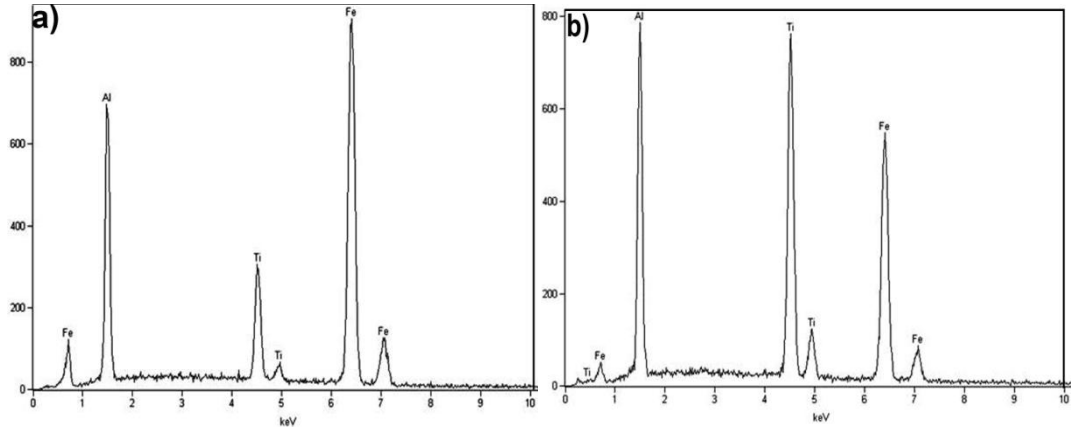

Figure 6.13 EDS analysis of heat-treated $Fe_{50}Al_{41}Ti_9$ alloy, (a) Fe-Al based matrix phase and (b) Al_2FeTi (τ_2) phase.

DSC heating curves of heat-treated $Fe_{50}Al_{50-n}Ti_n$ alloys are shown in Figure 6.14. B2↔A2 order-disorder transition temperature has a decreasing tendency with Ti content. This decrease becomes more pronounced for 9 at.% Ti addition because of the relatively higher volume fraction of ternary intermetallic Al_2FeTi (τ_2) phase. The Al content in the Fe-Al based matrix phase decreases considerably as the amount of second phase increases and thus order-disorder transition temperature decreases. Moreover, solidus and liquidus temperatures of heat-treated $Fe_{50}Al_{50-n}Ti_n$ alloys decrease with increasing Ti content (Table 6.1).

Table 6.1 Experimentally measured order-disorder transition, solidus and liquidus temperatures of heat-treated $Fe_{50}Al_{50-n}Ti_n$ alloys.

at.% Ti	T^{B2-A2} (°C)	$T^{sol.}$ (°C)	$T^{liq.}$ (°C)
0	1316	1270	1325
1	1313	1268	1324
3	1312	1243	1314
5	1302	1233	1310
7	1296	1230	1303
9	1248	1190	1284

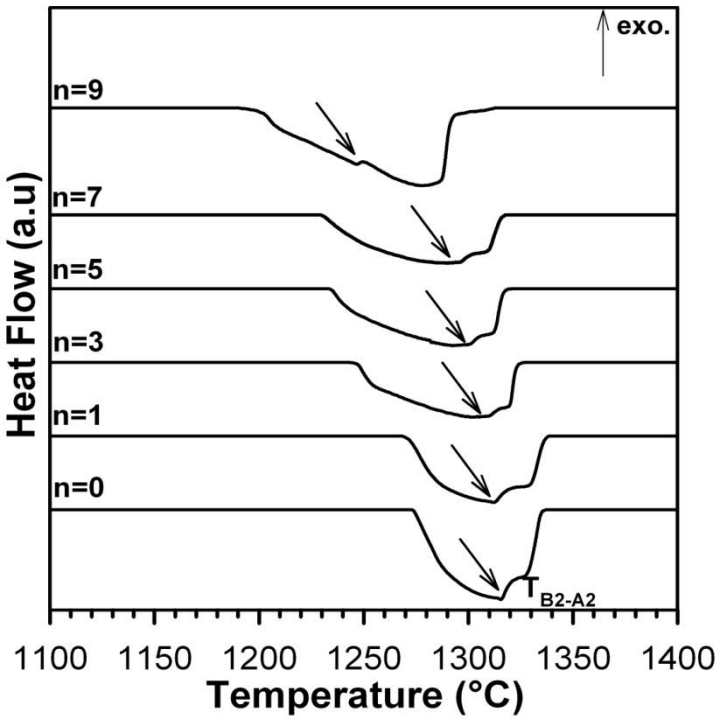

Figure 6.14 DSC heating (at a heating rate of 10K/min) curves of heat-treated $Fe_{50}Al_{50-n}Ti_n$ alloys.

7.2.2 Cyclic Oxidation Tests

The cyclic oxidation curves of heat-treated $Fe_{50}Al_{50-n}Ti_n$ alloys are plotted in Figure 6.15, showing the mass gain versus time at 900 °C. Total and net weight gains were recorded. The net weight gain corresponds to the sample weight excluding the spalled particles, while the total weight gain is the samples weight with their spalled oxides collected in ceramic crucibles. $Fe_{50}Al_{50-n}Ti_n$ samples with n = 1, 3, and 5 at.% do not show significant scale spallation, whereas $Fe_{50}Al_{43}Ti_7$ and $Fe_{50}Al_{41}Ti_9$ alloys exhibit scale spallation in the first three oxidation cycles. This spallation led to temporary mass losses. Both alloys exhibit an initial steep rise followed by small weight drop before they reach a plateau region.

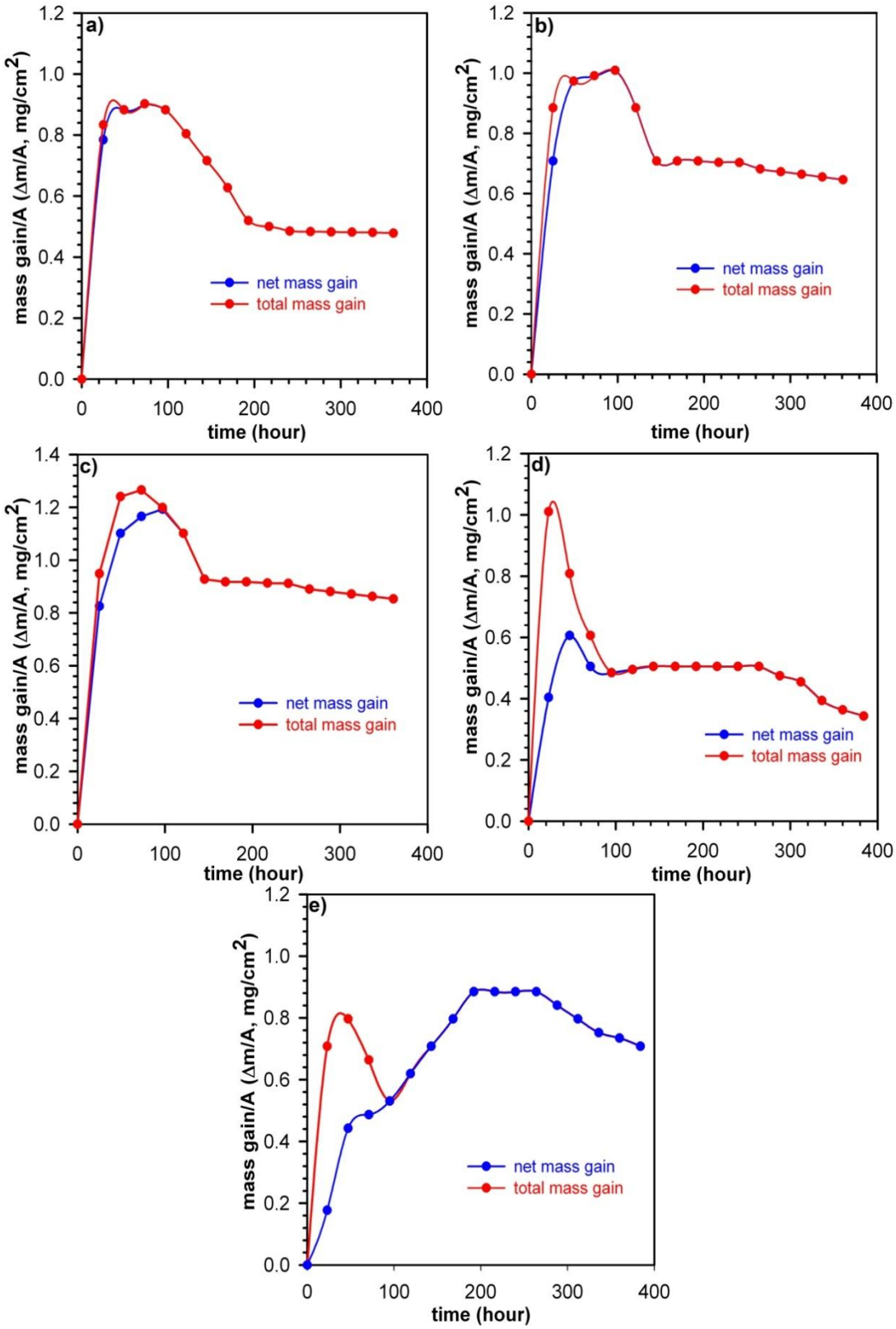

Figure 6.15 Mass gain versus time curves for cyclic oxidation tests of heat-treated $Fe_{50}Al_{50-n}Ti_n$ samples oxidised at 900 °C n = (a)1, (b) 3, (c) 5 , (d) 7 and (e) 9.

The main oxide product of the cyclic oxidation tests at 900 °C is stable α-Al_2O_3 for all Ti contents. However, small amount of TiO_2 (rutile) is formed starting from 5 at.% Ti addition and its volume fraction increases with increasing Ti concentration as understood by the increase in the relative peak intensities of rutile phase. In addition, high intensities of FeAl substrate indicate that the scale product is thin for all investigated alloys.

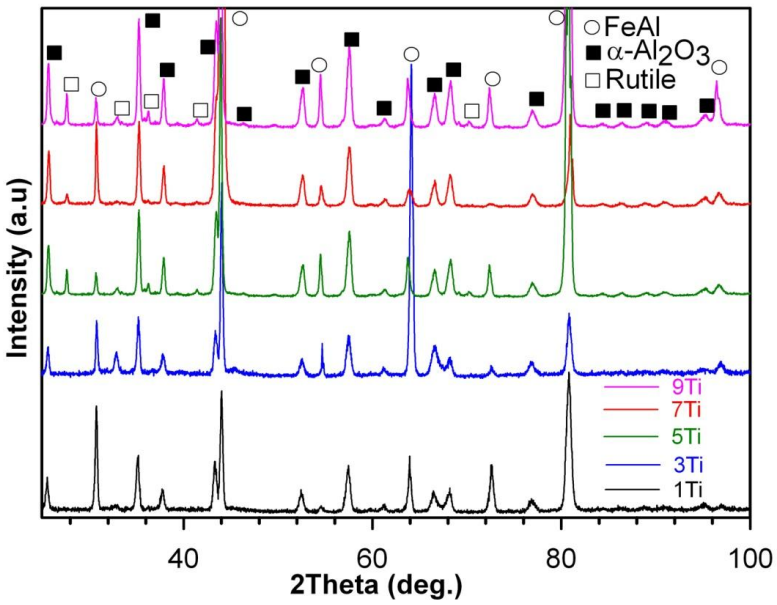

Figure 6.16 XRD patterns of heat-treated $Fe_{50}Al_{50-n}Ti_n$ samples oxidised at 900 °C.

The concentration of Ti has an important effect on the oxide scale morphology and scale spallation resistance of FeAl intermetallic compounds oxidised at 900 °C. The scale morphology of heat-treated $Fe_{50}Al_{50-n}Ti_n$ samples with n<9 is homogenous, continuous and even α-Al_2O_3 scale. For these compositions, scale is uniformly distributed along the whole surface without formation of any voids and cracks. Moreover, the results of EDS analysis showed that the scale predominantly consists of Al and O with trace amounts of Fe and Ti (Figure 6.18). Among these compositions, oxide scale morphology of 7 at.% Ti containing alloy is different than that of other compositions. The scale morphology of this composition (Figure 6.17(d)) is composed of finer Al_2O_3 nodules distributed uniformly and the scale is still adherent.

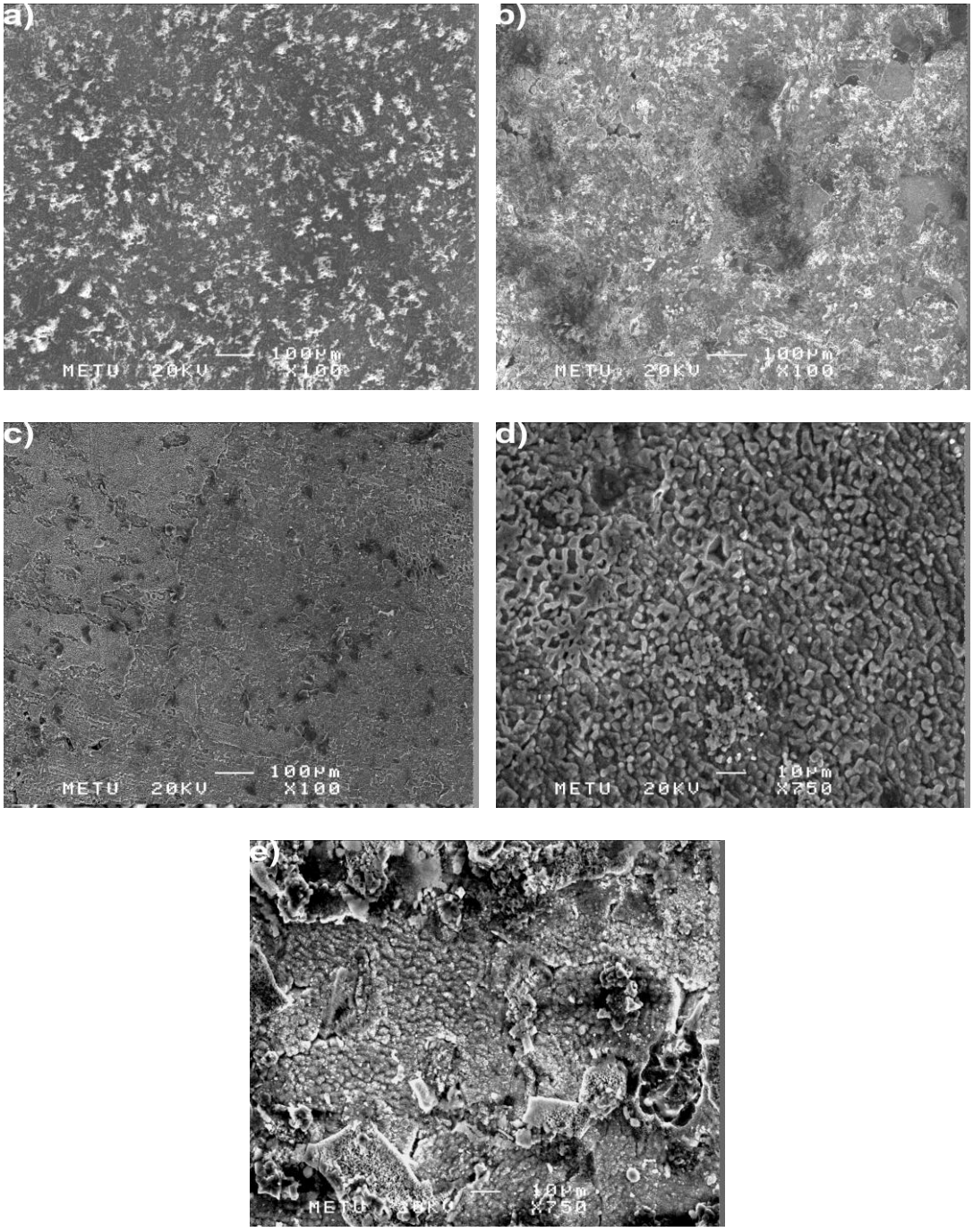

Figure 6.17 SEM micrographs showing the surface scale morphology of heat-treated $Fe_{50}Al_{50-n}Ti_n$ samples oxidised at 900 °C n = (a)1, (b) 3, (c) 5 , (d) 7 and (e) 9.

However, further increasing the Ti content to 9 at.% results in the generation of internal oxidation besides external oxidation. In the partially spalled external region large alumina plate-like structures made up finer whiskers and sphere-like TiO_2

particles are exist, while in the adherent internal part stable Al_2O_3 nodules are present. SEM observations indicated the formation of micro cracks initiated from the nodules embedded in the scale. The oxide formation free energy of Ti is between Fe and Al. Hence, it is another marginal oxide former besides Al and the initial stages of cyclic oxidation is affected before the formation of stable, continuous Al_2O_3 layer in the presence of Ti.

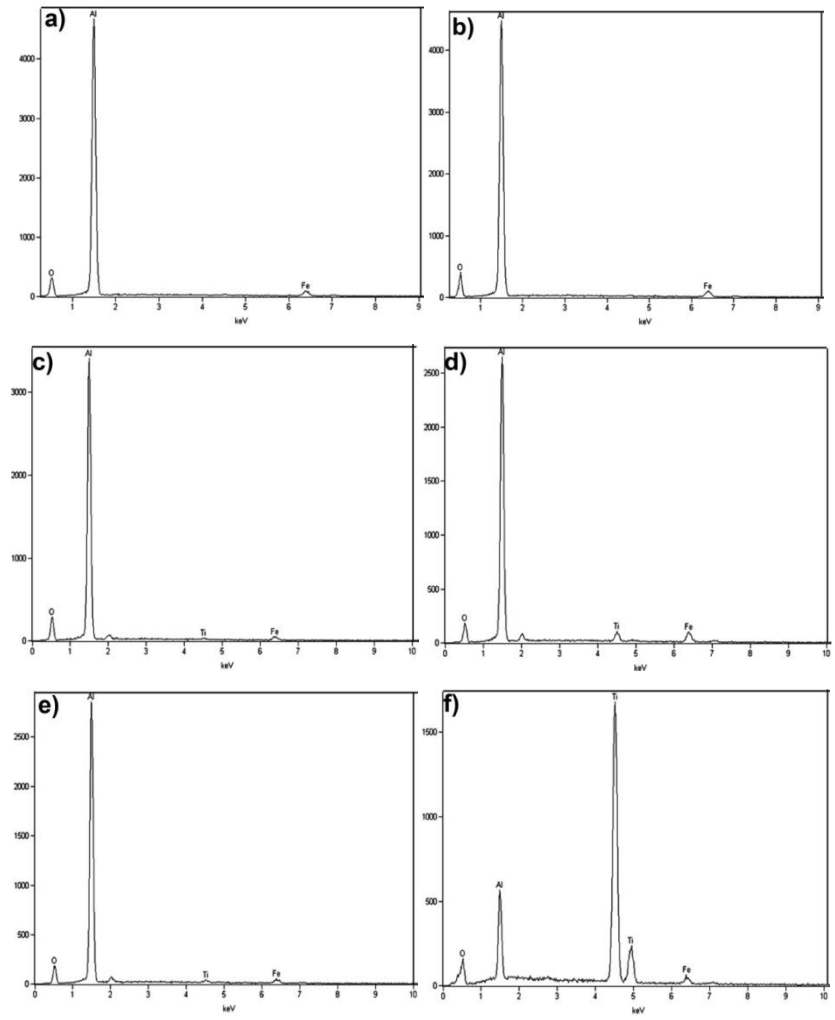

Figure 6.18 EDS elemental analyses of heat-treated $Fe_{50}Al_{50-n}Ti_n$ samples oxidised at 900 °C n = (a) 1, (b) 3, (c) 5 , (d) 7, (e) 9 (internal region showing stable Al_2O_3 nodules) and (f) 9 (external region sphere-like TiO_2 particles).

6.1.3 Conclusions

Structural properties and oxidation behavior of $Fe_{50}Al_{50-n}B_n$ alloys (n = 1, 3, 5, 7 and 9 at.%) have been investigated. Due to the limited solid solubility of Ti in FeAl, the ternary intermetallic Al_2FeTi (τ_2) phase is formed as a second phase precipitates even at 1 at.% Zr addition. The volume fraction of the Al_2FeTi precipitates increase with increasing Ti content.

The cyclic oxidation tests performed at 900 °C indicated that $Fe_{50}Al_{50-n}Ti_n$ alloys having 1, 3 or 5 at.% Ti did not show any scale spallation, whereas $Fe_{50}Al_{50-n}Ti_n$ alloys having 7 or 9 at.% Ti exhibited certain amount of scale spallation. The main oxide product is stable α-Al_2O_3 for all compositions. Small amount of TiO_2 (rutile) is present as another oxidation product for compositions containing 5, 7 or 9 at.% Ti and its volume fraction increases with Ti content. The scale morphology of the $Fe_{50}Al_{50-n}Ti_n$ samples except for $Fe_{50}Al_{41}Ti_9$ is homogenous, continuous and even α-Al_2O_3 scale without formation of any voids or cracks. For $Fe_{50}Al_{41}Ti_9$ composition, both external and internal oxidation is present and some regions contain certain amount of microcracks.

CHAPTER 7

CONCLUSIONS

- Theoretical predictions based on ordering characteristics of FeAl intermetallic compounds were verified experimentally.
- The relative partial ordering energy (RPOE) parameter, β, was defined to estimate the variation of order-disorder transition by taking into account the partial ordering energies of Al-X and Fe-X atomic pairs and also the site occupancy behavior of X element atoms.
- The sign of the β parameter implies the distribution of ternary alloying additions, while its magnitude provides an indication of the variation of the order-disorder transition temperature relative to binary FeAl alloys.
- Room temperature mechanical properties can be improved by proper selection of type and content of ternary alloying elements together with an appropriate heat-treatment.
- Among investigated alloys, Fe-Al-Mn alloys exhibit best room temperature ductility, while Fe-Al-Nb alloys display best combination of mechanical properties by means of enhanced ductility with high strength.

CHAPTER 8

FUTURE SUGGESTIONS

- Site occupancy characteristics of ternary alloying elements can be verified experimentally by Rietveld Refinement analyses.
- Room temperature mechanical properties can be further improved with increasing grain boundary strength by formation of carbide or boride particles at grain boundaries
- For eutectic alloys, room temperature mechanical properties can be modified by controlling the volume fraction and size of the eutectic constituents by adjusting the heat-treatment temperature and duration.

REFERENCES

[1] C.T. Liu, K.S. Kumar, JOM, 45 (1993) 38-44.

[2] I. Baker, E.P. George, Metals and Materials, 8 (1992) 318-323.

[3] D.P. Pope, Materials Research Society Symposium Proceedings, 81 (1986) 3-9.

[4] C.T. Liu, Materials Chemistry and Physics, 42 (1995) 77-86.

[5] D. Hardwick, G. Wallwork, Review of High Temperature Material, 4 (1978) 47-74.

[6] M.H. Yoo, S.L. Sass, C.L. Fu, M.J. Mills, D.M. Dimiduk, E.P. George, Acta Metallurgica et Materialia, 41 (1993) 987-1002.

[7] S.C. Deevi, V.K. Sikka, Intermetallics, 4 (1996) 357-375.

[8] C.T. Liu, J. Stringer, J.N. Mundy, L.L. Horton, P. Angelini, Intermetallics, 5 (1997) 579-596.

[9] N.S. Stoloff, Materials Science and Engineering: A, 258 (1998) 1-14.

[10] N.S. Stoloff, C.T. Liu, S.C. Deevi, Intermetallics, 8 (2000) 1313-1320.

[11] M. Palm, Intermetallics, 13 (2005) 1286-1295.

[12] F. Stein, M. Palm, G. Sauthoff, Intermetallics, 13 (2005) 1275-1285.

[13] C.T. Liu, J.O. Stiegler, Science, 226 (1984) 636-642.

[14] C.T. Liu, International Materials Reviews, 29 (1984) 168-194.

[15] C.G. McKamey, Physical Metallurgy and Processing of Intermetallic Compounds, Chapman and Hall, New York, NY, 1996.

[16] A.O. Mekhrabov, M.V. Akdeniz, Acta Materialia, 47 (1999) 2067-2075.

[17] T.B. Massalski, Chapter 3 - Structure and Stability of Alloys, in: W.C. Robert, H. Peter (Eds.) Physical Metallurgy (Fourth Edition), North-Holland, Oxford, 1996, pp. 135-204.

[18] D.A. Porter, K.E. Easterling, M.Y. Sherif, Phase transformations in metals and alloys, CRC Press, Boca Raton, FL, 2009.

[19] Laughlin D.E, in: Encylopedia of Materials sceince and Engineering Supplementary 1988, pp. 263-268.

[20] C.T. Liu, Materials Research Society Symposium Proceedings, 288 (1993) 3-17.

[21] I. Baker, D.J. Gaydosh, Materials Science and Engineering, 96 (1987) 147-158.

[22] D.J. Gaydosh, S.L. Draper, M.V. Nathal, Metall and Mat Trans A, 20 (1989) 1701-1714.

[23] C. Sykes, J.W. Bampfylde, Journal of Iron and Steel Institute, 130 (1934) 389-418.

[24] N.A. Ziegler, AIME Transactions, 100 (1932) 267.

[25] R.W. Cahn, J.A. coll, Acta Metallurgica, 9 (1961) 138-148.

[26] A. Lawley, E.A. Vidoz, R.W. Cahn, Acta Metallurgica, 9 (1961) 287-296.

[27] A. Lawley, J.A. Coll, R.W. Cahn, Transactions of the Metallurgical Society of AIME, 218 (1960) 166-176.

[28] U.R. Kattner, B.P. Burton, Phase Diagrams of Binary Alloys, ASM International, Materials Park,OH, 1993.

[29] R.R. Judkins, U.S. Rao, Intermetallics, 8 (2000) 1347-1354.

[30] K. Natesan, Materials Science and Engineering: A, 258 (1998) 126-134.

[31] J.L. Jordan, S.C. Deevi, Intermetallics, 11 (2003) 507-528.

[32] J.H. Devan, Oxidation of High Temperature Intermetallics, The Materials, Metals and Minerals Society (TMS), Warrendale, PA, 1989.

[33] P. Morgand, P. Mouturat, G. Sainfort, Acta Metallurgica, 16 (1968) 867-875.

[34] J. Herrmann, G. Inden, G. Sauthoff, Acta Materialia, 51 (2003) 2847-2857.

[35] H. Xiao, I. Baker, Acta Metallurgica et Materialia, 43 (1995) 391-396.

[36] I. Baker, H. Xiao, O. Klein, C. Nelson, J.D. Whittenberger, Acta Metallurgica et Materialia, 43 (1995) 1723-1730.

[37] U. Reimann, G. Sauthoff, Intermetallics, 7 (1999) 437-445.

[38] Y.A. Chang, L.M. Pike, C.T. Liu, A.R. Bilbrey, D.S. Stone, Intermetallics, 1 (1993) 107-115.

[39] R. Krachler, H. Ipser, B. Sepiol, G. Vogl, Intermetallics, 3 (1995) 83-88.

[40] C.T. Liu, E.H. Lee, C.G. McKamey, Scripta Metallurgica, 23 (1989) 875-880.

[41] M.G. Mendiratta, S.K. Ehlers, D.M. Dimiduk, W.R. Kerr, S. Mazdiyasni, H.A. Lipsitt, MRS Online Proceedings Library, 81 (1986) 393-403.

[42] P. Nagpal, I. Baker, Materials Characterization, 27 (1991) 167-173.

[43] D.J. Gaydosh, M.V. Nathal, Scripta Metallurgica et Materialia, 24 (1990) 1281-1284.

[44] C.T. Liu, E.P. George, Scripta Metallurgica et Materialia, 24 (1990) 1285-1290.

[45] R.H. Titran, K.M. Vedula, G.G. Anderson, Materials Research Society Symposium Proceedings, 39 (1985) 309-317.

[46] C.G. McKamey, J.A. Horton, C.T. Liu, Journal of Materials Research, 4 (1989) 1156-1163.

[47] C.G. McKamey, J.A. Horton, C.T. Liu, Scripta Metallurgica, 22 (1988) 1679-1681.

[48] C.G. McKamey, C.T. Liu, Scripta Metallurgica et Materialia, 24 (1990) 2119-2122.

[49] D. Li, D. Lin, Y. Liu, Materials Science and Engineering: A, 249 (1998) 206-216.

[50] M. Salazar, A. Albiter, G. Rosas, R. Pérez, Materials Science and Engineering: A, 351 (2003) 154-159.

[51] C.H. Kong, P.R. Munroe, Scripta Metallurgica et Materialia, 30 (1994) 1079-1083.

[52] C.H. Kong, P.R. Munroe, Scripta Metallurgica et Materialia, 28 (1993) 1241-1244.

[53] P.R. Munroe, Intermetallics, 4 (1996) 5-11.

[54] J.H. Schneibel, E.P. George, I.M. Anderson, Intermetallics, 5 (1997) 185-193.

[55] J.H. Schneibel, E.D. Specht, W.A. Simpson, Intermetallics, 4 (1996) 581-583.

[56] L.O.U. Baiyang, X.B. Zhang, L.I.U. Maosen, Z. Zhang, Journal of Materials Science, 33 (1998) 1481-1486.

[57] P. La, Y. Wei, R. Lv, Y. Zhao, Y. Yang, Materials Science and Engineering: A, 527 (2010) 2313-2319.

[58] D. Li, D. Lin, T.L. Lin, A. Shan, Y. Liu, Scripta Metallurgica et Materialia, 30 (1994) 655-659.

[59] D.D. Risanti, G. Sauthoff, Intermetallics, 13 (2005) 1313-1321.

[60] A. Wasilkowska, M. Bartsch, F. Stein, M. Palm, K. Sztwiertnia, G. Sauthoff, U. Messerschmidt, Materials Science and Engineering: A, 380 (2004) 9-19.

[61] F. Stein, M. Palm, G. Sauthoff, Intermetallics, 12 (2004) 713-720.

[62] G. Sauthoff, Intermetallics, 8 (2000) 1101-1109.

[63] K.S. Kumar, MRS Online Proceedings Library, 460 (1996) 677-688.

[64] F. Stein, G. Sauthoff, M. Palm, J. Phase Equilib. Diffus., 23 (2002) 480-494.

[65] V. Raghavan, J. Phase Equilib. Diffus., 31 (2010) 459-462.

[66] V. Raghavan, J. Phase Equilib. Diffus., 27 (2006) 284-287.

[67] V. Raghavan, J. Phase Equilib. Diffus., 31 (2010) 166-167.

[68] M. Palm, Journal of Alloys and Compounds, 475 (2009) 173-177.

[69] O. Prymak, F. Stein, Intermetallics, 18 (2010) 1322-1326.

[70] M.A. Mota, A.A. Coelho, J.M.Z. Bejarano, S. Gama, R. Caram, Journal of Alloys and Compounds, 399 (2005) 196-201.

[71] M.A. Mota, A.A. Coelho, J.M.Z. Bejarano, S. Gama, R. Caram, Journal of Crystal Growth, 198–199, Part 1 (1999) 850-855.

[72] S. Milenkovic, M. Palm, Intermetallics, 16 (2008) 1212-1218.

[73] J.M. Park, K.B. Kim, W.T. Kim, M.H. Lee, J. Eckert, D.H. Kim, Intermetallics, 16 (2008) 642-650.

[74] J.M. Park, S.W. Sohn, D.H. Kim, K.B. Kim, W.T. Kim, J. Eckert, Applied Physics Letters, 92 (2008) 091910-091913.

[75] R. Reviere, G. Sauthoff, D.R. Johnson, B.F. Oliver, Intermetallics, 5 (1997) 161-172.

[76] D.D. Risanti, G. Sauthoff, Intermetallics, 19 (2011) 1727-1736.

[77] V.V. Burnashova, V.R. Ryabov, V.Y. Markiv, Dopovidi Akademii Nauk Ukrainskoi Rsr Seriya A-Fiziko-Matematichni Ta Technichni Nauki, 8 (1969) 741-743.

[78] U. Prakash, G. Sauthoff, Intermetallics, 9 (2001) 107-112.

[79] R. Krein, M. Friak, J. Neugebauer, M. Palm, M. Heilmaier, Intermetallics, 18 (2010) 1360-1364.

[80] P. Hausild, J. Siegl, P. Malek, V. Sima, Intermetallics, 17 (2009) 680-687.

[81] M. Palm, G. Sauthoff, Intermetallics, 12 (2004) 1345-1359.

[82] M. Eumann, G. Sauthoff, M. Palm, Intermetallics, 16 (2008) 834-846.

[83] M. Eumann, G. Sauthoff, M. Palm, Intermetallics, 16 (2008) 706-716.

[84] M. Eumann, M. Palm, G. Sauthoff, Intermetallics, 12 (2004) 625-633.

[85] Y.N. Berdovsky, Intermetallics Research Progress, Nova Science Publishers, 2008.

[86] D. Piotr, in: Department of Solid State Chemistry, University of Science and Technology, Cracow, Poland, 2006.

[87] P. Tomaszewicz, G.R. Wallwork, Oxidation of Metals, 19 (1983) 165-185.

[88] K. Natesan, P.F. Tortorelli, in: Int. Symp. on Nickel and Iron Aluminides: Processing, Properties, and Applications, ASM International, Cincinnati, OH, 1996, pp. 265.

[89] P. Tomaszewicz, G.R. Wallwork, Corrosion, 40 (1984) 152-157.

[90] G. Rybicki, J. Smialek, Oxidation of Metals, 31 (1989) 275-304.

[91] I. Rommerskirchen, B. Eltester, H.J. Grabke, Materials and Corrosion, 47 (1996) 646-649.

[92] K.M.N. Prasanna, A.S. Khanna, R. Chandra, W.J. Quadakkers, Oxidation of Metals, 46 (1996) 465-480.

[93] K. Natesan, in: 6th Annual Conf. on Fossil Energy Materials, Oak Ridge, Tennessee, 1992, pp. 271.

[94] I. Levin, D. Brandon, Journal of the American Ceramic Society, 81 (1998) 1995-2012.

[95] H.J. Grabke, M. Schütze, Oxidation of Intermetallics, Wiley, 2008.

[96] D.J. Baxter, K. Natesan, Reviews on high temperature materials, 5 (1983) 149-250.

[97] M. Schütze, Oxidation of Metals, 44 (1995) 29-61.

[98] P.F. Tortorelli, J.H. DeVan, Materials Science and Engineering A, 153 (1992) 573-577.

[99] N. Babu, R. Balasubramaniam, A. Ghosh, Corrosion Science, 43 (2001) 2239-2254.

[100] A. Velon, D.Q. Yi, Oxidation of Metals, 57 (2002) 13-31.

[101] D.B. Lee, G.Y. Kim, J.G. Kim, Materials Science and Engineering: A, 339 (2003) 109-114.

[102] V. Shankar Rao, M. Norell, V.S. Raja, Corrosion Science, 45 (2003) 2717-2728.

[103] V. Shankar Rao, H.S. Kwon, Intermetallics, 13 (2005) 23-26.

[104] D. Li, Y. Xu, D. Lin, Journal of Materials Science, 36 (2001) 979-983.

[105] I. Kim, W.D. Cho, H.J. Kim, Journal of Materials Science, 35 (2000) 4695-4703.

[106] W.D. Cho, I. Kim, Metall and Mat Trans A, 31 (2000) 1685-1687.

[107] C.H. Xu, W. Gao, H. Gong, Intermetallics, 8 (2000) 769-779.

[108] A.O. Mekhrabov, M. Doyama, physica status solidi (b), 126 (1984) 453-458.

[109] A.O. Mekhrabov, M.V. Akdeniz, M.M. Arer, Acta Materialia, 45 (1997) 1077-1083.

[110] A.O. Mekhrabov, A. Ressamolu, T. Öztürk, Journal of Alloys and Compounds, 205 (1994) 147-155.

[111] M.V. Akdeniz, A.O. Mekhrabov, Acta Materialia, 46 (1998) 1185-1192.

[112] M.V. Akdeniz, A.O. Mekhrabov, T. Yilmaz, Scripta Metallurgica et Materialia, 31 (1994) 1723-1728.

[113] M. Aykol, A.O. Mekhrabov, M.V. Akdeniz, Intermetallics, 18 (2010) 893-899.

[114] M. Aykol, A. Mekhrabov, M. Vedat Akdeniz, Metall and Mat Trans A, 41 (2010) 267-274.

[115] A.O. Mekhrabov, M.V. Akdeniz, İ. Aktürk, in: NATO ASI Series B: Physics, Plenum Press, New York, NY, 1996, pp. 681-686.

[116] A.O. Mekhrabov, Fizika Metallov i Metallovedenie, 62 (1986) 1023-1025.

[117] A.O. Mekhrabov, Z.M. Babaev, A.A. Katsnelson, Z.A. Matysina, Fizika Metallov i Metallovedenie, 61 (1986) 1089-1093.

[118] A.O. Mekhrabov, Turkish Journal of Engineering and Environmental Sciences, 18 (1994) 349-356.

[119] L. Anthony, B. Fultz, Acta Metallurgica et Materialia, 43 (1995) 3885-3891.

[120] Y. Nishino, C. Kumada, S. Asano, Scripta Materialia, 36 (1997) 461-466.

[121] Y. Nishino, S. Asano, T. Ogawa, Materials Science and Engineering: A, 234–236 (1997) 271-274.

[122] F. Stein, A. Schneider, G. Frommeyer, Intermetallics, 11 (2003) 71-82.

[123] I. Ohnuma, C.G. Schön, R. Kainuma, G. Inden, K. Ishida, Acta Materialia, 46 (1998) 2083-2094.

[124] J.B. Cohen, J.E. Hillard, in: Metallurgical Society Conferences, Gordon and Breach, New York, NY 1965, pp. 123-148.

[125] M. Kupka, Intermetallics, 14 (2006) 149-155.

[126] F. Stein, M. Palm, International Journal of Materials Research, 98 (2007) 580-588.

[127] E. Schürmann, H.P. Kaiser, Arch. Eisenhuettenwes, 51 (1980) 325-327.

[128] M.A. Krivoglaz, A. Smirnov, The Theory of Order-Disorder in Alloys, Macdonald, London, 1964.

[129] M. Eumann, in, Shaker-Verlag, Aachen, 2002.

[130] M.A. Crimp, K.M. Vedula, D.J. Gaydosh, MRS Online Proceedings Library, 81 (1986) 499-504.

[131] F. Stein, G. Sauthoff, M. Palm, International Journal of Materials Research, 95 (2004) 469-485.

[132] S.-M. Zhu, K. Sakamoto, M. Tamura, K. Iwasaki, Materials transactions-JIM, 42 (2001) 484-490.

[133] J.M. Park, J.H. Han, K.B. Kim, N. Mattern, J. Eckert, D.H. Kim, Philosophical Magazine Letters, 89 (2009) 623-632.

[134] G. He, J. Eckert, W. Löser, L. Schultz, Nature materials, 2 (2002) 33-37.

[135] J.M. Park, N. Mattern, U. Kühn, J. Eckert, K.B. Kim, W.T. Kim, K. Chattopadhyay, D.H. Kim, Journal of Materials Research, 24 (2009) 2605-2609.

[136] G.H. Cao, Y.F. Peng, N. Liu, X. Li, Z.S. Lei, Z.M. Ren, D. Gerthsen, A.M. Russell, Materials Science and Engineering: A, 609 (2014) 60-64.

[137] F. Czerwinski, A. Zielinska-Lipiec, P. Pinet, J. Overbeeke, Acta Materialia, 49 (2001) 1225-1235.

[138] H. Li, J. Guo, K. Huai, H. Ye, Journal of Crystal Growth, 290 (2006) 258-265.

[139] J. Sha, H. Hirai, T. Tabaru, A. Kitahara, H. Ueno, S. Hanada, Materials Science and Engineering: A, 364 (2004) 151-158.

[140] W. Gerberich, H. Huang, W. Zielinski, P. Marsh, MTA, 24 (1993) 535-543.

[141] G.E. Dieter, D. Bacon, Mechanical metallurgy, McGraw-Hill New York, 1986.

[142] M. Ashby, F. Blunt, M. Bannister, Acta Metallurgica, 37 (1989) 1847-1857.

[143] G. Yang, S. Milenkovic, Intermetallics, 55 (2014) 129-137.

[144] M. Yildirim, M.V. Akdeniz, A.O. Mekhrabov, Metall and Mat Trans A, 43 (2012) 1809-1816.

[145] S.-W. Chen, C.-C. Lin, C. Chen, Metall and Mat Trans A, 29 (1998) 1965-1972.

[146] M.E. Loomans, M.E. Fine, Metall and Mat Trans A, 31 (2000) 1155-1162.

[147] K.W. Moon, W.J. Boettinger, U.R. Kattner, F.S. Biancaniello, C.A. Handwerker, Journal of Elec Materi, 29 (2000) 1122-1136.

[148] W.-C. Cheng, C.-F. Liu, Y.-F. Lai, Materials Science and Engineering: A, 337 (2002) 281-286.

[149] M. Li, K. Nagashio, T. Ishikawa, A. Mizuno, M. Adachi, M. Watanabe, S. Yoda, K. Kuribayashi, Y. Katayama, Acta Materialia, 56 (2008) 2514-2525.

[150] J.W. Christian, The Theory of Transformations in Metals and Alloys, 1st ed., Pergamon Press, Oxford, 1965.

[151] L.F. Mondolfo, Materials Science and Technology, 5 (1989) 118-122.

[152] B.E. Sundquist, L.F. Mondolfo, Transactions of the Metallurgical Society of AIME, 221 (1961) 607-613.

[153] B.E. Sundquist, L.F. Mondolfo, Transactions of the Metallurgical Society of AIME, 221 (1961) 157-164.

[154] M. Plapp, A. Karma, Physical Review E, 66 (2002) 061608.

[155] C.T. Rios, S. Milenkovic, S. Gama, R. Caram, Journal of Crystal Growth, 237–239, Part 1 (2002) 90-94.

[156] H.W. Weart, Transactions of the Metallurgical Society of AIME, 212 (1958) 664-670.

[157] W. Kraft, D.L. Albright, Transactions of the Metallurgical Society of AIME, 221 (1961) 95-102.

[158] M.A. McGuire, N. Ghimire, D.J. Singh, Journal of Applied Physics, 111 (2012) 093918-093916.

[159] Q. Zeng, I. Baker, Intermetallics, 14 (2006) 396-405.

[160] F. Plazaola, E. Apinaniz, D.M. Rodriguez, E. Legarra, J.S. Garitaonandia, Fe-Al Alloys' Magnetism, in: L. Malkinski (Ed.) Advanced Magnetic Materials, Intech, Rijeka, Croatia, 2012, pp. 133-170.

[161] A. Arrott, H. Sato, Physical Review, 114 (1959) 1420-1426.

[162] A.K. Arzhnikov, L.V. Dobysheva, M.A. Timirgazin, Journal of Magnetism and Magnetic Materials, 320 (2008) 1904-1908.

[163] R.D. Shull, H. Okamoto, P.A. Beck, Solid State Communications, 20 (1976) 863-868.

[164] B. Majumdar, D. Akhtar, Materials Science and Technology, 21 (2005) 1139-1144.

[165] K. H.E., Journal of Research of the National Bureau of Standards, 57 (1956) 217-221.

[166] T. Ozawa, Journal of Thermal Analysis and Calorimetry, 2 (1970) 301-324.

[167] V. Rigaud, B. Sundman, D. Daloz, G. Lesoult, Calphad, 33 (2009) 442-449.

[168] M. Palm, G. Inden, N. Thomas, JPE, 16 (1995) 209-222.

CURRICULUM VITAE

Mehmet YILDIRIM

PhD Student, Research Assistant

Department of Metallurgical and Materials Engineering,
Novel Alloys Design and Development Laboratory (NOVALAB), Room D-312,
Middle East Technical University, 06531, Ankara, Turkey
e-mail: ymehmet@metu.edu.tr, tel: +905054559289, +903122102534

EDUCATION

2013-2014 Visiting Research Scholar, Materials Science Engineering, Northwestern University

2006-…. Student, Integrated PhD, -Metallurgical and Materials Engineering, Middle East Technical University

- GPA of 3.85/4.00
- Thesis Title: Iron Aluminium Intermetallic Compounds for Structural Applications at High Temperatures, Supervisor: Prof. Dr. M. Vedat Akdeniz

2000-2005 B.S.- Mechanical Engineering, Dokuz Eylül University

- Fifth highest GPA of 3.15/4.00, High Honour Degree.

RESEARCH INTEREST

- Intermetallics (based on aluminides)
- Ordered/Disordered Multicomponent Alloys
- Bulk Amorphous/Nanocrystalline Materials

- Fe-Nd-B based Hard Magnetic Materials
- Synthesis and characterization of magnetic nanoalloys produced via high energy ball milling.
- Ni based Superalloys
- Classical nucleation theory/Coarsening

PUBLICATIONS

1. E. Y. Plotnikov, D. Cecchetti, **M. Yıldırım**, S. Baik, Z. Mao, Y. Li, R. D. Noebe, and D. N. Seidman *"A Four-Dimensional Study of Phase Separation at the Subnano- to Nanoscale of a Ni-Al Alloy"* (2015), to be submitted to Acta Materialia.

2. E. Y. Plotnikov, **M. Yıldırım,** Y. Li, P. Mavis, S. Baik, R. D. Noebe, Z. Mao and D. N. Seidman *"A Correlative Five-Dimensional Study of Phase Separation at the Subnano- to Nanoscale of a Ni-12.5 Al at.% Alloy: 3-D Space, Temperature, and Time"* (2015), to be submitted to Acta Materialia.

3. E. Y. Plotnikov, **M. Yıldırım,** Y. Li, P. Mavis, S. Baik, R. D. Noebe, Z. Mao and D. N. Seidman *"A Correlative Five-Dimensional Study of Phase Separation at the Subnano- to Nanoscale of a Ni-13.4 Al at.% Alloy: 3-D Space, Temperature, and Time"* (2015), to be submitted to Acta Materialia.

4. **M. Yıldırım**, M. V. Akdeniz and A. O. Mekhrabov *"Microstructural Investigation and Phase Relationships of Fe-Al-Hf Alloys"* (2014), Metallurgical and Materials Transactions A, Vol. 45 No:8, pp. 3412-3421.

5. **M. Yıldırım**, M. V. Akdeniz and A. O. Mekhrabov *"Effect of ternary alloying elements addition on the order-disorder transformation*

temperatures of B2-type ordered Fe-Al-X intermetallics" (2012), Metallurgical and Materials Transactions A, Vol. 43 No:6, pp. 1809-1816.

6. I. Küçük, M. Aykol, O. Uzun, **M. Yıldırım**, M. Kabaer, N. Duman, F. Ylmaz, K. Ertürk, M.V. Akdeniz and A.O. Mekhrabov "*Effects of (Mo, W) Substitution for Nb on Glass Forming Ability and Magnetic Properties of Fe-Co-based Bulk Amorphous Alloys Fabricated by Centrifugal Casting"* (2011), Journal of Alloys and Compounds, Vol. 509, No: 5, pp. 2334-2337.

ABSTRACTS & PROCEEDINGS

1. E. Y. Plotnikov, D. Cecchetti, **M. Yıldırım**, Z. Mao, R. D. Noebe, and D. N. Seidman *"On the temporal evolution of the γ(f.c.c.)- and γ'(L12)-phases in a Ni-12.5 Al at.% alloy"* , 31th The John Hillard Symposium, Department of Materials Science and Engineering, Northwestern University, 15 May 2014, Evanston, USA, Abstract.

2. **M. Yıldırım**, M.V. Akdeniz and A.O. Mekhrabov (2012), *"Effect of Mo Addition on Structural Properties of B2-type ordered FeAl Intermetallics",* 16th International Metallurgy & Materials Congress (IMMC 2012), UCTEA Chamber of Metallurgical Engineers, 13-15 September 2012, Istanbul, Turkey, Congress e-Book, pp. 642-650.

3. **M. Yıldırım**, M.V. Akdeniz and A.O. Mekhrabov (2011), *"Energetical and structural characterization of B2↔A2 order-disorder phase transformation in* $Fe_{0.5}(Al_{1-n}X_n)_{0.5}$ *intermetallics"*, Discussion Meeting on the Development of Innovative Iron Aluminium Alloys (FeAl2011), 5-7 October 2011, Lanzarote, Spain, Abstract and Proceeding Book, pp.75-78.

4. **M. Yıldırım**, M.V. Akdeniz and A.O. Mekhrabov (2011), *"Effect of X=Hf and Zr alloying addition on the microstructures of B2-type ordered*

$Fe_{0.5}(Al_{1-n}X_n)_{0.5}$ intermetallic alloys", Discussion Meeting on the Development of Innovative Iron Aluminium Alloys (FeAl2011), 5-7 October 2011, Lanzarote, Spain, Abstract and Proceeding Book, pp.90-93.

5. I. Küçük, M. Aykol, **M. Yıldırım**, M.V. Akdeniz and A.O. Mekhrabov (2010), "*Effects of Mo, W, Nb Additions and Heat Treatments on Thermal and Magnetic Properties of Fe-Co-B Based Bulk Metallic Glass Alloys Produced by Centrifugal Casting",* International Conference on Superconductivity and Magnetism (ICSM 2010), Ankara University, 25-30 April 2010, Antalya, Turkey, ICSM 2010 Abstract Book, p.

6. **M. Yıldırım**, M.V. Akdeniz and A.O. Mekhrabov (2010), "*Effect of Nanocrystallization on Magnetic Properties of Bulk Amorphous $Fe_{75-x}Co_xNd_3Zr_2Y_3B_{17}$ Alloys",* 6th Nanoscience and Nanotechnology Conference on (NANOTR-VI), IZTECH Izmir Institute of Technology, 15-18 June 2010, Izmir, Turkey, Abstract Book, p. 233.

7. **M. Yıldırım**, M.V. Akdeniz and A.O. Mekhrabov (2010), "*Effect of Co Concentration on Structural and Magnetic Properties of Bulk Amorphous/Nanocrystalline Fe-Nd-Zr-Y-B Alloys",* 5th International Conference on Nanostructured Materials (NANO 2010), 13-17 September 2010, Roma, Italy, Abstract Book, p.203.

8. **M. Yıldırım**, M.V. Akdeniz and A.O. Mekhrabov (2010), "*Effect of Nb and Hf on Microstructure and Microhardness of FeAl Based alloys",* 13th International Materials Symposium (IMSP 2010), Pamukkale University Engineering Faculty, 13-15 October 2010, Denizli, Turkey, Proceedings of 13th International Materials Symposium, pp. 628-635.

9. **M. Yıldırım**, M.V. Akdeniz and A.O. Mekhrabov (2010), "*Synthesis of Bulk Amorphous/ Nanocrystalline Fe-Co-Nd-B Magnetic Alloys"*, 15th International Metallurgy & Materials Congress (IMMC 2010), UCTEA Chamber of Metallurgical Engineers, 11-13 November 2010, Istanbul, Turkey, Congress e-Book, pp. 416-422.

10. **M. Yıldırım**, M. V. Akdeniz and A. O. Mekhrabov (2008), *"Effect of Transition Metal Additions on B2↔A2 Order-Disorder Phase Transition Temperatures in B2 Type FeAl Intermetallic Compounds"*, (MRS Fall Meeting 2008), Boston, USA, 1128, p.U2.8.

11. **M. Yıldırım**, M.V. Akdeniz and A.O. Mekhrabov (2008), "*Modelling of Glass Forming Ability of Fe-Al Based Alloy Systems"*, 13th International Metallurgy & Materials Congress (IMMC 2008), UCTEA Chamber of Metallurgical Engineers, 16-18 October 2008, Istanbul, Turkey, Congress e-Book, pp. 34-43.

12. **M. Yıldırım**, M.V. Akdeniz and A.O. Mekhrabov (2008), "*Modelling of Glass Forming Ability of Fe-Al Based Alloy Systems"*, 13th International Metallurgy & Materials Congress (IMMC 2008), UCTEA Chamber of Metallurgical Engineers, 16-18 October 2008, Istanbul, Turkey, Congress e-Book, pp. 120-127.

13. **M. Yıldırım**, M. V. Akdeniz and A. O. Mekhrabov (2007), *"Thermal analysis of order-disorder phase transformations of B2-type ordered Fe-Al-X intermetallics"*, 4th Discussion meeting on the development of innovative iron aluminium alloys, 21-24 October, Interlaken, Switzerland, Abstract Book, p.25.

14. **M. Yıldırım**, A. O. Mekhrabov and M.V. Akdeniz (2006), *"Magnetocaloric Properties of Fe-based Bulk Amorphous/Nanocrystalline Alloys"*, International Congress on Modern

Problems of Physics of Metals, 26-27 October 2006, Baku, Azerbaijan, Proceeding, pp.187-190.

SKILLS

- Analysis Software:
  - Thermal Analysis Software (Calisto),
  - Diffraction Analysis Software (Rigaku, PDFGetX),
  - Rietveld Analysis Software (Maud, Gsas, Expgui)
  - Peak Deconvolution (PeakFit),
  - SigmaPlot,
  - Mathematica, Matlab
  - Atom Probe Tomography Software (IVAS)

Experimental

- Atmosphere Controlled Arc-Melting
- Centrifugal Casting
- X-ray Diffractometer
- Scanning Electron Microscope
- Transmission Electron Microscope
- Atom Probe Tomography
- Vibrating Sample Magnetometer (VSM)
- Thermal Analyses (DSC/DTA/TGA)

RESEARCH / TEACHING EXPERIENCE

Researcher / Assistant

2006 – …. Research Assistance, Department of Metallurgical and Materials Engineering, Middle East Technical University, Ankara, Turkey.

2006 –Teaching Assistance

- Met E 201 Materials Science I
- Met E 202 Materials Science II
- Met E 206 Materials Laboratory
- Met E 222 Materials Science and Engineering
- Met E 225 Engineering Materials
- Met E 229 Materials Science and Engineering
- Met E 468 Welding Metallurgy
- Met E 507 Advance Crystallography
- Met E 538 Advanced Solidification
- Met E 540 Phase Stability in Alloys

SCHOLARSHIPS

2007 – 2011 The Scientific and Technological Research Council of Turkey, TUBITAK, National Scholarship Programme for PhD Students.